

DISSERTATION

Rare Earth Substituted Hexaferrites

ausgeführt zum Zwecke der Erlangung des akademischen
Grades eines Doktors der technischen Wissenschaften

unter der Leitung von

A. o. Prof. Dipl.-Ing. Dr. techn. Roland Grössinger,
Institut für Festkörperphysik (E138),

eingereicht an der Technischen Universität Wien,
Fakultät für Physik,

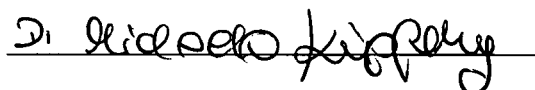
von

Dipl.-Ing. Michaela KÜPFERLING

Matrikelnummer: 9126262

1230 WIEN, Stipcakgasse 14/7/13

Wien, im Juni 2005



Kurzfassung

Aufgaben der vorliegenden Doktorarbeit war mit Selten-Erd Elementen substituierte M-Typ Hexaferrite zu untersuchen und Änderungen von magnetischen und strukturellen Eigenschaften mit der Substitution zu beobachten. Die Arbeit bestand aus vier Hauptteilen: Bestimmung magnetischer Eigenschaften von hydrothermal synthetisierten Proben, Herstellung von La substituierten Sr Hexaferrit Proben, Untersuchung von magnetischen und strukturellen Eigenschaften dieser Proben und Elektronenstruktur-Berechnungen.

Der erste Teil diente zur Untersuchung von an der Universität von Birmingham mittels hydrothormaler Synthese hergestellten Sr-Hexaferrit Proben, in welchen ein Teil der Sr-Ionen durch ein Selten-Erd (SE) Element ersetzt wurde. Die verwendeten Elemente waren La, Sm, Nd, Pr in Konzentrationen $SE/Sr=1/24, 1/20, 1/16, 1/8, 1/4, 1/2$. Diese Proben waren bereits mittels XRD und SEM charakterisiert. Messungen von magnetischen Eigenschaften dieser Proben und Charakterisierung mittels NMR wurden innerhalb dieser Arbeit durchgeführt. Die Anisotropie wurde mittels SPD ("singular point detection") Verfahren gemessen und zeigte bei Raumtemperatur nur eine leichte Zunahme und keine klare Abhängigkeit von der SE Konzentration. Messungen der Sättigungsmagnetisierung lieferten sowohl bei Raumtemperatur als auch bei 4.2 K einen erniedrigten Wert mit zunehmender Substitution. Bei tiefen Temperaturen war das Anisotropiefeld nahezu Temperatur unabhängig, vergleichbar mit reinem Sr-Hexaferrit. Mit Röntgenstreuung wurde der Grund für dieses Verhalten sichtbar, da eine hohe Menge an Fremdphasen in Proben mit hoher SE Konzentration auftrat. Für sehr kleine Konzentrationen bis $SE/Sr=1/16$ wurde eine Verschiebung aller fünf ^{57}Fe Linien in den NMR-Spektren beobachtet, was durch das Auftreten eines großen Polarons erklärt wurde. Für höhere Konzentrationen zeigten die NMR Spektren, aber auch Mössbauer Messungen, keine relevante Abweichung von reinem Sr-Hexaferrit.

Ein Hauptteil der Arbeit war, eine entsprechende Methode zur Herstellung von SE substituierten Hexaferriten zu entwickeln, Hauptaugenmerk wurde dabei auf den reinen La-Hexaferrit und La substituierten Sr-Hexaferrit

gelegt. Vier verschiedene, für Ferrite typische, Herstellungsmethoden wurden für den reinen La-Hexaferrit versucht: Mechanische Legierung, mit Hilfe einer Kugelmühle, Coprecipitation, Sol-Gel und Sol-Gel-„Selbstverbrennungs“-Methode. Die Herstellung der Hexaferrit-Phase war mit allen vier Methoden erfolgreich. Der wesentliche Punkt in der Herstellung ist die Wärmebehandlung bei hohen Temperaturen. La-Hexaferrit ist eine Hochtemperaturphase, die nur in dem engen Temperaturbereich zwischen 1380°C und 1420°C stabil ist. Bei Raumtemperatur liegt eine metastabile Verbindung vor, die leicht zerfällt. Deshalb muss sofort nach der Wärmebehandlung ein rasches Abschrecken der Probe, z.B. in Wasser, erfolgen. Durch Variation der Ofentemperatur und des La-Überschusses war es möglich, die Menge von in der Probe enthaltenen Fremdphasen zu minimieren. Die Probe mit der geringsten Verunreinigung, hergestellt mit Coprecipitation, enthielt 10% LaFeO₃ und Fe₂O₃ als Fremdphasen, die in der Kugelmühle hergestellte war XRD zufolge rein. Sr-Hexaferrit Proben mit unterschiedlichem La-Gehalt wurden hauptsächlich mittels mechanischer Legierung hergestellt, wobei La Konzentrationen von La/Sr=1/8, 1/4, 1/2, 1/1, 1/3 verwendet wurden. Die Wärmebehandlung dieser Proben musste bei hohen Temperaturen, ähnlich wie für den reinen La-Hexaferrit, erfolgen, um die Bildung von Fremdphasen zu vermeiden. Allerdings war eine kleine Menge an Verunreinigung für höhere La-Konzentrationen (>1/4) immer vorhanden. Es wurde ebenfalls versucht, Dy- und Er-Hexaferrit mit der gleichen Methode herzustellen. Der Stabilitäts-Temperaturbereich dieser Verbindung ist unbekannt, weshalb mehrere Temperaturen in einem größeren Bereich zur Wärmebehandlung gewählt wurden, bisher ohne Erfolg.

Anschließend wurden diese Proben mittels XRD charakterisiert, um die Phasen zu bestimmen und Änderungen der Gitterparameter mit der Substitution zu erkennen. Eine Gitterverzerrung des reinen La-Hexaferrites wurde bei tiefen Temperaturen anhand von Neutronenstreuung beobachtet. Informationen über die lokale Umgebung der Fe-Ionen wurde durch NMR und Mössbauer-Spektroskopie gewonnen und lieferten wichtige Erkenntnisse über den Wertigkeitszustand der Fe-Ionen und Veränderungen aufgrund der Gitterverzerrung. Festkörpereigenschaften wie die Dichte wurden gemessen und mit der Röntgendichte verglichen. Der elektrische Widerstand wurde von

30 K bis Raumtemperatur gemessen und zeigte einen verringerten Wert mit steigender La-Konzentration. Magnetische Eigenschaften wurden mit unterschiedlichen Verfahren bestimmt. Die Anisotropie wurde mittels SPD Verfahren von 4.2 K bis Raumtemperatur gemessen. Es zeigte sich ein starker Anstieg mit fallender Temperatur für den reinen La-Hexaferrit, ebenfalls eine Zunahme für die Probe mit einer La-Konzentration von $\text{La}/\text{Sr}=3/1$, aber eine Abnahme für alle geringeren Konzentrationen. Es war möglich, eine qualitative Erklärung dieses Verhaltens zu geben. Magnetisierungskurven wurden bei Raumtemperatur und bei 4.2 K gemessen. Das Koerzitivfeld aller Proben ist außerordentlich gering, was durch die Bildung von extrem großen Körnern aufgrund der Wärmebehandlung bei sehr hohen Temperaturen erklärt werden konnte. Die Sättigungsmagnetisierung zeigte eine nur geringe Abnahme mit der La-Konzentration.

Im letzten Teil wurden Elektronenstrukturberechnungen mit einem auf der Dichte-Funktional-Theorie basierendem Programm (Wien2k) durchgeführt. Unterschiedliche Methoden wurden hierbei verglichen. Die Zustandsdichte und die lokalen magnetischen Momente wurden berechnet und mit den Experimenten verglichen. Diese ersten Berechnungen stellen die Grundlage für Berechnungen von Anisotropie und Hyperfeinfeldern, die das experimentell beobachtete Verhalten erklären könnten.

Summary

Within this thesis rare earth substituted M-type hexaferrites, mainly Sr hexaferrite, were investigated in order to monitor changes in magnetic and structural properties with the substitution. The work was divided in four main parts: investigation of magnetic properties of samples prepared by hydrothermal synthesis, preparation of La substituted Sr hexaferrite samples, investigation of magnetic and structural properties of these samples and calculations of the electron structure of these samples.

In the first part Sr hexaferrite samples prepared by hydrothermal synthesis were obtained from the University of Birmingham, where a part of Sr ions was substituted by a rare earth element. The elements used were La, Sm, Nd, Pr in concentrations of RE/Sr=1/24, 1/20, 1/16, 1/8, 1/4, 1/2. These samples were obtained already characterized by XRD and SEM. Measurements of magnetic properties of these samples and NMR were performed within this work. The anisotropy measured by singular point detection (SPD) technique at room temperature showed only slight increase and no clear dependence on the RE concentration. The magnetization at room temperature and 4.2 K was decreased with increasing amount of substitution. The low temperature anisotropy was almost constant with respect to temperature, like in the pure Sr hexaferrite. With X-ray diffraction the reason for this behavior was found in a high amount of secondary phases for high RE concentrations. For very small concentrations up to RE/Sr=1/16, a shift of all five ^{57}Fe peaks was found in the NMR spectra, which was explained by the effect of a large polaron. For higher concentrations the NMR spectrum but also Mössbauer exhibited no significant deviation from the pure Sr hexaferrite.

One main part of the work was to develop an appropriate preparation method for RE substituted hexaferrites. This was focused on La hexaferrite and La substituted Sr hexaferrite. Four different preparation methods, common in ferrite production, were tried for the pure La hexaferrite: Mechanical alloying by using a steel ball mill, coprecipitation, sol gel and sol gel autocombustion method. With all four methods the hexaferrite phase was obtained. It was found out that the essential point in the preparation is the

heat treatment at high temperatures. The La hexaferrite is a high temperature phase, stable only in the narrow temperature range between 1380°C and 1420°C. At room temperature it is a metastable compound, and decomposes easily. Therefore a rapid quenching, e.g. in water, has to be performed after the heat treatment. By variation of the furnace temperature and the La excess it was possible to minimize the amount of secondary phases. The sample with the smallest amount prepared by coprecipitation still contained 10% LaFeO_3 and Fe_2O_3 , the one prepared by mechanical alloying was pure according to XRD. Sr hexaferrite samples with different La amount were mainly prepared by mechanical alloying and ratios of $\text{La}/\text{Sr}=1/8, 1/4, 1/2, 1/1, 1/3$ were used. A heat treatment of these samples had to be performed at high temperatures like used for the pure La hexaferrite in order to avoid the formation of secondary phases. However, for higher La concentrations ($>1/4$) a small amount was always present. It was tried to obtain Dy and Er hexaferrite by the same method. The temperature range of stability of this phase is unknown, therefore several temperatures were tried, without success.

Subsequently these samples were characterized by XRD in order to determine the phases and observe changes in the lattice parameters with the substitution. A lattice distortion of the pure La hexaferrite was observed at low temperatures by neutron diffraction. Information about the local Fe environment were obtained by NMR and Mössbauer spectroscopy and delivered important results about the valence state of the Fe ions and changes due to the lattice distortion. Bulk properties like the density were measured and compared with the X-ray density. The electrical resistivity was measured in zero field from room temperature down to 30 K and showed a decreased resistivity with increasing La concentration. Magnetic properties were determined with different techniques. The anisotropy was measured by using singular point detection from room temperature down to 4.2 K. It showed a strong increase with decreasing temperature for the pure La hexaferrite, still an increase for the sample with a La concentration of $\text{La}/\text{Sr}=3/1$, but a decrease for all smaller concentrations. It was possible to give a qualitative explanation of this behavior. Magnetization curves were measured at room temperature and at 4.2 K. The coercivity was observed to be very

small, which could be explained by the big grains formed due to the heat treatment at high temperatures. The saturation magnetization showed only small decrease with the La concentration.

In the last part the electron structure was calculated with the program Wien2k based on the density functional theory. Different methods were compared. The density of states and the local magnetic moments were obtained and compared with the experiments. These first calculations provide the basis for calculations of anisotropy and hyperfine fields, which may explain the experimentally observed behavior.

Acknowledgement

First of all I want to thank my advisor Prof. Roland Grössinger for the opportunity to make the doctoral thesis and the interesting topic he proposed. Thanks to his contacts I had the chance to collaborate with other instituts and make first experiences abroad. He encouraged me to obtain autonomy with publications and presentations of my work at international conferences.

I owe my gratitude also to my co-assessor Dr. Martin W. Pieper, who continuously stimulated me to obtain better physical understanding. He was a main initiator for physical interpretation of the experiments performed within my work and discussions with him were always a source of motivation. I also have to thank him for the NMR measurements he performed.

I am deeply in dept of gratitude with all the people at the Department of Solid State Physics at the TU Vienna, who helped me with the experimental work. Especially I want to mention here Prof. Günter Wiesinger and Prof. Michael Reissner.

I thank also my external collaborators Prof. Christian Edtmaier (Department of Chemical Technologies and Analytics, TU Vienna), MSc. Veronica Corral Flores, Dr. Dario Bueno Baques and Dr. José Matutes Aquino (CIMAV, Chihuahua, Mexico), Dr. Pavel Novák and Dr. Karel Knížek (Institute of Physics of ASCR, Praha, Czech Republic) and Dr. Clemens Ritter (Institute Laue Langevin, Grenoble, France).

My deep thanks to all my friends and colleagues, who were able to stand me especially in the last stressing period of my Ph.D. Special thanks to Michael and Thomas for their technical support.

Special gratitude I owe my parents, who supported me in all belongings and never doubted my decisions.

Finally I want to thank Claudio, who put a lot of trust in my scientific abilities and helped me through periods with a lack of motivation.

Contents

1	Introduction	15
2	Magnetism and magnetic materials	19
2.1	Magnetism and solid state physics	19
2.1.1	Magnetic moments	19
2.1.2	Magnetic interaction	20
2.1.3	Anisotropy	23
2.1.4	Hysteresis loop and coercivity processes	30
2.1.5	Debye model	32
2.1.6	Density functional theory	33
2.2	Magnetic materials - Hexaferrites	36
2.2.1	Crystal structure	37
2.2.2	Magnetic structure and magnetic properties	39
2.2.3	Substituted M-type hexaferrites	42
3	Preparation and characterization techniques	47
3.1	Investigated compounds and preparation techniques	47
3.1.1	La hexaferrite and La substituted Sr hexaferrite	47
3.1.2	Rare earth substituted Sr hexaferrite	57
3.2	Characterization techniques	59
3.2.1	X-ray diffraction	59
3.2.2	Neutron diffraction	59
3.2.3	Microscopy	60
3.2.4	Density	60
3.2.5	Resistivity measurement	61
3.2.6	Calorimetry	62

3.2.7	Pulsed field magnetometer	63
3.2.8	Vibrating Sample Magnetometer	64
3.2.9	Susceptometer	65
3.2.10	Mössbauer spectroscopy	66
3.2.11	Nuclear magnetic resonance	68
4	Experimental results and discussion	73
4.1	La hexaferrite	73
4.1.1	Structural properties	73
4.1.2	Electronic properties	85
4.1.3	Magnetic properties	88
4.1.4	Local probes	97
4.2	La substituted Sr hexaferrite	109
4.2.1	Structural properties	109
4.2.2	Electronic properties	116
4.2.3	Magnetic properties	118
4.2.4	Local probes	126
4.3	Rare earth substituted Sr hexaferrite	135
4.3.1	Structural properties	135
4.3.2	Magnetic properties	136
4.3.3	Local probes	144
5	Electron structure calculations	151
5.1	Introduction	151
5.2	Calculation method	152
5.2.1	Mixed valence region - La substituted Sr ferrite	154
5.3	Results and discussion	155
5.3.1	Sr hexaferrite	155
5.3.2	La substituted Sr hexaferrite	159
6	Conclusion	167
6.1	First studies	167
6.2	Preparation	168
6.3	Structural properties	169
6.4	Magnetic properties	170

6.4.1	Anisotropy	170
6.4.2	Magnetization and coercivity	171
6.5	Electron structure calculations	172

Chapter 1

Introduction

Permanent magnetic materials are part of our every day life and with the increasing introduction of electronics in households, transport, but also industrial applications, there is an increasing demand for magnetic materials. For example the average car contains around fifty magnets, the number increasing, ranging from small motors for the electrical window lift to sensors and actuators. But besides the well known motors, there is a huge variety of other applications, stimulated essentially by the development of new and better performing magnetic materials. In the 1970's and 1980's the rare earth magnets, Sm-Co and Nd-Fe-B compounds, were found, which decreased significantly the size of the magnets, due to their higher energy density, and enabled so a miniaturizing of electronic devices. These materials partly replaced the former permanent magnets Alnico and the hexaferrites $\text{BaFe}_{12}\text{O}_{19}$ and $\text{SrFe}_{12}\text{O}_{19}$ [1].

M-type hexaferrites were discovered in the 1950's in the research laboratories of Philips [2]. Due to the fact that they are ferrimagnetic their magnetization is comparably low and also the coercivity is ten times lower than the one of the rare earth compounds. Nevertheless hexaferrites are still covering more than 50% of the permanent magnet market. The main reason is the low costs, since rare earth elements are very expensive, while for ferrites the main starting material is the cheap iron oxide. Another reason is the chemical stability of ferrites in contrast to the rare earth compounds, which oxidize easily. This makes also their handling simple and therefore

production processes are facile. A further advantage is the fact that oxides are insulating which is attractive for rf-applications [3]. Additional interest was paid few years ago to the properties of small particles or thin films based on hard magnetic ferrites, since they might be used as a disk medium. Hexaferrites were also discovered recently as multifunctional materials, exhibiting a strong magnetoelectrical effect [4]. This proves that although they appear as well known material, further investigations may still lead to remarkable results.

Because of their technical importance any improvement of the properties of the M-type ferrites is of relevance for the large market. Therefore, many attempts have been made to improve their magnetic properties by doping and substitutions within the complex structure, for the Ba or Sr ion as well as for the Fe ions. But most types of substitutions investigated up to now, such as e.g. Fe by Al, or Co and Ti, either cause a decrease of the saturation magnetization, or a drastic reduction of the magnetocrystalline anisotropy (for a survey see [5]). Since magnetocrystalline anisotropy determines mainly the coercivity, this also leads to a decrease of coercivity and, therefore, a reduction of the energy product of the permanent magnet. However, a very early work showing improved hard magnetic properties in samples doped simultaneously with La and Co went unnoticed [6], so it came as surprise when the significant increase in room temperature coercivity upon La-Co substitution was rediscovered [7], causing a remarkable comeback of research activities in substituted ferrites. The increase in coercivity was explained by an increase in anisotropy due to the orbital momentum of the Co^{2+} ion. The research included investigations of rare earth substituted hexaferrites [8, 9, 10], following early publications like e.g. [11], which are interesting also due to a possible contribution of the magnetic moment of the rare earth element, most likely at low temperatures. Among the rare earth substitutions the complete substitution of Sr or Ba by La was promising, despite the missing magnetic moment, due to a very high anisotropy at low temperatures of this compound reported already in 1974 by Lotgering [12]. While the La-Co substituted ferrites exhibited a significant increase in anisotropy, the rare earth doped compounds did not show any significant change in magnetic properties [13]. Especially for La this was unexpected, in view of the results

of Lotgering.

This work was started in order to clarify the role of the rare earth element in substituted M-type hexaferrites in enhancing magnetocrystalline anisotropy. For this reason rare earth substituted ferrites prepared by hydrothermal synthesis [14] were obtained and investigated for their magnetic properties. In order to check the publication of Lotgering, La hexaferrite was prepared using different methods. These samples were examined by spectroscopic methods like nuclear magnetic resonance, neutron diffraction and Mössbauer spectroscopy, together with measurements of temperature dependent anisotropy and the low temperature hysteresis loop. In order to arrive at a microscopic understanding of the large anisotropy enhancement by La substitution, samples of partly La substituted Sr ferrite with various La concentrations were prepared, using the same methods as for pure LaM, and the change in magnetic properties observed.

A comparison with band structure calculations with respect to the La concentration, yielding the local magnetic moments at the different Fe sublattices, was performed. From these investigations considerable insight is obtained on the interplay between orbital, magnetic and structural degrees of freedom in the hexaferrites.

This research gives a contribution to explain how the properties of M-type hexaferrites change with rare earth substitution of the Sr or Ba ion, and if an improvement with respect to the parent compound is possible.

Chapter 2

Magnetism and magnetic materials

2.1 Magnetism and solid state physics

This chapter is intended as a survey of certain topics related to magnetism and solid state physics, with the aim to let the reader better understand the content of following chapters.

2.1.1 Magnetic moments

The magnetism of materials is caused by the magnetic moments of the electrons. There exist two type of magnetic moments: the spin moment

$$\vec{\mu}_s = -g\mu_B\vec{S},$$

where $\mu_B = \frac{e\hbar}{2m} = 0.92710^{-23} \text{ Am}^2$ is the Bohr magneton, which is the elementary magnetic moment of an electron, and g is the gyromagnetic ratio given by $g = 2.0023$, containing a correction of the Dirac value for the interaction with electromagnetic fields, and the orbital moment

$$\vec{\mu}_l = -\frac{e}{2}(\vec{r} \times \vec{v}) = -\mu_B\vec{l}.$$

Also the nucleus has a magnetic moment, given by

$$\vec{\mu}_n = g_N \mu_N \vec{I},$$

where μ_N contains the proton mass instead of the electron mass and is therefore $1/1836$ of μ_B , and g_N is of order of 1.

The magnetic moment of a free ion is given by the sum of all electron contributions. Taking into account the Pauli exclusion principle and the Coulomb interaction, Hund's rules postulate lowest energy for maximum spin and maximum orbital momentum. Since the magnetic field generated by the orbital momentum acts on the spin and vice versa, also this interaction, called LS coupling, has to be considered. The term in the Hamiltonian related to LS coupling is $H_{so} = \lambda \vec{L} \cdot \vec{S}$, where \vec{L} and \vec{S} are the total orbital momentum and the spin moment. With LS coupling \vec{L} and \vec{S} are no longer constants of motion, therefore one defines a vector $\vec{J} = \vec{L} + \vec{S}$, which is a good quantum number. The total magnetic moment is parallel to this vector

$$\vec{M} = -g_J \mu_B \vec{J},$$

where $g_J = 1 + \frac{J(J+1)+S(S+1)-L(L+1)}{2J(J+1)}$ is the Landé factor. This correlation is valid for the rare earth elements. For the 3d elements the crystal field is stronger than the LS coupling (see later chapter 2.1.3), so that the magnetic moment is given by

$$\vec{M} = -\mu_B(2\vec{S} + \vec{L}),$$

where \vec{L} and \vec{S} are determined by the crystal field ground state and H_{so} has to be treated by perturbation theory.

A table with the quantum numbers and magnetic moments of certain ions is shown below (see tab.2.1).

2.1.2 Magnetic interaction

Interactions between electronic moments

There are two types of magnetic interactions including only electronic magnetic moments. The dipole-dipole interaction (see later chapter 2.1.3), due

Table 2.1: Quantum numbers of spin and orbital moment of certain free ions of the 3d and 4f group

ion	configuration	S	L	J	ground state	M_s [μ_B]
Fe ³⁺	3d ⁵ 4s ²	5/2	0	5/2	⁶ S _{5/2}	5
Fe ²⁺	3d ⁶ 4s ²	2	2	4	⁵ D ₄	4
Co ²⁺	3d ⁷ 4s ²	3/2	3	9/2	⁴ F _{9/2}	4
La ³⁺	5s ² 5p ⁶	0	0	0	¹ S ₀	0
Er ³⁺	4f ¹¹ 5s ² 5p ⁶	3/2	6	15/2	⁴ I _{15/2}	3
Dy ³⁺	4f ⁹ 5s ² 5p ⁶	5/2	5	15/2	⁶ H _{15/2}	5
Sm ³⁺	4f ⁵ 5s ² 5p ⁶	5/2	5	5/2	⁶ H _{5/2}	5
Nd ³⁺	4f ³ 5s ² 5p ⁶	3/2	6	9/2	⁴ I _{9/2}	3
Pr ³⁺	4f ² 5s ² 5p ⁶	1	5	4	³ H ₄	2

to the magnetic field of a magnetic moment that acts on other magnetic moments. This is a long range interaction, but very weak. Usually the thermal energy $k_B T$ is larger than the dipole energy, so that no alignment due to the dipole-dipole interaction occurs. Therefore this interaction is also neglected for paramagnetic materials.

The interaction that causes a spontaneous magnetization is the exchange interaction between spin moments. It is characterized by the Heisenberg Hamiltonian

$$H = - \sum_{ij} J_{ij} \vec{S}_i \cdot \vec{S}_j,$$

where J_{ij} is the exchange integral. Since the exchange interaction is short ranged, it is usually sufficient to consider only the nearest neighbors in the summation. For $J_{ij} > 0$ the minimum energy is given by a parallel alignment of spins, which corresponds to ferromagnetism, while for $J_{ij} < 0$ it corresponds to antiparallel alignment (antiferromagnetism).

From a macroscopic point of view this can be described in analogy to paramagnetism with a field, produced by all spins, acting on another spin. It is reasonable to assume that this field is proportional to the magnetization

and therefore Weiss postulated

$$H_W = N_W M,$$

called Weiss' molecular field. From the paramagnetic analogy we find

$$M(H, T) = M_0 \tanh\left(\frac{\mu_0 m}{k_B T} (H + H_W(M))\right),$$

with the molecular field acting on the magnetic moments in addition to an external field H . From this the Curie-Weiss law for $T > T_C$ is derived

$$\chi = \frac{C}{T - T_C},$$

where T_C is the Curie temperature, below which spontaneous magnetic ordering occurs.

The direct exchange interaction derives from the Coulomb interaction between localized d electrons on neighboring ions. There exists also an indirect exchange via neighboring non magnetic anions, that is called superexchange [15]. It is an exchange between non neighboring ions and, therefore, longer ranged. Usually superexchange is antiferromagnetic and is common for many Fe oxides. There the 3d orbital of the Fe overlaps with the 2p orbital of O. Due to Pauli exclusion the electrons in one shell can only have antiparallel spins. This leads to the antiferromagnetic exchange.

There exists also a form of anisotropic exchange, an interaction between an excited state of one ion with the ground state of another. This leads to an exchange that prefers perpendicular orientation of the spins and therefore leads to canted spins. It occurs mainly in antiferromagnets and results in a small magnetization, which is known as weak ferromagnetism [16].

Interaction between electronic and nuclear moments

The interaction between electron and nuclear moment is given by the dipole-dipole interaction between spin moment of the electron and nuclear magnetic moment, by the Fermi contact term and by the interaction of the nuclear moment with the magnetic field produced by the orbital momentum of the

electrons. The Fermi contact term $-\frac{8\pi}{3}\vec{s} \cdot \vec{\mu}_N\delta(\vec{r})$ is necessary, since the dipole-dipole term is not valid for $r = 0$, and describes the interaction of the nucleus with electrons, that have a non vanishing probability at the nucleus position. These are the s electrons. For 3d electrons this probability vanishes. Nevertheless the Fermi contact term is important for the iron-group ions, due to the so called core polarization. The strong exchange interaction between the 3d electrons and the inner s cores, leads to a concentration of s spins antiparallel to the 3d polarization at the nucleus site, while the parallel spins are more far. This causes a local magnetic polarization at the nucleus site. The total magnetic interaction is given in 2.1.

$$\sum_i g\mu_B \left\{ \left[\frac{(\vec{l}_i - \vec{s}_i) \cdot \vec{\mu}_n}{r_i^3} + 3\frac{1}{r_i^5}(\vec{s}_i \cdot \vec{r}_i)(\vec{\mu}_n \cdot \vec{r}_i) \right] + \frac{8\pi}{3}(\vec{s}_i \cdot \vec{\mu}_n)\delta(\vec{r}_i) \right\} \quad (2.1)$$

It is important to note the different signs of spin- and orbital-interaction with the nuclear magnetic moment, which leads to opposite signs in the hyperfine field H_{hf} , given by

$$E = -\mu_0\mu_n H_{hf}.$$

The Hamiltonian can be easily described by the hyperfine parameters

$$H_i = \sum_j (I_i A_{ij} S_j - I_i B_{ij} L_j).$$

Neglecting the orbital term it leads to $\vec{H}_{hf} = \alpha\vec{M}$, with the hyperfine coupling constant α . The hyperfine interaction causes a splitting of energy levels of the nucleus.

2.1.3 Anisotropy

An energetical preference of the magnetization for a certain direction is called anisotropy. The simplest case is a uniaxial anisotropy, where the energy is minimum for the magnetization pointing along one certain axis in space. It is possible to define this direction as the z-axis and describe the anisotropy energy by a series expansion with variable θ , which is the angle between the

magnetization vector and the so called easy axis, where the energy is zero.

$$E_A = K_1 \sin^2 \theta + K_2 \sin^4 \theta + \dots \quad (2.2)$$

In the case of a hexagonal crystal we can write 2.2 in the form [17]

$$E_A = K_1 \sin^2 \theta + K_2 \sin^4 \theta + K_3 \sin^6 \theta + K'_3 \sin^6 \theta \cos^4 \phi \quad (2.3)$$

neglecting terms of higher order. Here we have already to distinguish two different types of anisotropy, easy axis anisotropy as described before, when

$$K_1 > 0 \quad \text{and} \quad K_1 + K_2 > 0$$

and easy plane anisotropy, where an orientation in the basal plane is preferred, when

$$0 \leq K_1 < -K_2 \quad \text{or} \quad -K_1 > 2K_2 \quad \text{and} \quad K_1 < 0.$$

A magnetic field that is strong enough to rotate the magnetization from the easy axis into a perpendicular hard axis is called anisotropy field and is related to the anisotropy energy through

$$H_A = \frac{1}{\mu_0 M_S} \left(\frac{\partial^2 E_A}{\partial \theta^2} \right)_{\theta=0} \quad (2.4)$$

This derives from the torque acting on the magnetization in an external field, given by

$$T_H = \frac{\partial E_H}{\partial \theta} = -\frac{\partial}{\partial \theta} \mu_0 H M_S \cos \theta,$$

Replacing the energy by the anisotropy energy and considering only small angles it can be expanded

$$T_A = \left(\frac{\partial E_A}{\partial \theta} \right)_{\theta=0} + \left(\frac{\partial^2 E_A}{\partial \theta^2} \right)_{\theta=0} \Delta \theta,$$

neglecting terms of higher order. Since $\left(\frac{\partial E_A}{\partial \theta}\right)_{\theta=0} = 0$ this leads to

$$\mu_0 H_A M_S \Delta \theta = \left(\frac{\partial^2 E_A}{\partial \theta^2}\right)_{\theta=0} \Delta \theta,$$

delivering 2.4. For [100] easy direction the anisotropy field is

$$H_A = \frac{2K_1}{\mu_0 M_S}, \quad (2.5)$$

where anisotropy constants of higher order are equal zero.

Besides easy axis and easy plane there exist also other types of anisotropy like e.g. easy cone, where the magnetization orientates along a cone. The type is determined by the ratios of the anisotropy constants K_i/K_1 , which can also change with temperature. Therefore temperature dependent changes of the anisotropy type occur in some compounds.

The mechanisms that cause magnetic anisotropy are of different origin. The only intrinsic property causing anisotropy is the magnetocrystalline anisotropy, due to a coupling of the magnetic moments to the lattice symmetry. The microstructure plays an important role leading to shape anisotropy caused by deviations of the particles from spherical shape. And then there are several forms of induced anisotropy, when a sample is exposed to stress or an external field during heat treatment.

Shape anisotropy

Shape anisotropy arises from the fact that every magnetized particle generates a demagnetizing field on average antiparallel to the magnetization. This can be easily imagined, thinking of the Maxwell equation

$$\text{div} \vec{B} = 0$$

which means that the field lines are always closed. This demagnetizing field is defined for ellipsoidal particles by

$$\vec{H}_D = -N_{ij} \vec{M}_S, \quad (2.6)$$

where N_{ij} ($i, j = x, y, z$) is a second order tensor. Assuming an ellipsoidal particle with the cartesian coordinates along the principal axis a, b, c , N_{ij} is unequal zero only for the diagonal elements of the matrix with the constraint $N_a + N_b + N_c = 1$. The magnetostatic energy of a uniformly magnetized body in its own demagnetizing field is, therefore

$$U_M = -\frac{\mu_0}{2} \int_V \vec{H}_D \vec{M} d^3r = \frac{\mu_0}{2} V N M^2 \quad (2.7)$$

for a sphere or, more general,

$$\frac{U_M}{V} = \frac{\mu_0}{2} (N_a M_x^2 + N_b M_y^2 + N_c M_z^2). \quad (2.8)$$

For a spheroid with two principal axes equal and a rotational symmetry around the third, the energy density 2.8 can be rewritten as

$$f_M = \frac{\mu_0 M_S^2}{2} (N_{\perp} \sin^2 \theta + N_{\parallel} \cos^2 \theta)$$

and the corresponding anisotropy constant is in comparison with 2.2

$$K_M = \frac{\mu_0 M_S^2}{2} (N_{\perp} - N_{\parallel}).$$

For a prolate spheroid, where $N_{\perp} > N_{\parallel}$ and $N_{\parallel} < 1/3$, this results in easy axis anisotropy, while for a oblate spheroid with $N_{\perp} < N_{\parallel}$ and $N_{\parallel} > 1/3$ we have easy plane anisotropy in the plane perpendicular to the symmetry axis.

The shape anisotropy is one of the reasons why microstructure plays an important role for the anisotropy of a material, since for single domain particles, the shape and alignment of the particles is essential. However shape anisotropy is limited by M_S and therefore in many cases $H_D < H_A$, so that the magnetocrystalline anisotropy determines the total anisotropy.

Dipole-dipole anisotropy

The dipolar field caused by a magnetic moment \vec{m}_i is given by

$$\vec{B}_i = \frac{\mu_0}{4\pi} \left(\frac{3\vec{r}(\vec{r} \cdot \vec{m}_i)}{r^5} - \frac{\vec{m}_i}{r^3} \right).$$

Bringing another magnetic moment \vec{m}_j close, it will interact with this field with a potential energy of $-\vec{m}_j \cdot \vec{B}_i$. Taking into account that there are several magnetic moments surrounding, we have to sum up all dipole fields. The average magnetostatic field, which is equal to $\vec{B}_M = \mu_0(\vec{H}_M + \vec{M})$, is then

$$\vec{B}_M = \frac{1}{\Delta V} \int_{\Delta V} \sum_i \vec{B}_i d^3r, \quad (2.9)$$

used in 2.7. This field is in general anisotropic and causes therefore an orientation preference of a magnetic moment. Only for a sphere the Lorentz field ($\frac{\mu_0}{3}\vec{M}$), which is the magnetic field in a spherical cavity of a magnetized material, and the demagnetizing field cancel each other and the dipole field is equal zero. An example for this are ferrites with spinel structure.

Two types of anisotropy based on the same interaction can be derived from 2.9. One is the dipole-dipole anisotropy, integrating over a spherical volume of an assembly of dipole moments in an arbitrary symmetry. The other one is the shape anisotropy, where a cubic symmetry is assumed and the integration volume deviates from a sphere.

Magnetocrystalline anisotropy

In a crystal lattice the magnetic moment of an ion is influenced by the electrical field of the surrounding atoms at the ion position. This so called crystal field creates, due to an interaction with the orbital momentum and the LS coupling, a preferred orientation of the spins according to the symmetry of the ion site, which is called magnetocrystalline anisotropy. We distinguish two cases depending on the relative strength of crystal-field and spin-orbit-coupling. When the crystal field is stronger than the spin-orbit-coupling the orbital momentum is rigidly tied to the lattice and the anisotropy energy is determined by the variation of the spin-orbit energy proportional to $\vec{L} \cdot \vec{S}$ with fixed \vec{L} , and with \vec{S} rotating with \vec{M} . In the other case \vec{L} follows \vec{S} and the anisotropy energy is determined by the variation of \vec{L} with respect to the lattice. The crystal field is proportional to a positive power of the electron orbit radius, while the LS coupling is proportional to $1/r^3$. An example for the first case are therefore the iron group ions, with a large orbit, since the 3d shell is screened from the nucleus attraction by the 4s shell. On the other

hand the rare earth ions belong to the latter case, because the 4f shell is located inside the 5s shell, and therefore the effective nucleus charge is large and the orbit small.

In the case of the iron group the crystal field effect is not only an electrostatic one. More important is a direct mixing of the 3d orbitals with the 2p orbitals of the surrounding O^{2-} ions. This leads in cubic symmetry (like an octahedral site) to a splitting of the degenerate 3d energy levels in a 2-fold degenerate $d\gamma$ (e_g) level or Γ_3 with higher energy, including the wave functions or orbitals $\phi_{x^2-y^2}$ and ϕ_0 , and a 3-fold degenerate level $d\epsilon$ (t_{2g}) or Γ_5 with lower energy, including ϕ_{xy} , ϕ_{yz} and ϕ_{zx} (see fig.2.1 and fig.2.2). This is also the energy level splitting for the half filled Fe^{3+} ion, where Hund's first rule is fulfilled maximizing S, but $L=0$. If we have to consider Hund's second rule, which is a consequence of electrostatic repulsion due to the Coulomb interaction of the electrons, filling up the 3d shell with further electrons, the splitting changes. The same splitting still occurs for the $3d^6$ configuration that we find in Fe^{2+} , but for the $3d^7$ with $L=3$ the splitting changes in a 3-fold degenerate Γ_4 with lowest energy, a 3-fold degenerate Γ_5 and a non degenerate Γ_2 with highest energy. This corresponds to the Co^{2+} ion in octahedral environment.

For a non degenerate ground state like in $3d^8$ or $3d^3$ the expectation value of the angular momentum operator is always zero. This is called quenching of the orbital momentum. Indeed, in many cases the ground state is non degenerate, since there is always a crystal field of lower symmetry present, that splits the lowest energy level. In this case the anisotropy Hamiltonian can be derived by treating the LS coupling and the Zeeman energy in second order perturbation theory. If in addition to $L=0$ the site symmetry is cubic, the anisotropy shows up only in fourth order perturbation [19]. This applies to the Fe^{3+} ion at octahedral sites, as they are in many ferrites.

In the case that due to the crystal field splitting ground state is still degenerate, the degeneracy is further lifted by the LS coupling. The orbital state is strongly coupled to the lattice, so that any distortion of the lattice will also lead to a splitting of energy levels. The lifting of an orbital degeneracy by the interaction between a lattice distortion and the orbital state is called Jahn-Teller effect. An example is Co^{2+} in an octahedral environment, like

saturation

$$I = I_S(1 - A/H - B/H^2 - C/H^3) + \chi H + D\sqrt{H}, \quad (2.10)$$

I_S is the saturation polarisation, A is describing inhomogeneities due to e.g. impurities, B is proportional to the square of the uniaxial anisotropy constant K^2 , C is proportional to K^3 , χ is a paramagnetic susceptibility and D is the spin wave factor. For hexaferrites a good fit can be obtained neglecting the last two terms and $A, B, C > 0$, with B is the main parameter [23]. For determining I_S it is sufficient to reduce 2.10 to

$$I = I_S(1 - B/H^2).$$

I_S and B can then be determined from a plot of I versus $1/H^2$.

2.1.5 Debye model

In the Debye model an upper frequency limit is defined for the continuous, dispersion free phonon modes. This limit is often characterized by the Debye temperature

$$\Theta_D = \frac{\hbar\Omega_D}{k_B},$$

where Ω_D is a material constant, depending on the particle density and the velocity of sound (and therefore the elastic constants). Integration over the density of states for the phonon oscillations, which is quadratic in the Debye approximation, leads then to the thermal energy. From this the part of the specific heat, that is caused only by phonons can be derived. In the high temperature limit $T \gg \Theta_D$ this leads to a constant value for the specific heat

$$C_V = 3N^3k_B.$$

In the low temperature limit it leads to a Debye function for the thermal energy

$$E_{th} = \frac{9N^3k_B T^4}{\Theta_D^3} \int_0^{x_D} \frac{x^3}{e^x - 1} dx,$$

be obtained [20] and exhibit a strong effect at low temperatures depending mainly on the LS coupling parameter λ and on α . This is a parameter that describes the effective orbital moment due to the orbital moment of the Co ion interacting with the crystal field. For the Fe^{2+} ion in magnetite the lowest energy state is Γ_5 instead of Γ_4 due to the cubic crystal field (see fig.2.2) and is further split to a nondegenerate ground state and a doublet by the trigonal field and second order perturbation has to be applied. This is the reason, why only the Co substituted spinel ferrite exhibits a large anisotropy: For Co^{2+} the angular orbital momentum appears in first order perturbation. The same argument was applied to the La-Co substituted hexaferrites (see chapter 2.2).

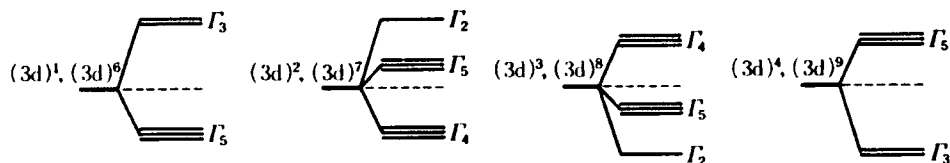


Figure 2.2: Splitting of the many electron energy levels of the 3d orbital [21]

2.1.4 Hysteresis loop and coercivity processes

Fig.2.3 shows a typical hysteresis loop for a ferromagnetic material. The saturation magnetization M_S , the maximum magnetization, the remanence, the magnetization value for zero internal field, and the coercivity, the field of zero magnetization, are shown. These parameters are used to characterize a hard magnetic material. The shape of the hysteresis contains a lot of information, including the shape of the sample, the magnetic phases, the anisotropy, the stored energy and the magnetization process. We distinguish in principle two steps of the magnetization process. The first in the steep part of the hysteresis loop is due to domain wall motion, where domains of less preferred orientation shrink and the ones in preferred orientation grow. The second step is in the very flat part of the hysteresis, at high external fields, where rotation of the magnetization in order to align with the external field occurs. To manage this the energy provided by the external field

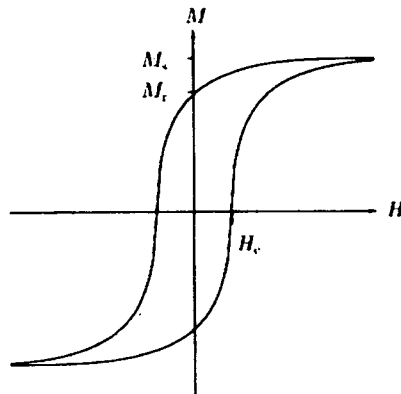


Figure 2.3: Typical hysteresis loop of a ferromagnetic material [16]

has to be higher than the anisotropy energy. Therefore saturation magnetization can be reached at much lower fields if the sample is aligned with the easy axis parallel to the external field. The coercivity, which is a measure for the energy needed to reverse magnetization, is mainly determined by domain wall motion and therefore by pinning effects due to impurities, strains and surfaces. If one would consider only rotation processes, like in a Stoner Wohlfahrt model [22], where single domain particles without interaction but uniaxial anisotropy are assumed, the coercivity is represented by the anisotropy field. In general the situation is more complicated and since domain wall motion requires less energy, the anisotropy field is only an upper limit. While the domain wall can easily move within a particle it will face a energy barrier at the particle surface. That is the reason why the coercivity is reciprocally proportional to the grain size, for grains in the range of μm . For very small grains (in the nm range) no domains occur, since the energy gain does not outweigh the magnetostatic energy loss. Considering in this case also exchange coupling between the sufficiently isolated grains leads to the strong decrease in coercivity with decreasing grain size, which was observed in nanocrystalline materials.

The saturation magnetization is defined as the magnetization at $H = \infty$. It can be determined from the hysteresis loop, using the law of approach to

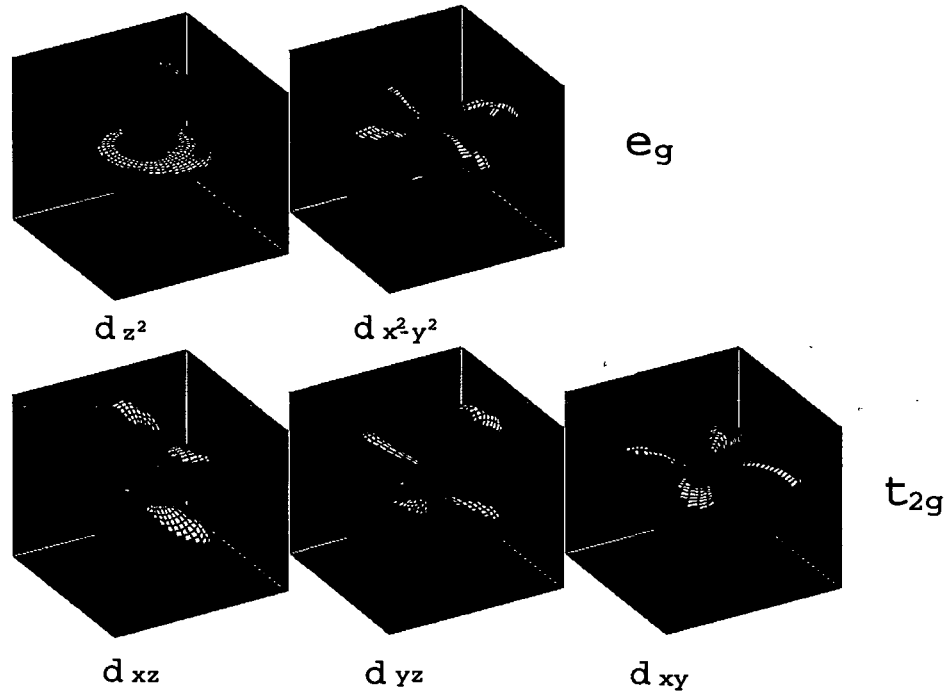


Figure 2.1: Shape of the orbitals with $L=2$; the 3d orbitals are grouped in e_g and t_{2g} , which are split in a cubic crystal field [18]

in the Co substituted magnetite. Here the energy levels of the free ion are primarily split by the cubic crystal field, then by the trigonal distortion, that splits Γ_4 in a doublet with lower energy and a singlet with higher energy, and these are finally split by the exchange coupling and the spin-orbit-coupling. The anisotropy energy is given by a part of the Helmholtz free energy given by

$$F = -k_B T \sum_i N_i \ln z_i,$$

where N_i is the cobalt population of the sublattice and z_i is the partition function given by

$$z_i = \sum_j e^{\frac{-\epsilon_j(\theta_i)}{kT}},$$

where ϵ_j are the split energy levels and θ_i is the angle between \vec{M} and the trigonal axis. From this, the temperature dependent anisotropy constants can

where $x = \frac{\hbar\Omega}{k_B T}$ and the Debye T^3 -law describing the phonon contribution of the specific heat

$$C_V = \frac{12\pi^4 N^3}{5} k_B \frac{T^3}{\Theta_D^3}.$$

The Debye model can be also used for calculating the intensity loss in diffraction experiments due to the oscillations of the atoms in a crystal lattice. Assuming a harmonic oscillation the intensity is reduced by a factor

$$f = e^{-\frac{1}{3}\langle x^2 \rangle G^2}, \quad (2.11)$$

where $\langle x^2 \rangle$ is the mean squared deflection and G is the lattice vector of the reflex. f is called Debye-Waller factor and is calculated with the Debye model to

$$f = e^{-3 \frac{(2\pi\hbar)^2}{M k_B \Theta_D} \frac{\sin^2 \theta}{\lambda^2} P\left(\frac{T}{\Theta_D}\right)},$$

where $P = 1 + 4 \left(\frac{T}{\Theta_D}\right)^2 \cdot \int_0^{\Theta_D/T} \frac{y}{e^y - 1} dy$. The Debye-Waller factor is related to the lattice bonding, the stronger the bonding, the smaller the Debye-Waller factor.

2.1.6 Density functional theory

For calculations of the electron structure in solid matter it is necessary to solve the quantum many body problem. The exact many particle Hamiltonian contains beside the kinetic energies of the ZN electrons and N nuclei all Coulomb interactions of electron-electron-, nucleus-nucleus- and electron-nucleus-type. It is impossible to solve this problem exactly for a realistic number of particles and therefore several approximations are made [24].

The first is the Born-Oppenheimer approximation, where the fact that the nuclei are much heavier than the electrons is considered. Hence the kinetic energy of the nuclei is assumed to be zero and the nucleus-nucleus interaction is reduced to a constant. In the Hamiltonian the influence of the nuclei on the electrons appears then in form of an external potential.

The second approximation is based on the first Hohenberg-Kohn theorem [25], that asserts a one-to-one correspondence between ground state density of a many electron system and this external potential. The second theorem

gives the ground state total energy as

$$E_{V_{ext}}[\rho] = F_{HK}[\rho] + \int \rho(\vec{r})V_{ext}(\vec{r})d\vec{r},$$

where F_{HK} is the Hohenberg-Kohn density functional, which is universal for any many electron system. These two theorems established the density functional theory (DFT).

The equations published by Kohn and Sham [26] turned DFT in a practical tool. According to their theorem the ground state density is given by

$$\rho(\vec{r}) = \sum_{i=1}^N \phi_i(\vec{r})^* \phi_i(\vec{r}),$$

where ϕ_i are the single particle wave functions of the lowest energy solution of the Kohn-Sham Hamiltonian. The Kohn-Sham Hamiltonian considers the electrons as a non interacting electron gas in two potentials, one due to the nuclei and one due to exchange and correlation effects. Now the problem is reduced to solving single particle Schrödinger like equations, which can be done in a self consistent way starting from a reasonable guess for the density and perform several iterations. The problem is that the second potential is not known and therefore another approximation has to be made. One is the so called local (spin) density approximation (L(S)DA), where the (spin) density is assumed to be constant in infinitesimally small volumes. Each such volume contributes to the total exchange correlation energy by an amount equal to the exchange correlation energy of an identical volume filled with a homogeneous electron gas, that has the same overall density as the original material has in this volume. This method performs well for systems with slowly varying density. Another approach is to make the exchange-correlation contribution of every infinitesimal volume not only dependent on the local density in that volume, but also on the density in the neighbouring volumes. In other words, the gradient of the density will play a role. This approximation is therefore called the generalized gradient approximation (GGA). This method is more realistic and performs usually better, but it is not an ab-initio calculation in the strict sense, since the gradient density

is not unique.

The equation can finally be solved by choosing an appropriate set of basis functions. One option is the linearized augmented plane wave (LAPW) method. In this method the space is divided in two regions: non overlapping spheres around each atom with radius R_α , often called muffin tin sphere, and the remaining outside space, called interstitial region. The electron states within the muffin tin sphere are usually the core states, while the ones outside are called valence states. The basis set is then derived from the augmented plane waves (APW)

$$\phi_{\vec{k}}^{\vec{K}}(\vec{r}, E) = \begin{cases} \frac{1}{\sqrt{V}} e^{i(\vec{k}+\vec{K})\cdot\vec{r}} & \vec{r} \in \text{interstitial region} \\ \sum_{l,m} A_{lm}^{\alpha,\vec{k}+\vec{K}} u_l^\alpha(r', E) Y_m^l(\hat{r}') & \vec{r} \in \text{muffin tin region} \end{cases}$$

which are plane waves in the interstitial region and solutions of the Schrödinger equation for a free atom α in the muffin tin region. In this basis set the radial function $u_l^\alpha(r', E)$ is expanded at a fixed energy E_0 and only the linear term is taken into account, which reduces the number of basis functions with respect to the APW and therefore the calculation times. The accuracy of the method is determined by the factor $R_\alpha^{min} K_{max}$, where R_α^{min} is the smallest muffin tin radius and K_{max} is determined by the cut off energy $E = \frac{\hbar^2 K_{max}^2}{2m_e}$ corresponding to a maximum radius in the reciprocal space. This basis set has to be calculated for as many \vec{k} points in the Brillouin zone as necessary to fill it densely enough. Often a local orbital is added in the sphere of each atom α in order to treat two valence functions with the same orbital number.

An improvement is the LDA+U method proposed by Liechtenstein [27]. A Coulomb potential is added to the Hamiltonian described by the Coulomb integral U (Hubbard parameter), corresponding to the repulsive Coulomb force between electrons with opposite spin located at the same site. This is in competition with the interaction of the electrons with the crystal potential. For U much bigger than the crystal potential parameter an isolated ionic state occurs. In the opposite case the electrons will behave as conduction electrons and the repulsive potential is usually treated as a perturbation.

2.2 Magnetic materials - Hexaferrites

The material which is topic of this work belongs to the group of iron oxides with hard magnetic properties. A compound is classified as hard magnetic when it exhibits a hysteresis loop with a large area, which is proportional to the stored energy [28]. Such a material is usually characterized by BH_{max} , but simplified it should have a high remanence and coercivity [29]. Ferrites with spinel structure of the type $MeFe_2O_4$ with $Me=Mn, Fe, Co, Ni, Cu, Zn, Mg, Cd$, with the most known representative magnetite (Fe_3O_4), have usually a very small coercivity in the order of 10^{-4} T. Ferrites with hexagonal structure and easy plane anisotropy also exhibit a small coercivity, while easy axis structures have a coercivity in the order of 10^{-1} T. Hexagonal ferrites are divided in M-type (e.g. $BaFe_{12}O_{19}$), Y-type (e.g. $BaMe_2Fe_{12}O_{22}$, Me is a divalent transition element), W-type (e.g. $BaMe_2Fe_{16}O_{27}$) and Z-type (e.g. $Ba_3Me_2Fe_{24}O_{41}$) structures. For Z-, M- and most of the W-type structures the spontaneous magnetization is parallel to the c-axis, while for Y-type it is perpendicular. Y- and Z-compounds at room temperature exhibit always easy plane anisotropy, W- and M-compounds easy axis anisotropy. Higher magnetization at a comparable anisotropy field shows the M-type compound.

The crystal structure of the M-type hexaferrites corresponds to the one of the mineral magnetoplumbite with the following formula unit $PbFe_{7.5}Mn_{3.5}Al_{0.5}Ti_{0.5}O_{19}$ [30]. The most famous representatives of this group are BaM and SrM, which were synthesized at the Philips laboratory in the 1950's [2]. Still this material covers a big part of the permanent magnet market, although since then better performing compounds were developed. Fig.2.4 shows a comparison of hard magnetic materials with respect to remanence and coercivity. In the 1970's Sm-Co magnets were developed and in the 1980's Nd-Fe-B compounds, which exhibit the highest magnetization value up to now. Compared with these materials ferrites have rather poor magnetic properties, but their main advantage are the low costs (see tab.2.2), since rare earth elements are very expensive, while for ferrites the main starting material is the cheap iron oxide. Besides this, ferrites are as oxides chemically very stable in contrast to the rare earth compounds, that oxidize easily. This makes also their handling simple and therefore production processes are

facile. Another advantage, that made hexaferrites interesting for microwave applications in the last years [31, 3], is the high electrical resistivity. For these reasons there is still a strong industrial interest in advances of hexaferrites.

Table 2.2: Prizes of different permanent magnets [32]

material	prize [\$/kg]
ferrite (standard)	3.5
ferrite (high quality)	4.7
Alnico	45
SmCo ₅	110
Sm ₂ Co ₁₇	130
Nd-Fe-B (standard)	90
Nd-Fe-B (high quality)	150

2.2.1 Crystal structure

Hexagonal ferrites with M-type structure belong to the space group $P6_3/mmc$ (Hermann-Mauguin notation) with the number 194. The unit cell contains two formula units of $XFe_{12}O_{19}$, with $X=Ba, Sr, Pb$. The unit cell is divided in four different lattice modules. A S module with spinel structure and two oxygen layers and S^* , which is rotated 180° , and a R module with two oxygen layers and in between the layer that contains the X ion (see fig.2.5). S has cubic closest package of the oxygen ions, while R has hexagonal closest package, so that cubic and hexagonal structure are alternating according to RSR^*S^* . There are 5 different Fe lattice sites present in the structure with the Wyckoff numbers 2a, 4f1, 12k, 4f2 and 2b. The spinel like module S contains two octahedral sites (2a and 12k) and one tetrahedral (4f1), and the R module one octahedral (4f2) and a bipyramidal site (2b) [34]. The Fe ion at the latter site is surrounded by 5 oxygen ions, building a double pyramid with triangular basis plane, which can be represented as two tetrahedral sites. The iron ion is fluctuating between these two 4e sites [35]. The oxygen ions are distributed between 5 different sites, according to the Wyckoff coefficients 4e,

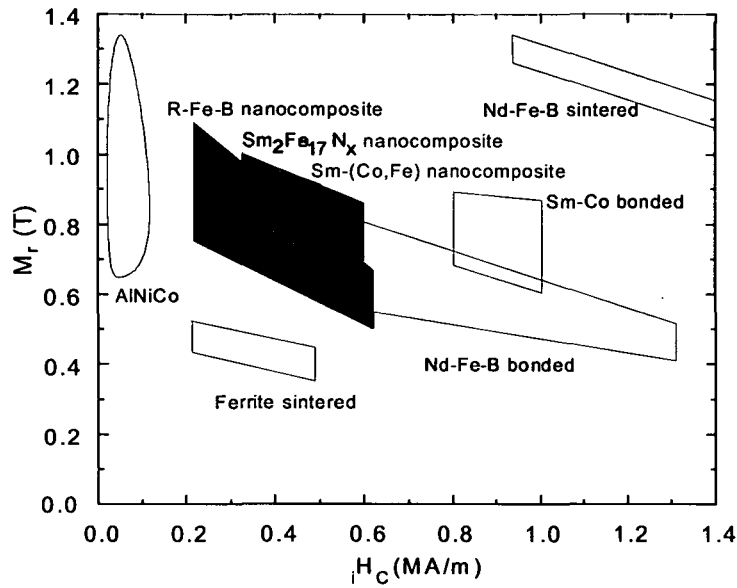


Figure 2.4: Comparison of hard magnetic materials with respect to remanence and coercivity [33]

4f, 6h, 12k1 and 12k2, and the X ion is at the 2d site. The general coordinates of the different Fe sites in the $P6_3/mmc$ structure are shown in tab.2.3. Typical values for the coordinates are $x(12k) = 0.16886 \text{ \AA}$, $z(12k) = 0.89083 \text{ \AA}$, $z(4f1) = 0.02718 \text{ \AA}$ and $z(4f2) = 0.19091 \text{ \AA}$ and for the lattice parameters are $a = b = 5.883 \text{ \AA}$ and $c = 23.037 \text{ \AA}$ (for SrM) [36]. All Fe ions are in the Fe^{3+} state, all O ions in the O^{2-} and X in the 2+ state. A list of ion radii of ions contained in the M-type structure or related ions is shown in tab.2.4.

Table 2.3: Coordinates of Fe sites in $P6_3/mmc$ ferrites [38]

site	x	y	z
2a	0	0	0
2b	0	0	1/4
4f1	1/3	2/3	z
4f2	1/3	2/3	z
12k	x	2x	z

Table 2.4: Ion radii of ions related to the M-type structure [39, 40]

ion	electronic configuration	radius [Å]
Sr ²⁺	[Kr]	1.13
La ³⁺	[Xe]	1.15
Fe ²⁺	[Ar]3d ⁵	0.74
Fe ³⁺	[Ar]3d ⁶	0.64
Co ²⁺	[Ar]3d ⁷	0.72
O ²⁻	[Ne]	1.4

2.2.2 Magnetic structure and magnetic properties

The M-type hexaferrite is a ferrimagnetic compound with all Fe ions in the 3+ state, which give therefore a contribution of $5\mu_B$ to the total magnetization. According to the Gorter model [41], at the sites 2a, 12k and 2b the Fe spin points parallel to the c-axis, at the sites 4f1 and 4f2 it points antiparallel (see fig.2.6). Therefore the total magnetization per unit cell at 0 K is $(12 + 2 + 2) * 5\mu_B - (4 + 4) * 5\mu_B = 40\mu_B$, so $20\mu_B$ per formula unit. The Fe spins are coupled antiparallel via superexchange through the oxygen ions. The exchange parameters were calculated to be larger for angles close to 180° , like for the Fe(2b)-O-Fe(4f2) bond, and negligible small for angles close to 90° , like for the Fe(2a)-O-Fe(12k) bond [42].

The saturation magnetization exhibits an almost linear temperature dependence in the range from 77 K up to 650 K. Curie temperature and magnetization are decreasing with the order of the element X=Sr, Ba, Pb (see tab.2.5).

The anisotropy energy for a hexagonal crystal lattice

$$F = K_1 \sin^2 \theta + K_2 \sin^4 \theta + K_3 \sin^6 \theta + K_4 \sin^6 \theta \cos^6 \phi + \dots \quad (2.12)$$

in the M-type structure is determined by the anisotropy constant K_1 , and exhibits uniaxial anisotropy. This is visible in a measurement of M versus H perpendicular to the easy axis (=c-axis), which exhibits a linear dependence. Such a behavior can be usually explained by a dipole-dipole-interaction, but

Table 2.5: Comparison of saturation magnetization and Curie temperature of the different M-type compounds [5]

compound	$M_S(300\text{ K})$ [Am^2/kg]	$M_S(0\text{ K})$ [Am^2/kg]	θ_C [K]
$\text{SrFe}_{12}\text{O}_{19}$	74.3	104.2	750
$\text{BaFe}_{12}\text{O}_{19}$	72 (380 G)	100	740
$\text{PbFe}_{12}\text{O}_{19}$	320 G	-	725

it was reported, that for the M-type structure it would lead to a negative K_1 due to the interaction of the R and the S module [43]. In more recent publications a positive but very small dipole interaction was reported [44]. Therefore it was assumed that the strong anisotropy must be caused by spin-orbit-interaction, although the Fe^{3+} ion does not exhibit an orbital momentum in the ground state. Wanatabe [45] investigated the excited states of the Fe^{3+} ion and calculated K_1 in a uniaxial crystal field with cubic symmetry. This led to a reasonable positive value of K_1 , under the assumption that a significant amount of excited states exists due to a perturbation by the crystal field. This corresponds to the single ion anisotropy, due to the combined interaction of spin-orbit coupling and the crystal field effect [21]. However, more recent calculations support the idea that the anisotropy of the M-type hexaferrites is caused by the dipole-dipole-interaction, or at least it gives a strong contribution [46].

Which Fe site gives the main contribution to the anisotropy is unclear, too. According to Asti et al.[47], who based their calculation on the Callen and Callen theory [48] for the single ion contribution to the anisotropy, the 12k site is responsible for the high anisotropy. In contradiction You [49, 50] reported the 2b site to give the main contribution.

In the case that only K_1 contributes to the magnetocrystalline anisotropy, the anisotropy field can be calculated by $H_A = \frac{2K_1}{\mu_0 M_S}$ (see chapter 2.1.3). At low temperatures H_A is almost independent of temperature. Tab.2.6 shows values of H_A at 300 K and at 0 K for SrM and BaM.

The grains in M-type hexaferrites have usually platelet structure, with the c-axis along the short diameter, and are typically in the order of 1 μm .

Table 2.6: Anisotropy fields at room temperature and 0 K of the M-type compounds [5]

compound	$\mu_0 H_A(300 \text{ K})$ [T]	$\mu_0 H_A(0 \text{ K})$ [T]
SrFe ₁₂ O ₁₉	1.85	1.65
BaFe ₁₂ O ₁₉	1.68	1.55

Therefore in most cases the condition for single domain particles is fulfilled, calculated by Kittel [51] and Néel [52] to be

$$D = \frac{9}{2\pi} \frac{\sigma_w}{M_S^2} \quad (2.13)$$

for the critical particle diameter. σ_w is the domain wall energy given by

$$\sigma_w = 4(AK)^{1/2} \quad (2.14)$$

with A is the exchange constant and K the anisotropy constant. The single domain diameter is of order of 1 μm for Ba hexaferrite [53]. The coercivity is then determined only by rotation processes and can be written according to the Stoner-Wohlfahrt theory [22] as

$${}_M H_C = 0.48 \frac{2K}{M_S} - N M_S, \quad (2.15)$$

where N is the demagnetizing factor, for a non interacting single domain powder assembly. In general this value can be only considered as an approximation for the coercivity, first of all since nucleation processes of domain walls and domain wall movement cannot be completely neglected in commercial hexaferrites, due to bigger grain sizes. Even if the grains are sufficiently small compared with the critical thickness, domain wall processes have to be considered because of lattice defects, stacking faults, or local changes in anisotropy and inhomogeneities of magnetic fields at the edges of the plate like crystals. A semi-empirical formula was found to describe the coercivity

[54]

$$JH_C = aH_A - \frac{N}{\mu_0}(B_r + J_S). \quad (2.16)$$

Typical values for the coercivity are shown in tab.2.7.

Table 2.7: Coercivity at room temperature of the M-type compounds, prepared by coprecipitation [5]

compound	MH_C [T]
SrFe ₁₂ O ₁₉	0.575
BaFe ₁₂ O ₁₉	0.6

2.2.3 Substituted M-type hexaferrites

It was tried to improve the M-type hexaferrite by modifying the formula XFe₁₂O₁₉ through substitution of elements. Improving a hard magnetic material means either to enhance magnetization or increase coercivity. Coercivity can be increased in two ways, modifying the microstructure or increasing the magnetocrystalline anisotropy.

There are two possibilities for substitution: substitution of the X ion or substitution of the Fe ion. If the valence is the same and the ionic radius resembles the one of the substituted element, the crystal structure will be unchanged and only a slight change in the lattice parameters will occur. It is also possible to substitute with elements with different valence, but in this case a charge compensation must take place. This can be in form of double substitution, like in the case of La-Co substituted samples, where one ion may compensate the charge of the other one. In the La-Co substituted samples, which is an example for successful substitution since anisotropy is significantly increased in these compounds, the La ion with valence 3+ substitutes for the X ion with valence 2+ and Co with valence 2+ compensates this with an additional electron at one of the Fe³⁺ sites. Another possibility of charge compensation is, that Fe changes its valence state, which occurs in the LaM compound.

Ca was used for a substitution of the X ion without changing the valence, but the pure CaM phase was reported to be not stable [55, 56]. Only with addition of La the compound was stable, but in magnetic properties almost equal to SrM and BaM. Other elements like Ag and Na, with a 1+ valence, were tried in addition to La^{3+} to compensate the valence difference, but without any improvement of magnetic properties [5]. Among the X ion substitutions, only the La substitution showed a strong effect. The pure LaM was reported to exhibit a strongly increased anisotropy at low temperatures [12], while the magnetization decreases only slightly. In this material a strong influence by the substitution was obtained since the X substitution has also an effect on the Fe sites changing the valence of one of the Fe ions to 2+. Lotgering explained the increased anisotropy with the orbital momentum of the Fe^{2+} ion, that enters a Fe site with positive anisotropy contribution. First Mössbauer studies didn't confirm the presence of the Fe^{2+} [57], but later measurements by Sauer et al. [58] supported this idea. The Curie temperature was reported to be decreased (695 K) in this compound due to the smaller unit cell dimensions [59]. However, only few publications are available about this compound and motivated by that an investigation of La and other rare earth substitutions started recently, including this work, following an early report of Deschamps et al. [11].

For substitutions of the Fe ions without valence change the elements Al, Ga and Cr have been intensively studied starting with Adelsköld 1938 [30] and Bertraut et al. 1959. They are industrially used since the anisotropy is increased without strong decrease of saturation magnetization. Other elements that followed were Mn^{3+} , Sc^{3+} , In^{3+} and Ru^{3+} . According to their ionic radii the ions prefer sites of a certain coordination type. With Mössbauer spectroscopy such a preference was investigated, and it was found, that Al^{3+} and Cr^{3+} enter first the 2a and then the 12k sites (octahedral), while Ga^{3+} prefers the 4f1 site (tetrahedral). For all these substitutions a decrease in Curie temperature was observed, since these ions are not magnetic and reduce the exchange. Placed on a Fe site with parallel magnetic moment this would also decrease magnetization, but placed on an antiparallel site, it could enhance magnetization. This was only observed in a La-Zn substitution, where La substitutes for the X ion and Zn for an antiparallel Fe

ion. Also the Fe substitution can be performed with two elements of different valence, compensating each other for electrical neutrality. Among this group are $\text{Ti}^{4+}\text{-Co}^{2+}$, $\text{Ti}^{4+}\text{-Zn}^{2+}$, $\text{Ti}^{4+}\text{-Ni}^{2+}$, $\text{Ir}^{4+}\text{-Co}^{2+}$ and others. An increase in anisotropy like for the LaM compound could not be observed in any of the Fe substituted materials. Instead anisotropy mostly decreases, changing for example to easy plane anisotropy above a certain amount of substitution. An overview of these materials can be found in [5].

Recently more important became the already mentioned $\text{La}^{3+}\text{-Co}^{2+}$ substituted Sr hexaferrite, which is a simultaneous substitution of the X ion and the Fe ion. After an early publication of Smolenski [6] the compound went more or less unnoticed until in the 1990's companies like Hitachi and TDK announced commercial interest. Since then detailed investigations of this material were started [60, 7] and a main contribution was given within studies of Carbone Lorraine [32]. According to a preference for octahedral sites the Co^{2+} ion enters the 4f2 and the 2a site. In cubic symmetry the Co ion exhibits an unquenched orbital momentum, that according to the single ion model enhances drastically magnetocrystalline anisotropy [20], which was observed for Co substituted magnetite. The same effect occurs in the La-Co substituted hexaferrite. At the 4f2 site the Co ion gives even a positive contribution to the total magnetization, and therefore improves the hard magnetic properties in both ways.

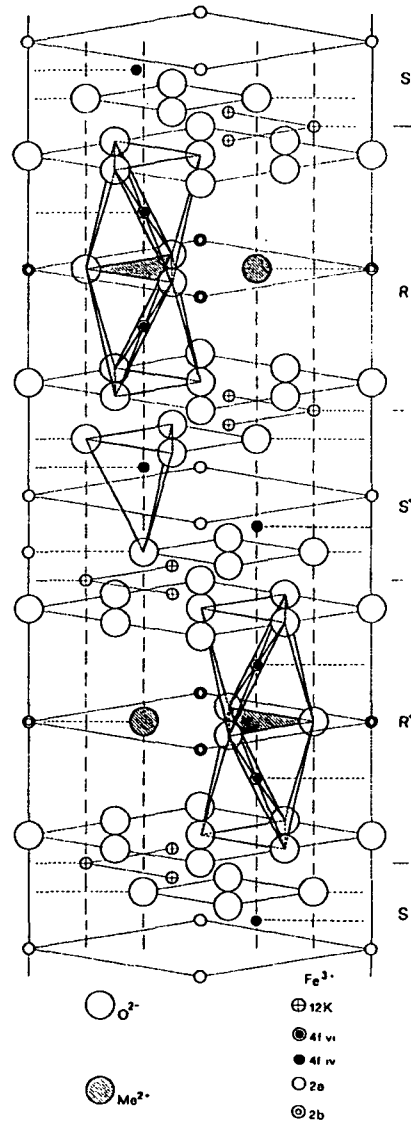


Figure 2.5: Unit cell of the magnetoplumbite crystal structure with space group $P6_3/mmc$ [37]

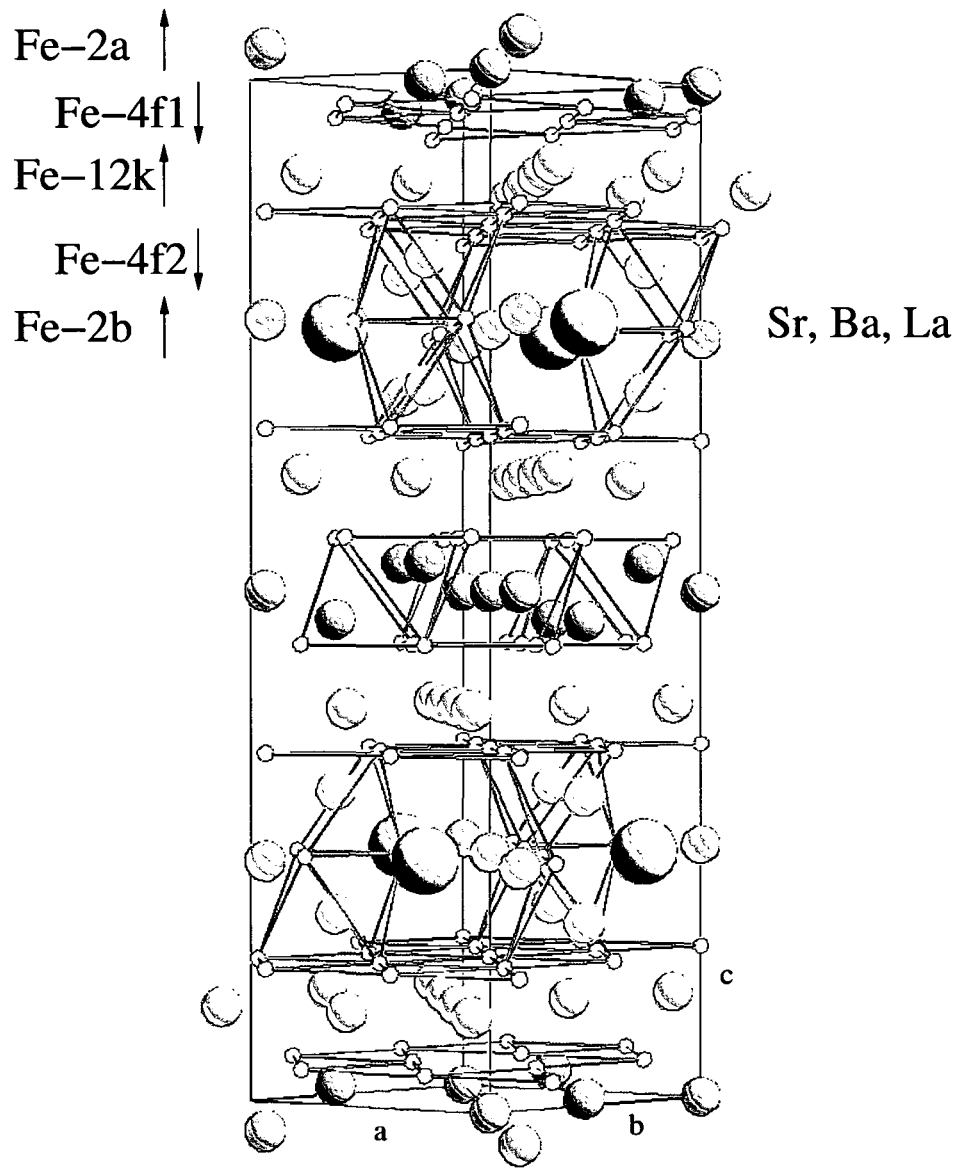


Figure 2.6: Unit cell of the magnetoplumbite crystal structure with space group $P6_3/mmc$; the directions of the Fe moments are shown

Chapter 3

Preparation and characterization techniques

3.1 Investigated compounds and preparation techniques

3.1.1 La hexaferrite and La substituted Sr hexaferrite

La substituted Sr ferrite and the pure La hexaferrite were prepared in collaboration with CIMAV, a materials research institute in Chihuahua, Mexico. The pure La hexaferrite is primarily important due to its remarkably increased magnetocrystalline anisotropy at low temperatures. Phase diagram and preparation methods for this compound were already reported [61], nevertheless there existed only few publications about this compound. The reason may be that La hexaferrite is a high temperature phase, which is metastable at room temperature. First attempts to prepare this compound failed completely. It was then found out that the main points are to perform a heat treatment within the temperature range of stability of this phase followed by a very rapid quenching.

Four different methods were tried, all typical for preparation of hexaferrites, which were mechanical alloying, a ceramic route, and 3 chemical methods, coprecipitation and two sol gel methods. For mechanical alloying [62] the starting materials were La_2O_3 and Fe_2O_3 in a ratio of 1/12. Differ-

ent amounts of La excess in mol% were used in order to compensate for Fe excess due to milling in a steel vial. The mechanical alloying was done in a hardened steel vial together with 12 mm steel balls for 24 h using a Spex 8000 mixer/mill. The ball to powder mass ratio was 8:1.

For coprecipitation the starting materials were $\text{La}(\text{NO}_3)_3$ and $\text{Fe}(\text{NO}_3)_3$ in a ratio of 1/12 with different La excess, since some La loss is expected due to different solubility of the $\text{La}(\text{OH})_3$ and the $\text{Fe}(\text{OH})_3$. These were dissolved in a solution of water and ammonia, followed by a digestion step at 80°C . Of this reaction results a fine distribution of La- and Fe-hydroxides. This powder has been carefully washed, filtered and overnight dried prior to its oxidation at 800°C for 24 h.

Two different sol gel methods were employed. For the first [63] $\text{La}(\text{NO}_3)_3 \cdot \text{H}_2\text{O}$ and ferric citrate were dissolved in distilled water. Citric acid was added to the solution in order to obtain an iron-lanthanum citrate complex. Ethylene glycol and benzoic acid were also added as secondary coordinate agents. This solution was slowly evaporated to get a gel, then the gel is overnight dried at 110°C and grounded to form a powder. The powder is subject to calcination in an open tubular furnace at 300°C for 2 h (the powder was placed in a quartz tube inside the furnace). For the second [64] $\text{La}(\text{NO}_3)_3 \cdot \text{H}_2\text{O}$ and $\text{Fe}(\text{NO}_3)_3 \cdot 9\text{H}_2\text{O}$ were dissolved in distilled water. Citric acid was added to the solution in order to obtain an iron-lanthanum citrate complex. NH_4OH was also added to adjust the pH value to about 5. This solution was slowly evaporated to get a gel. A brown-glassy material was formed and burnt in a self-propagating combustion manner until all the gel was burnt out completely to form a loose powder (ashes).

According to the phase diagram reported by Moruzzi et al. [61] the La-hexaferrite phase is only stable between 1380°C and 1420°C . So, to form this phase a heat treatment within this temperature range was performed. All samples were pressed with 3 t (1 cm^2 cross section of the samples) and heat treated in air in a tubular furnace for 23 h or 24 h using several temperatures within the stability range and some higher respectively lower temperatures. To preserve the hexaferrite phase a rapid quenching after heat treatment is necessary. Two different methods of quenching, in air and in water, were used and the resulting samples were compared with a slowly cooled sample.

Fig.3.1 shows a comparison of XRD patterns of samples prepared by all four methods and heat treated at 1385°C. To identify the various phases the samples were investigated by X-ray diffraction using Cu K α radiation at 40kV and 20mA. In agreement with Moruzzi et al. [61] the possible phases that form together with LaFe₁₂O₁₉ are LaFeO₃ (La-orthoferrite), Fe₂O₃ (hematite) and Fe₃O₄ (magnetite). For the coprecipitated sample hematite appeared as second phase, which means according to the phase diagram, that the La excess was too low. For the mechanical alloyed sample La-orthoferrite was found as second phase, due to a too high La excess. For both sol gel methods magnetite was found. This can be explained by a too high annealing temperature, because a variation of furnace temperature within $\pm 5^\circ\text{C}$ is possible. In that case the upper limit of the stability temperature range of the La-hexaferrite phase must be around 1390°C, which is much lower than reported.

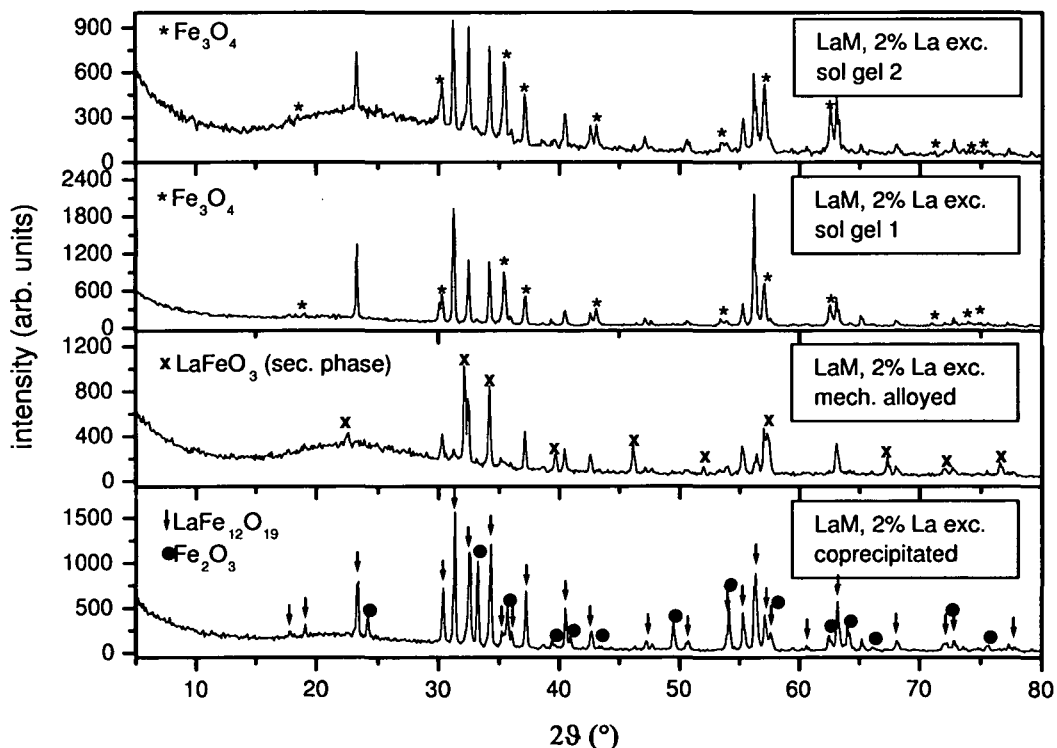


Figure 3.1: XRD measurement of samples prepared by all 4 different methods

In order to get preliminary results about the magnetic behavior, the samples were measured at room temperature in a vibrating sample magnetometer (VSM) up to 1.6 T. Fig.3.2 shows the hysteresis loops of these samples. As hematite and La-orthoferrite are antiferromagnetic, they give no contribution to the magnetization so that the loops of the coprecipitated and mechanical alloyed sample show almost no deviation and therefore contain the same amount of hexaferrite phase. $\alpha\text{-Fe}_2\text{O}_3$ exhibits a weak ferromagnetism above 260°C , where a Morin transition [65] takes place that gives a negligible contribution to the magnetization [66]. For the samples prepared by both sol gel method the contribution of the magnetite phase is clearly visible.

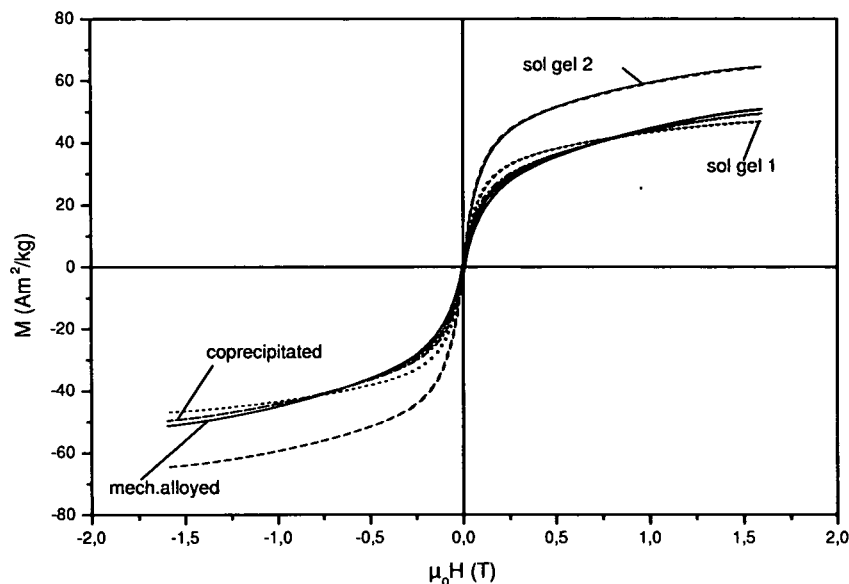


Figure 3.2: Room temperature measurement performed in a VSM of samples prepared by all 4 different methods

It was then decided to concentrate on coprecipitation and mechanical alloying, which are common in ferrite production and more simple to perform than the sol gel methods. For coprecipitation, which was mainly performed at CIMAV, the following refinements of sample preparation were performed: varying the La excess in order to reduce the secondary phases, checking the temperature range of stability with the available tubular furnace, reducing the heat treatment time and investigating different quenching methods.

The first step was to vary the La excess in order to reduce the secondary phases. Tab.3.1 shows room temperature magnetization at 1.6 T and phases of three samples with different La excess. For 10% and 100% La excess the secondary phase was hematite and La-orthoferrite respectively, which means that there was either too little or too much La added. For the 50% sample both secondary phases appeared, so that this amount of starting material should result approximately in the required 1/12 ratio for La/Fe. This is also confirmed by the magnetization value, which is highest for this sample.

Table 3.1: Samples prepared by coprecipitation with different La excess. All samples are heat treated at 1365°C for 23 h and quenched in water. Secondary phases were determined by XRD.

La exc. (%)	$M_{1.6T}$ (Am ² /kg)	secondary phases
10	52.5	Fe ₂ O ₃
50	63.1	Fe ₂ O ₃ +LaFeO ₃
100	59.2	LaFeO ₃

In order to verify the temperature range of stability of the La-hexaferrite phase a series of samples was heat treated at several temperatures starting at 1355°C in steps of 5 degrees (see tab.3.2). As expected at 1355°C almost no hexaferrite phase was found, only hematite and La-orthoferrite. But already at 1360°C a smaller amount of LaFe₁₂O₁₉ was formed. This is in disagreement with the phase diagram reported by Moruzzi et al. [61], where formation of hexaferrite phase was found at 1380°C lowest temperature. From 1360°C to 1380°C the magnetization is steadily increasing, except at 1375°C. This value has to be considered as an outlier, and may be explained by a variation in furnace temperature. Beside this value the magnetization varies only slightly between 1370°C and 1390°C, so that any temperature within this temperature range will be good for heat treatment. But above 1390°C only La-orthoferrite and magnetite were formed.

Tab.3.3 shows the comparison of samples quenched in different ways. Because of the metastability of the La-hexaferrite phase the not quenched sample decomposed during cooling down to La-orthoferrite and hematite

Table 3.2: Samples prepared by coprecipitation with 50% La excess, heat treated at different temperatures for 23 h and quenched in water. Phases were determined by XRD.

temp. (°C)	$M_{1.6T}$ (Am ² /kg)	phases
1355	1.2	Fe ₂ O ₃ +LaFeO ₃
1360	46.6	LaFe ₁₂ O ₁₉ +Fe ₂ O ₃ +LaFeO ₃
1365	61.0	LaFe ₁₂ O ₁₉ +Fe ₂ O ₃ +LaFeO ₃
1370	66.4	LaFe ₁₂ O ₁₉ +LaFeO ₃
1375	61.1	LaFe ₁₂ O ₁₉ +LaFeO ₃
1380	66.9	LaFe ₁₂ O ₁₉ +LaFeO ₃
1385	65.6	LaFe ₁₂ O ₁₉ +LaFeO ₃
1390	65.5	LaFe ₁₂ O ₁₉ +LaFeO ₃

which results in a negligible magnetization. For both different quenching methods the XRD showed the hexaferrite phase, but the magnetization of the water quenched sample was higher, which is equivalent to a higher amount of LaFe₁₂O₁₉, so that this method was chosen for further experiments.

Table 3.3: Samples prepared by coprecipitation with 50% La excess, quenched in water or air and without quenching. All samples are heat treated at 1365°C for 23 h. Phases were determined by XRD.

quenching	$M_{1.6T}$ (Am ² /kg)	phases
water	61.0	LaFe ₁₂ O ₁₉ +Fe ₂ O ₃ +LaFeO ₃
air	56.1	LaFe ₁₂ O ₁₉ +Fe ₂ O ₃ +LaFeO ₃
not quenched	0.5	Fe ₂ O ₃ +LaFeO ₃

The method of mechanical alloying, which was mainly performed at the Vienna University of Technology, was enhanced for the La ferrite in a similar way, starting with the investigation of the temperature range of stability. For this investigation a sample with high La excess was chosen, in order to avoid the formation of Fe₃O₄. Magnetite is likely to form with some Fe excess and would give a contribution to the magnetization signal. Without Fe₃O₄

it is possible to estimate the amount of hexaferrite phase from the magnetization, since the other possible phases do not contribute. For this furnace type a formation of small amounts of La hexaferrite was found at 1310°C. Although in both furnaces the setting temperature was checked using a Pt-Pt/Rh thermocouple, the difference was very big. This can be explained by slight differences between sample position and position of the thermocouple, since this is essential at high temperatures. At 1365°C Fe₃O₄ formed, leading to a high magnetization value, although a smaller amount of hexaferrite phase was present in this sample. The samples heat treated between 1325°C and 1345°C are almost equal, differing only 1% in magnetization. For further heat treatments a setting temperature of 1335°C was chosen.

Table 3.4: Samples prepared by mechanical alloying with 100% La excess, heat treated at different temperatures for 24 h and quenched in water. Phases were determined by XRD.

temp. (°C)	M _{4.9T} (Am ² /kg)	phases
1305	-	Fe ₂ O ₃ +LaFeO ₃
1310	24.7	LaFe ₁₂ O ₁₉ +LaFeO ₃
1315	16.2	LaFe ₁₂ O ₁₉ +LaFeO ₃
1325	58.0	LaFe ₁₂ O ₁₉ +LaFeO ₃
1335	58.5	LaFe ₁₂ O ₁₉ +LaFeO ₃
1345	58.5	LaFe ₁₂ O ₁₉ +LaFeO ₃
1350	53.3	LaFe ₁₂ O ₁₉ +LaFeO ₃
1355	54.3	LaFe ₁₂ O ₁₉ +LaFeO ₃
1365	54.3	LaFeO ₃ +Fe ₃ O ₄

In the next step the La excess was varied, in order to find the optimum value to compensate the Fe abrasion of the steel vial and minimize the secondary phases (see tab.3.5). The best result was obtained for the sample with 2% La excess, where no secondary phase was observed in the XRD pattern. In order to ensure, that, against expectation, an even smaller amount of La could lead to better results, a sample with 2% Fe excess was prepared. The magnetization value yielded 68.7 Am²/kg and the secondary phases were LaFeO₃ and Fe₂O₃.

Table 3.5: Samples prepared by mechanical alloying with different La excess. All samples are heat treated at 1335°C for 24 h and quenched in water. Secondary phases were determined by XRD.

La exc. (%)	$M_{4.9T}$ (Am ² /kg)	secondary phases
2	73.9	-
20	69.5	LaFeO ₃
50	65.1	LaFeO ₃
100	58.5	LaFeO ₃

With samples with 2% La excess the investigations were continued and it was tried to reduce the heat treatment duration (see tab.3.6). With decreasing heat treatment duration the magnetization, and therefore the amount of hexaferrite phase, is reduced. In the XRD pattern of the sample heat treated for 1 hour, LaFeO₃ and Fe₂O₃ were visible, which means that the reaction is not yet complete and this explains the reduction in magnetization by 7%. Between 24 h and 8.5 h almost no reduction appeared, therefore a heat treatment for more than 8 hours is sufficient.

Table 3.6: Samples prepared by mechanical alloying with 2% La excess, heat treated at 1335°C temperatures for different durations and quenched in water.

duration (h)	$M_{4.9T}$ (Am ² /kg)
24	73.9
16.5	73.3
8.5	73.5
5	70.8
2	69.4
1	68.8

Partly with La substituted Sr ferrite samples were prepared by coprecipitation as well as by mechanical alloying. These samples were interesting in order to monitor the changes in crystal structure and magnetic properties

from Sr hexaferrite to La hexaferrite. Only one sample was prepared by coprecipitation (see tab.3.7), following the same procedure as described above using in addition $\text{Sr}(\text{NO}_3)_2$ in a ratio of $\text{La}/\text{Sr}=1/2$. This sample was pressed and heat treated at various temperatures ranging from 1000°C to 1365°C , the same temperature, which was used for the pure La ferrite. Fig.3.3 shows

Table 3.7: La substituted Sr hexaferrites with nominal formula unit

name	formula unit	preparation method
LaM50	$\text{LaFe}_{12}\text{O}_{19}$	coprecipitation
LaM3	$\text{LaFe}_{12}\text{O}_{19}$	mechanical alloying
SrLa2.1co	$\text{Sr}_{0.66}\text{La}_{0.33}\text{Fe}_{12}\text{O}_{19}$	coprecipitation
SrLa8.1	$\text{Sr}_{0.88}\text{La}_{0.11}\text{Fe}_{12}\text{O}_{19}$	mechanical alloying
SrLa4.1	$\text{Sr}_{0.8}\text{La}_{0.2}\text{Fe}_{12}\text{O}_{19}$	mechanical alloying
SrLa2.1	$\text{Sr}_{0.66}\text{La}_{0.33}\text{Fe}_{12}\text{O}_{19}$	mechanical alloying
SrLa1.1	$\text{Sr}_{0.5}\text{La}_{0.5}\text{Fe}_{12}\text{O}_{19}$	mechanical alloying
SrLa1.3	$\text{Sr}_{0.25}\text{La}_{0.75}\text{Fe}_{12}\text{O}_{19}$	mechanical alloying
SrM	$\text{SrFe}_{12}\text{O}_{19}$	mechanical alloying

the hysteresis loops of these samples measured in a VSM. With increasing temperature the coercivity is decreasing from a for hexaferrites typical coercivity of 0.5 T after heat treatment at 1000°C to a negligible coercivity at 1365°C annealing temperature. But there is also a decrease in magnetization for low annealing temperature, which indicates a higher amount of secondary phases. It is expected that not the complete amount of La entered the lattice, which would also result in a lower magnetization if the La formed a compound, which does not contribute to magnetization. Most probable is the formation of La orthoferrite or La_2O_3 which is non magnetic. The XRD showed as secondary phase in this sample only Fe_2O_3 , but as the gate time for the XRD measurement was low, it is possible that an amount of a few percent of secondary phase is not visible in the pattern. As there is almost no change in lattice parameter between La hexaferrite and Sr hexaferrite because of the similar ion radii of La^{3+} (0.115 nm) and Sr^{2+} (0.113 nm), it is also not easy to distinguish between these two phases in XRD. Therefore it is more safe to perform a heat treatment at high temperatures, to ensure

that La enters the hexaferrite structure. Unfortunately the high temperature stimulates grain growth and leads therefore to a reduced coercivity. This was also confirmed by images of scanning electron microscope (see chapter 4.1.1).

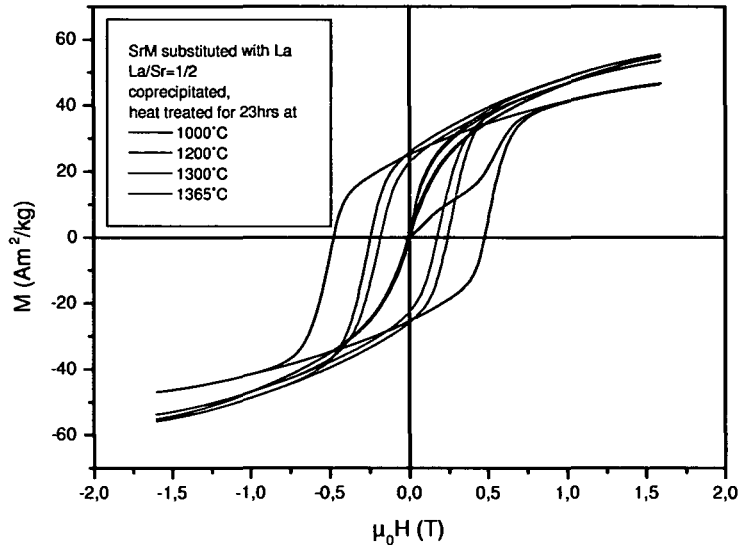


Figure 3.3: VSM measurement of the sample SrLa_{2.1}co heat treated at different temperatures

Samples with various La concentrations were prepared by mechanical alloying (see tab.3.7). While for the La ferrite the starting materials were oxides, for the partly substituted Sr ferrite carbonates were used according to the usual procedure for Sr or Ba ferrite [67]. The samples were prepared according to the formula $(1 - x)\text{SrCO}_3 + x/2\text{La}_2(\text{CO}_3)_3 + 6\text{Fe}_2\text{O}_3$, using different La concentrations x . No La excess was used for these samples. All samples were heat treated for 24 h at 1335°C and quenched in water. The pure Sr ferrite (SrM) was heat treated only for 2 h at 1000°C, which is sufficient to form this phase. Tab.3.8 shows the secondary phases in these samples, determined by XRD, and the quantitative analysis was performed by the Rietveld method [68]. All samples with concentrations higher than $x=0.2$, except $x=1$, contain an amount of hematite (Fe_2O_3). In order not to change the La/Fe ratio, also an amount of a La containing secondary phase should be present, although it was not observed in the XRD pattern. Since

the background in these patterns was very small, even an amount of only 1% is possible to be observed with a good quantitative analysis. Either the La evaporated forming a gas phase during the heat treatment, or there exists a phase with higher La/Fe ratio, that exhibits a very similar XRD pattern, like for example the W-type for the conventional hexaferrites. Such a phase is not reported yet. For future experiments it is necessary to perform a chemical analysis of the Fe and La amount in the sample, by e.g. titration.

Table 3.8: Amount of secondary phase Fe_2O_3 in partly with La substituted Sr hexaferrites, prepared by mechanical alloying

sample	x	Fe_2O_3 [%]
SrM	0	0
SrLa8.1	0.11	0
SrLa4.1	0.2	0
SrLa2.1	0.33	8
SrLa1.1	0.5	6
SrLa1.3	0.75	12
LaM3	1	0

3.1.2 Rare earth substituted Sr hexaferrite

Substituted Sr hexaferrite prepared by hydrothermal synthesis

The La, Sm and Nd substituted Sr-M particles were produced by hydrothermal synthesis [14]. The chemical precursors used for these experiments were $\text{Fe}(\text{NO}_3)_3 \cdot 9\text{H}_2\text{O}$, $\text{Sr}(\text{NO}_3)_2$, $\text{RE}(\text{NO}_3)_3 \cdot 6\text{H}_2\text{O}$ ($\text{R} = \text{Sm}, \text{Nd}, \text{La}, \text{Pr}$) and NaOH . The precursors were weighed according to different $\text{RE}^{3+}/\text{Sr}^{2+}$ ratios (n), where n was varied between 1/16 and 1/2, while $\text{Sr}^{2+}/\text{Fe}^{3+}$ and $\text{NO}_3^-/\text{OH}^-$ ratios were fixed at 1/8 and 1/2 respectively. A water solution containing Sr^{2+} , Fe^{3+} and RE^{3+} ions was poured into the solution of NaOH . Aqueous suspensions containing the precipitated products were sealed, stirred at 1000 rpm and heat-treated at 220°C in an autoclave for 3 h. The resultant particles were washed carefully, filtered and then dried

at 80°C overnight. The as-synthesized particles were calcined at 1100°C to 1150°C for 2 h in air.

Dy and Er substituted Sr hexaferrite

According to the experience with La ferrite, it was assumed that the hexaferrite structure forms also for other rare earth elements. This would be very interesting, since they have a magnetic moment in contrast to La, which may contribute to the magnetization, and can exhibit an orbital momentum, which may influence anisotropy and magnetostriction. Dy ($S=5/2$, $L=5$) and Er ($S=3/2$, $L=6$) were chosen for this experiment, also for the reason of the affordable costs.

Dy hexaferrite was tried to be prepared by mechanical alloying following the same procedure as for the La hexaferrite. Dy_2O_3 and Fe_2O_3 were used as starting materials with 2% Dy excess. A heat treatment for 2 h at temperatures ranging from 1225°C to 1400°C in steps of 25° was performed, in order to find the temperature range of stability, and the samples were again quenched in water. Unfortunately no hexaferrite phase was formed. Above 1325°C the sample exhibited a magnetization of 62 Am²/kg, and with XRD the pattern could be attributed to the $Dy_3Fe_5O_{12}$ phase [69], which has garnet structure like YIG compound. These are magneto optic compounds, exhibiting a strong anisotropy at 4.2 K.

The attempt was also not successful for Er which was prepared by coprecipitation and heat treated between 1340°C and 1380°C. This temperature range was very small, so that it is probable, that the temperature range of stability was not found. For future investigations it is recommended to try heat treatments at temperatures in a very large range (eg between 1200°C and 1500°C) and use small steps of not more than 20°. Otherwise it may happen, that one misses the stability range, since it can be very small, like in LaM and it may be significantly shifted to higher or lower temperatures.

3.2 Characterization techniques

3.2.1 X-ray diffraction

X-ray diffraction uses on the constructive and destructive interference of X-rays reflected at the crystal lattice planes. It is based on the Bragg equation

$$2d\sin\theta = n\lambda$$

delivering for a certain wavelength λ the lattice plane distance d at a certain reflection angle θ . Scanning all angles delivers a diffractogram with peaks corresponding to the different lattice planes in the crystal structure. This reflects the crystal symmetry and is characteristic for a material.

X-ray diffraction was performed at a Siemens D500 powder diffractometer with a graphite monochromator. Co $K\alpha$ radiation ($\lambda=1.79 \text{ \AA}$) at 35mA and 30kV was used. For low temperature diffraction a helium flow temperature controller down to 4.2 K was available. The system was controlled by a LINUX based software, developed at the Department of Solid State Physics (TU Vienna). The evaluation of the data was performed with the software Topas by Bruker. Topas is a graphics based profile analysis program, integrating various types of X-ray and neutron diffraction analyses by supporting all profile fit methods currently employed in powder diffractometry. For quantitative analysis the Rietveld method [68] was employed.

3.2.2 Neutron diffraction

Neutron diffraction is based on the same principles as X-ray diffraction. The wavelength of the neutron is adjusted by their velocity using

$$p = mv = \hbar k = \hbar \frac{2\pi}{\lambda}.$$

Neutrons have the advantage that due to their magnetic moment, they interact with magnetic materials, so that information about the local magnetic moments in the sample can be obtained.

The neutron diffraction experiments were performed at the Institute Laue

Langevin, Grenoble, France, in collaboration with Dr. C. Ritter. The diffractometers D20 and D2B, for high resolution experiments, were employed. D20 is very high intensity 2-axis diffractometer equipped with a large He³ microstrip gas detector. Due to the high neutron flux, small samples can be measured. The complete diffraction pattern, covering a scattering range of 153.6°, can be obtained as a function of temperature, pressure or other parameter. D2B is very high-resolution powder diffractometer designed to achieve the ultimate resolution. Being on a beam tube in the reactor hall, it can use wavelengths as short as 1.05 Å and can collect the complete diffraction patterns in 15-60 minutes, depending on the amount of sample.

3.2.3 Microscopy

In order to determine microstructure the samples were examined with a scanning electron microscope (SEM) and an optical microscope. A JEOL T 330A SEM was available at the Departement of Solid State Physics, TU Vienna. Since hexaferrites are insulators a thin layer (30 Å) of Au-Pd was sputtered on the surface of the samples to make an electrical contact with the anode. For element analysis an EDAX UTW detector was used, performing energy dispersive spectroscopy (EDS), where characteristic X-rays emitted from the sample are measured. A Polyvar optical microscope was used for determining the grain size.

3.2.4 Density

For density measurements a Micromeritics multivolume pycnometer 1305 was used. This is a He gas pycnometer, observing the reduction of gas capacity in the sample chamber caused by the presence of the sample. Since helium penetrates even the smallest pores and surface irregularities, the volume obtained permits computation of the theoretical density. The gas capacity is measured by the pressure in the sample chamber and after expansion of the gas in a second precisely known volume.

3.2.5 Resistivity measurement

Theory

The resistivity of hexaferrites exhibit a semiconductor like behavior following an exponential law for the temperature dependence

$$\rho = \rho_{\infty} e^{\frac{E_{\rho}}{k_B T}}.$$

The activation energy E_{ρ} for eg. $\text{BaFe}_{12}\text{O}_{19}$ is 0.8 eV [43]. This corresponds to 9280 K, so at room temperature hexaferrites are good insulators with a specific resistivity of $10^6 \Omega\text{m}$. In the La substituted SrM the La may act as p-doping and the gap energy is significantly reduced, so that there is a considerable conductivity at room temperature. The simple exponential behavior dominates at higher temperatures. At low temperature in the La substituted samples a variable-range hopping [70] mechanism takes over. This means a conduction via hopping of electrons between localized states close to the Fermi level. This type of conduction always occurs if temperature is sufficiently low or if the medium is disordered, e.g. due to impurities. In this case the resistivity follows a law

$$\rho = A e^{\frac{B}{k_B T^{1/4}}}. \quad (3.1)$$

More general one can write

$$\rho = A e^{\frac{B}{k_B T^{\nu}}},$$

where $1/4 \leq \nu \leq 1/2$, since ν was found to differ from 1/4 for e.g. a non constant density of states close to the Fermi level [71].

Experimental setup

The resistivity was measured with a Linear research LR-700 DC resistance bridge in zero field. The samples, cylindrical pellets of pressed and annealed powder, were contacted with conductive silver paste, a copper foil and thin copper wires. To fix everything, it was wrapped in teflon tape and fixed with a small copper clamp (see fig.3.4). The measurement was performed in a He dewar vessel in order to vary the temperature from room temperature down

to 4.2 K.

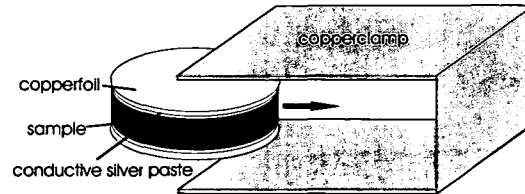


Figure 3.4: Sketch of the sample contact to perform the resistivity measurement

3.2.6 Calorimetry

For measurements of the specific heat the quasi-adiabatic pulse heat method was used. In this method the sample is exposed to a certain amount of heat, given in form of a pulse, ΔQ and the change in temperature ΔT is measured. If the sample is in ideal adiabatic condition the specific heat is given by

$$C(T) = \lim_{\Delta T \rightarrow 0} \frac{\Delta Q}{\Delta T}.$$

In a realistic measurement one has to consider three types of errors: internal relaxation of the sample, external relaxation or heat loss and self heating of the thermometer. The internal relaxation is due to the expansion of the sample, so that it takes some time until the heat gradient within the sample vanishes. The external relaxation is due to heat exchange with the environment, which results in a heat loss of the sample.

For realizing adiabatic conditions in the experimental setup, the sample is mounted on a small sapphire disk, which is connected with the sample holder only through thin nylon wires. The heating is performed with a strain gauge, connected through very thin manganin wires of diameter of 76 μm . The temperature is measured with a field calibrated CERNOX-resistivity thermometer with wire connections of 20 μm . All wires are fixed at the irradiation shield (gold plated copper tin), surrounding the sample. It is temperature controlled by a Lake Shore DRC-93CA, using a carbon-glass thermometer. The sample holder is inserted in a magnet for field dependent

measurements. Temperature dependent measurements are performed in a He flow cryostat.

3.2.7 Pulsed field magnetometer

Theory

A pulsed field magnetometer is used for measurements of the hysteresis loop of hard magnetic materials and anisotropy. The measurement is based on the law of induction

$$U = -\frac{d\Phi}{dt},$$

so that a time varying magnetic flux is necessary. This is performed by a time varying magnetic field, for example a field that is produced by a magnet supplied with a sinusoidal alternating current. If a magnetic sample is placed in such a field, its magnetization will follow the time dependence of the field and therefore induce a voltage in a small coil wound around the sample. The detection of the signal is usually not performed with a single coil, but with a set of 4 coils, two that measure the magnetization and compensate for the signal of the external field and two that measure the external field in symmetric arrangement with respect to the magnet homogeneity. Such a set is called pick-up system. The signal is proportional to the time derivative of the magnetization according to $U = -\frac{d}{dt} \int \vec{B} d\vec{A} = -\frac{d}{dt} \mu_0 (H + M) A$, so that it has to be processed afterwards. For hysteresis measurements the signal is integrated, while for anisotropy it is derivated.

The latter is based on the singular point detection method (SPD) [72]. It is known that in a single crystal the magnetization curve in the hard direction, shows a singularity in the second derivative $\frac{d^2 M}{dH^2}$ at the anisotropy field H_A , since $M(H)$ is linear for $0 < H < H_A$ and constant for $H > H_A$. In a polycrystalline material the curve is more smooth, but still it keeps information about the anisotropy field, since there is always a part of crystallites oriented in the hard direction. For a uniaxial material one can find a peak in the second derivative of $M(H)$. For basal plane anisotropy or cubic anisotropy the peak occurs in higher order derivatives, but then it is very difficult to measure since the derivation of the signal produces a lot of

noise and then the peak is not visible.

The SPD technique can be easily performed in a pulsed field magnetometer, since the signal detected is already the first derivative with respect to time. If the functions $M(t)$ and $H(t)$ are steady and invertible, the second derivative with respect to time can be converted to $\frac{d^2M}{dH^2}$. So it is just necessary to differentiate the measured signal with an analog differentiator.

Experimental setup

The pulsed field magnetometer used for the measurements was available at the Department of Solid State Physics at the Vienna University of Technology. It consists of a magnet for fields up to 30 T, a He flux cryostat for low temperature measurements, two condenser battery banks with 24 mF if both are used or 8 mF if the smaller one is used alone, the electronic control system, a transient recorder for recording the measured signal and a PC for the data acquisition. The condenser is charged by the electronic equipment and discharged over the magnet, which produces a damped sinusoidal magnetic field. The signal of the sample is detected with a coaxial pick-up system and integrated digitally with the software. The derivation is performed analog with a differentiator. The calibration of the system was performed with a magnetite sample for the magnetization signal and for the field signal with a planar coil with by NMR calibrated winding area ($N \cdot A$).

3.2.8 Vibrating Sample Magnetometer

A vibrating sample magnetometer (VSM) is based on the law of induction, too. In contrast to the pulsed field magnetometer, the external magnetic field is static, but the sample moved vertically in a low frequency sinusoidal oscillation. This induces a signal in a pick-up coil proportional to the magnetization of the sample. The main advantage is that the signal can be measured by a lock-in amplifier. The lock-in couples the induction signal with a signal synchronous with the sample oscillation and amplifies phase sensitive at the relevant frequency only. This method reduces noise significantly.

At the Department of Solid State Physics, TU Vienna, two VSM are available, one with a superconducting magnet up to 7 T and one up to 17 T.

The oscillation is generated by a loudspeaker system with a frequency of 82 Hz and amplitude of 0.1 mm and 36.44 Hz and 1.4 mm, respectively. The system with the 17 T magnet has the possibility to measure magnetization in three orthogonal direction, since it contains a special type of pick-up-system. For low temperature measurements both systems include a He flow cryostat with a heater and a temperature controller.

3.2.9 Susceptometer

Theory

With a susceptometer the susceptibility of magnetic samples is measured. It is defined by a tensor of second rank

$$\chi_{ij} = \frac{1}{\mu_0} \frac{1}{V} \frac{\partial M_i}{\partial H_j},$$

which can be considered as a response function of a magnetic material. It is usually measured in a ac magnetic field of small amplitude $H_{ac} = H_0 \cos(\omega t)$. The magnetization of the sample is measured with a pick-up system consisting of two coils, similar like in pulsed field magnetometer, but by using a lock-in amplifier. Therefore one can easily measure a signal in phase with the external field and a signal 90° phase shifted defined by

$$M_{ac} = M_0 \cos(\omega t - \phi) = M_0 \cos(\omega t) \cos \phi + M_0 \sin(\omega t) \sin \phi.$$

The susceptibility can then be given in a complex form

$$\chi = \chi' - i\chi'',$$

where $\chi' = \frac{M_0}{H_0} \cos \phi$ is the real part and $\chi'' = \frac{M_0}{H_0} \sin \phi$ is the imaginary part.

Experimental setup

For the experiments a Lake Shore ac-susceptometer 7000 was used. It contains a field generating coil, wound around the pick-up-system, a stepper motor for positioning the sample, a lock-in amplifier and a PC as control

unit. Sapphire is used as pick-up tube to ensure good thermal contact without generating a magnetic moment. A He flow cryostat, a heater and a temperature controller are used for temperature dependent measurements.

3.2.10 Mössbauer spectroscopy

Theory

Mössbauer spectroscopy is based on recoilless resonance absorption of γ -rays in crystals, discovered by Mössbauer in the late 1950's (Mössbauer effect). This is possible since the crystal transforms the recoil energy in phonon energy distributed over the whole crystal, which has a naturally high mass. A common γ -ray source is the radioactive ^{57}Co , that decays through electron capture in an excited state of ^{57}Fe . The transition of ^{57}Fe from the $3/2$ to the $1/2$ state (14.4 keV) is then used in the Mössbauer experiment. This radiation excites the ^{57}Fe in the sample, which is around 2% of the total Fe amount, and the following transmitted radiation is detected. Due to the Zeeman splitting in a magnetic material six different transitions from the excited $3/2$ state to the $1/2$ groundstate are allowed with $\Delta m = 0, \pm 1$ (see fig.3.5) and therefore a sextet is observed. This splitting is sensitive to interactions between the nuclear magnetic moment with surrounding electric and magnetic fields.

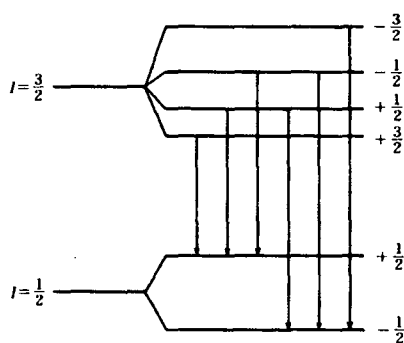


Figure 3.5: Transitions from the excited $3/2$ state of ^{57}Fe to the $1/2$ ground state

The main factors that can be determined by Mössbauer spectroscopy

are the hyperfine field, due to the nuclear-Zeeman splitting caused by the magnetic hyperfine field (see chapter 2.1.2), the isomer shift, due to the electrical potential caused by a charge density at the nuclear site, and the quadrupole shift, caused by the interaction between the nuclear quadrupole moment and an electrical field gradient. The two latter terms arise from the electrostatic exchange energy of a charge distribution with an electrical field

$$E_{el} = q\Phi - \vec{p}\vec{E} - \frac{1}{6}Q_{ij}\frac{\partial E_i}{\partial r_j} + \dots \quad (3.2)$$

Because of parity the nucleus has no dipole moment, therefore the second term in 3.2 vanishes. The first term corresponds to the isomer shift, the third to the quadrupole shift.

An electrical potential at the nucleus site arises mainly from s electrons. If s electrons give a contribution to chemical bondings or change their distribution due to interaction with outer shells (e.g. 3d electrons), this can be determined by the isomer shift. It has to be mentioned that only the difference between the electron density of the source and of the absorber is measured. It is therefore necessary to define the matrix of the ^{57}Fe source. The energy shift also depends on the change in radius of the excited nucleus and the groundstate. The isomer shift is visible in a shift of the whole sextet by a constant factor.

A non negligible electrical field gradient (EFG) is present only for sites with non cubic symmetry. Octahedral and tetrahedral sites have usually very small field gradients, since they are close to cubic symmetry. Nuclei with $I = 0$ and $I = 1/2$ have a zero quadrupole moment, thus only the excited state of ^{57}Fe is influenced. This leads to a shift of the outer lines in the sextet to higher energies, while all other lines are shifted to lower energies, depending on the sign of the EFG.

The intensity of the Mössbauer line can be calculated from a harmonic oscillation considering the Debye model (see chapter 2.1.5). This leads to the Lamb-Mössbauer factor

$$f = e^{-\frac{E_R}{\hbar\omega}} = e^{-k_0^2\langle x^2 \rangle},$$

where E_R is the recoil energy and $\langle x^2 \rangle$ is the mean squared displacement of the oscillator. For the Bragg reflection of x-rays this is equal to the Debye-Waller factor. The intensity of the different Fe sublattice spectra in different materials depends therefore on the bonding. For all ferrites an identical Lamb-Mössbauer factor was assumed for all sublattices, so that the area of the spectra is proportional to the weight percentage.

Experimental setup

The Mössbauer spectrometers at the department of Solid State Physics at the Vienna University of Technology are using a ^{57}Co source in Rh matrix, which has a half-life of 270 days. The Fe line used has an energy of 14.4 keV. A variation of this energy is performed by a movement of the source with constant acceleration. This changes the energy according to the Doppler effect by $\Delta E = \pm \frac{v}{c} E_0$. With a velocity of 1 mm/s a Doppler shift of 48 neV is produced, which is 10 times the natural line width (life time of the excited ^{57}Fe state $\tau = 1.4 \cdot 10^{-7}$ s). As absorber thin layers of powder samples were used, to ensure transmission of the low energy γ -rays. For low temperature measurements a He flow cryostat with temperature controller was used, while for high temperature a furnace with temperatures up to 800°C and a PID regulator was available. As detector a gas proportional counter with 97% Kr and 3% CO_2 as quenching gas with a voltage of 2.7 kV was used. The transmitted γ -ray intensity shows a minimum at the energies, where absorption occurs. The pulses of the detector are amplified and in a multi channel analyzer counted with respect to a velocity interval.

3.2.11 Nuclear magnetic resonance

Theory

Nuclear magnetic resonance is a method to measure energy transitions of the nucleus in a magnetic field. The $2I + 1$ degenerate energy of the nuclear magnetic moment splits in a magnetic field B_0 into the equidistant energy levels

$$E = -m\gamma B_0 \hbar, \quad -I \leq m \leq I,$$

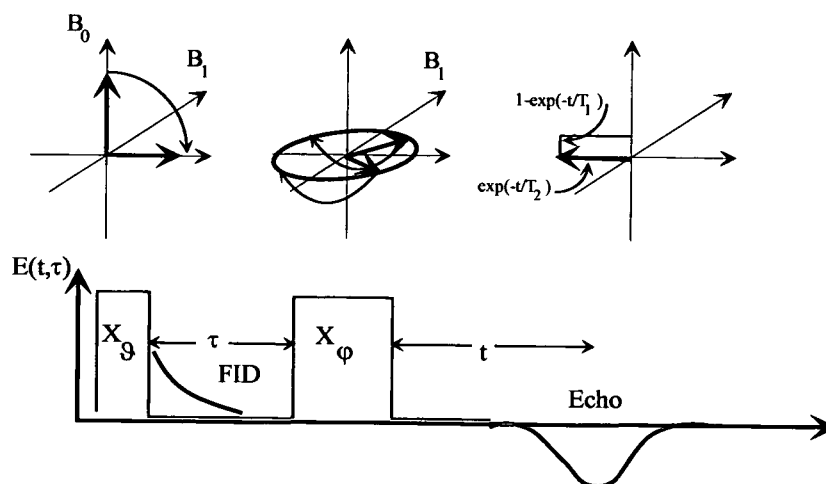
where $\gamma = g_N$, the gyromagnetic ratio of the nucleus, as defined in chapter 2.1.1. Dipole transitions $\Delta m = \pm 1$ can be induced by irradiation of the energy $E = \hbar\omega = \hbar\gamma B_0$. This is usually performed with an alternating magnetic field. The transition can be described classically by a change of precessional motion of the magnetic moment with the frequency $\omega_L = \gamma B_0$, the Larmor frequency. Taking into account a system of nuclear spins leading to a nuclear magnetization M and energy exchange between the spins and between the spin and the lattice, this leads to the Bloch equations

$$\frac{d\vec{M}}{dt} = \gamma\vec{M} \times \vec{B}_0 - \frac{M_x\hat{x} + M_y\hat{y}}{T_2} + \frac{M_0 - M_z}{T_1}\hat{z}$$

where T_1 is a characteristic time for the relaxation of the longitudinal magnetization to the thermal equilibrium value M_0 (spin-lattice relaxation) and T_2 is the relaxation time for the spin-spin-relaxation that describes the loss of phase coherence between the spins.

In ferromagnetic materials the field B_0 is given by four different terms, the external field, the demagnetizing field, the Lorentz field (see chapter 2.1.3) and the hyperfine field, which is the field at the nucleus position produced by the surrounding electrons. Assuming spherical particles, Lorentz field and demagnetizing field cancel each other and the hyperfine field can be measured directly. An external field is only necessary to determine the orientation of the hyperfine field. The hyperfine field provides information about the local magnetization of the sample, since they are coupled through the hyperfine coupling constants (see chapter 2.1.2). The local surrounding also influences the hyperfine field, so that different crystal sites can be distinguished. In a magnetic sample the magnetization leads to an amplification of the alternating field, due to the tilting of the magnetization vector in the direction of the alternating field. Since too high intensities lead to equally occupied energy levels, no signal can be observed, because the difference in occupation according to the Boltzmann factor is essential for the resonance. Therefore it is necessary to reduce the amplitude. In magnetic walls the field is even more amplified than in domains. By choosing the right intensity for the alternating magnetic field signals either from domains or from walls can be observed.

A powerful method to observe the resonance signal is the spin-echo method (see fig.3.6). This can be explained using the classical interpretation with a rotating coordinate system with z-axis in the direction of the static field B_0 and the rotation frequency equal to the frequency of the alternating field B_1 . In this coordinate system the alternating field is also static in x-direction, and causes a precession of the magnetization vector in the y-z plane. The angle can be determined by the duration of a B_1 pulse, $\alpha = \omega \cdot t = \gamma B_1 t$. If one chooses t so that $\alpha = 90^\circ$, the magnetization will turn to the y-axis and then it will precess in the x-y plane around B_0 . Due to inhomogeneities in the field the spins will have slightly different Larmor frequency and spread over the x-y plane and the signal weakens rapidly. If now another pulse is applied, so that $\alpha = 180^\circ$, the spins are again in the x-y plane, but the ones that are slower are now closer to the -y-axis than the ones that are faster, so that all will refocus after a time $t = 2\tau$, with τ the time between the two pulses. The signal observable at that time is called the echo.



habkoll.ds4:echoerz.eps

Figure 3.6: Scheme of the spin-echo method

Experimental setup

The experimental setup includes a superconducting magnet with maximum field of 7 T, that produces the external field B_0 . Most spectra of the hexaferrites were measured in zero field using a frequency sweep. For the ^{57}Fe

($I = 1/2$) resonance a field was used to identify spin up and spin down sites. The ^{139}La ($I = 7/2$) resonance was measured in a field sweep. A He flux cryostat with temperature controller was used for temperature dependent measurements, measurements at 4.2 K were performed in a liquid He dewar vessel. The NMR system consists of sample holder, the transmitter electronic equipment and the receiver electronic equipment. The sample holder contains the resonance circuit (parallel) with variable capacitance, that applies the high frequency pulse (MHz). The coil of this circuit also detects the signal of the sample by the induced voltage (μV). The high frequency is produced by a synthesizer and is pulsed by a PC. The pulses are delivered through an attenuator (0-63dB) and a pulse amplifier (0-45dB) to the sample holder. Pulses of frequencies between 10MHz and 1GHz can be delivered. The samples induces a signal of app. $1\mu\text{V}$ amplitude and several μs pulse duration at the resonance frequency in the coil. The frequency for Fe in the hexaferrite is around 70 MHz (2b site 60 MHz), for La between 10 MHz and 40 MHz, depending on the external field. The signal is amplified and phase sensitive detected by mixing with the synthesizer signal in phase and 90° shifted. The whole system is controlled by a PC, where also the data acquisition, including Fourier analysis of the measured signal, is performed.

Chapter 4

Experimental results and discussion

4.1 La hexaferrite

The following table gives an overview of samples investigated within this group.

Table 4.1: La substituted Sr hexaferrites with formula unit and preparation technique

name	formula unit	preparation method
LaM50	$\text{LaFe}_{12}\text{O}_{19}$	coprecipitation
LaM3	$\text{LaFe}_{12}\text{O}_{19}$	mechanical alloying

4.1.1 Structural properties

X-ray diffraction

The formation of the M-type hexagonal crystal structure was confirmed by X-ray diffraction. Fig.4.1 shows the diffractogram of the purest sample prepared by mechanical alloying (LaM3). A Rietveld analysis showed that there are no secondary phases present. The crystal parameters are given by $a = b =$

5.8907 Å and $c = 22.9003$ Å. Compared with typical values for Sr hexaferrite ($a = b = 5.883$ Å and $c = 23.037$ Å [36]) the parameter a/b are slightly increased while c is reduced.

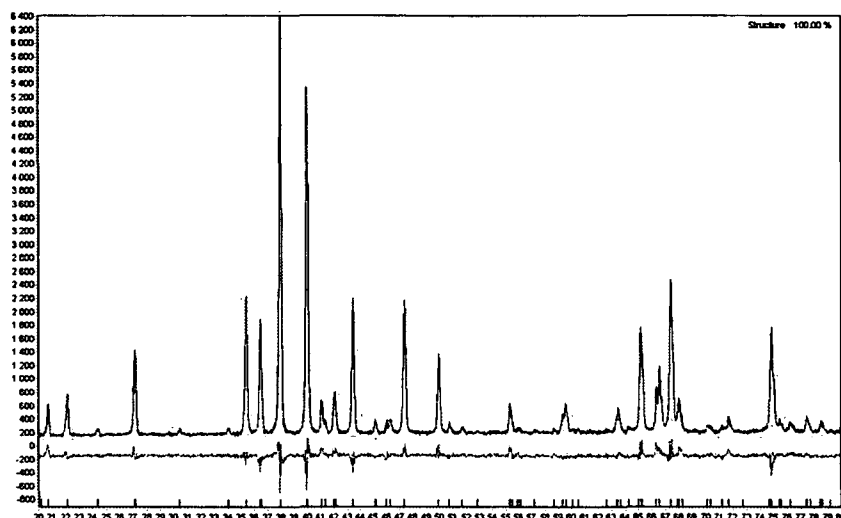


Figure 4.1: XRD of sample LaM3 analysed by Topas shows the typical M-type structure; no secondary phases were observed; the black line is the difference between measured and refined pattern

A careful comparison between the X-ray diffractograms at room temperature and at 4.2 K revealed a distortion of the hexagonal crystal lattice to an orthorhombic structure with spacegroup $CmCm$. The distortion was evident in the splitting of the peak $hkl = 220$ in the $P6_3/mmc$ structure ($2\theta = 74.83^\circ$ for Co $K\alpha$ radiation) in two peaks corresponding to $hkl = 400$ and $hkl = 260$ at 4.2 K (see fig.4.2). This splitting was also found for the peak of lower order, $hkl = 110$ ($2\theta = 35.37^\circ$ for Co $K\alpha$ radiation), although here the peak shows only a shoulder at the left, since the resolution is worse at smaller angles (see fig.4.3). Due to the splitting a distortion in the basis plane of the hexagonal structure was assumed. Fig.4.4 shows a sketch of the distortion, where an orthorhombic description with parameters a and b is used. The 400 peak was shifted to lower angles, which corresponds to an increased lattice plane distance and the parameter a' is elongated, while the 260 peak is shifted to higher angles, so that b' must be shortened. A Rietveld analysis confirmed this idea, delivering the following values for the lattice parameters

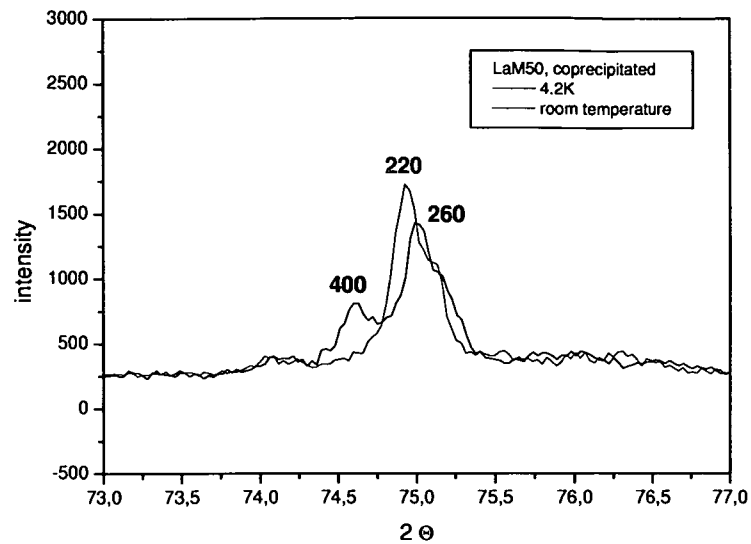


Figure 4.2: Splitting of the 220 peak of the sample LaM50 at 4.2 K; the splitting is characteristic for a distortion to an orthorhombic structure

(see tab.4.2). To compare the values b it is necessary to multiply b in the orthorhombic description with $1/\sqrt{3}$ which delivers 5.8671 \AA , which is indeed 0.4% smaller. From the line shift a distortion of $\Delta d/d=1\%$ was calculated. Also the value for c is smaller in the distorted lattice. The 6-fold symmetry

Table 4.2: Lattice parameters of LaM50 from XRD at room temperature and at 4.2 K analyzed by Topas

temperature	a [10^{-10}m]	b [10^{-10}m]	c [10^{-10}m]
300 K	5.8886	5.8886	22.8992
4.2 K	5.9044	10.1622	22.7976

of the 220 planes is broken in a 2-fold symmetry for the 400 planes and a 4-fold symmetry for the 260 planes. The intensity ratio of the peaks in the x-ray pattern corresponds usually to the symmetry and indeed the 260 peak exhibits an intensity approximately two times as high as for the 400 peak (see fig.4.2). The distorted lattice has a doubled unit cell (see. fig.4.5) and the five Fe sites change in the Wyckoff notation from 2b, 2a, 4f1, 4f2, 12k to

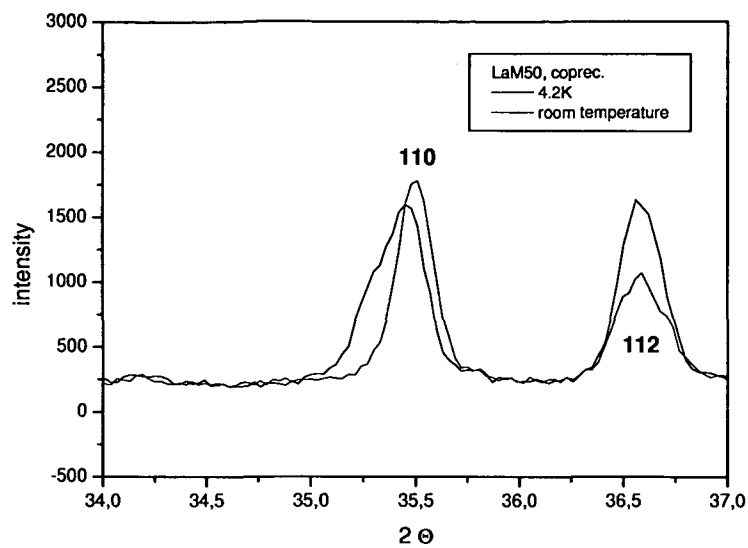


Figure 4.3: Splitting of the 110 peak of the sample LaM50 at 4.2 K; at small angles only a shoulder appears

4c, 4a, 8f1, 8f2, 8f3 and 16h, so that 12k is split in two sites. The assignment of the sites in the different spacegroups is not trivial and was observed with NMR measurements (see chapter 4.1.4).

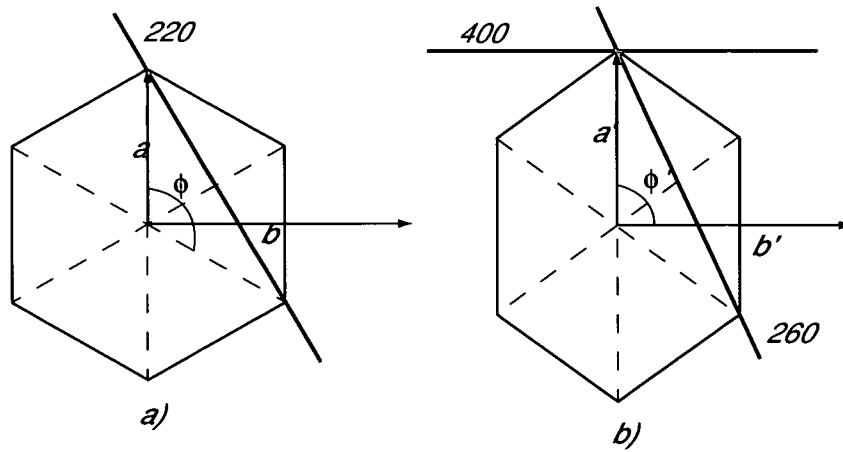


Figure 4.4: Distortion in the basis plane; a) undistorted hexagonal lattice in hexagonal discription with parameters a and $\phi = 120^\circ$ and in orthorhombic discription with $a' = a$, $b' = \sqrt{3}a$ and $\phi' = 90^\circ$; b) distorted lattice, only orthorhombic discription is possible with parameters a' , b' and $\phi' = 90^\circ$; one representative of the lattice planes corresponding to the peaks in the X-ray diffractogram are shown

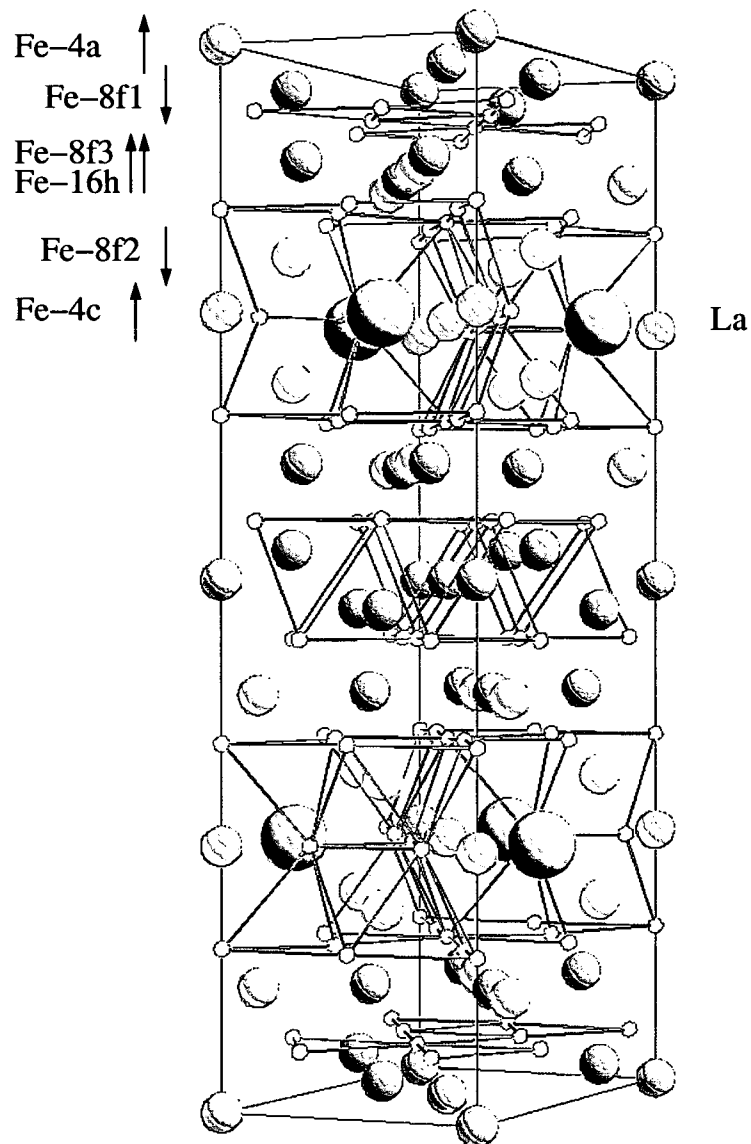


Figure 4.5: Distorted crystal lattice of the La ferrite with orthorhombic $CmCm$ spacegroup. The 12k site splits in the 16h and the 8f3 site (ions colored pink)

Neutron diffraction

With neutron diffraction of wave length 1.88 Å a temperature scan from 295 K down to 10 K was performed in order to observe the phase transition. A splitting of the peaks at 120.1° and 121.2° is shown in fig.4.6, that occurs at temperatures lower than 101 K. This is in agreement with observations of magnetic and thermal properties (see later in this chapter). The lattice parameters obtained from this measurement at room temperature and at 10 K are shown in tab.4.3. A calculation of temperature dependent lattice parameters and thermal expansion requires a detailed study of all neutron diffraction patterns, since for a good Rietveld fit the structure has to be changed from hexagonal to orthorhombic, with a possible mixing at the temperature of phase transition. This work is currently in progress.

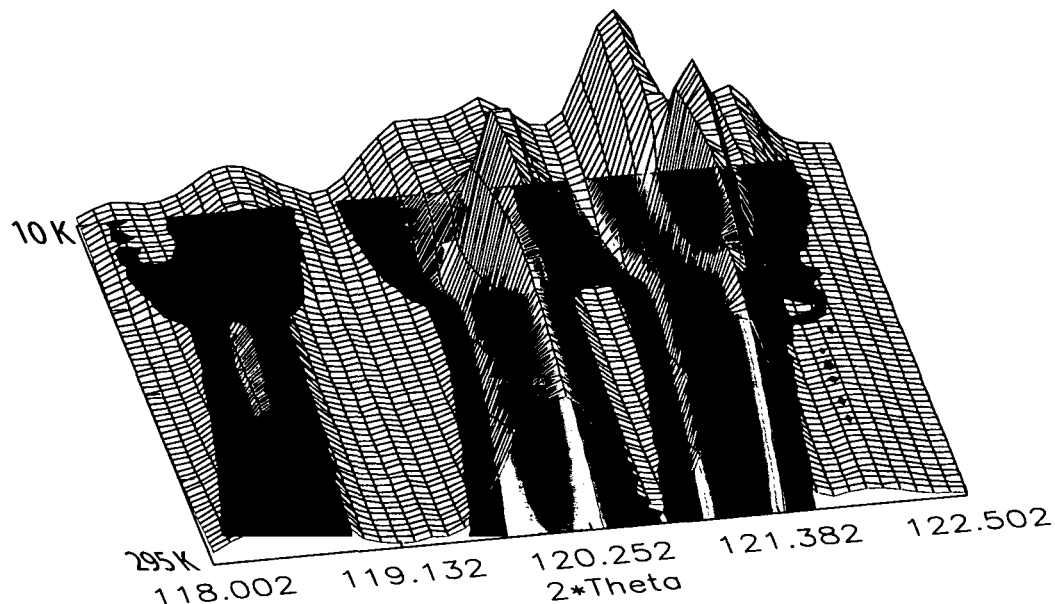


Figure 4.6: Splitting of peaks in the neutron diffractogram of LaM at low temperature indicating a phase transition

Microstructure

For studying the microstructure the sample LaM50 was investigated in a scanning electron microscope as well as in an optical microscope. Due to

Table 4.3: Lattice parameters of LaM50 from neutron diffraction at room temperature and at 10 K

temperature	a [10^{-10}m]	b [10^{-10}m]	c [10^{-10}m]
295 K	5.8858	5.8858	22.8887
10 K	5.9034	10.1626	22.7863

the porosity of the sample it was difficult to analyze the grain size. Fig.4.7 shows a SEM image with magnification factor 500 of the fracture surface. It is impossible to observe the grains, also because of the big grain size in this sample. On the polished surface no grain boundaries were visible, maybe be-

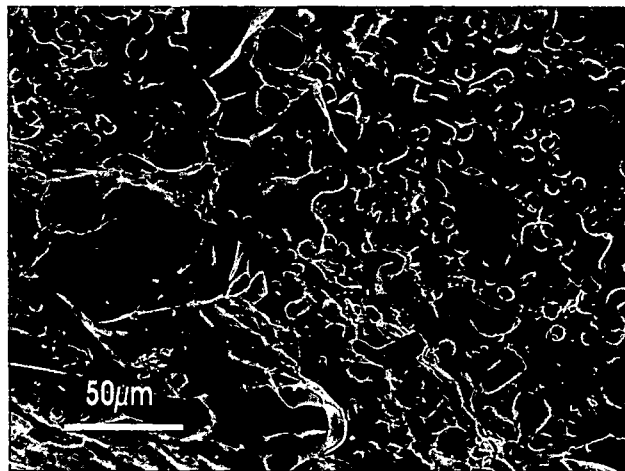


Figure 4.7: Image of SEM with magnification 500 of the LaM50 sample with fracture surface; the sample shows a strong porosity

cause polishing leads easily to a covering of the boundaries with the sample dust. Also etching methods with 10% nital, which is usually used for ferrites, and even strong acids as eg aqua regia for up to 30 sec did not improve the result. Finally the best results were obtained with the pressed, not polished, surface of the sample in an optical microscope using a magnification of 160 (see fig.4.8 and 4.9). The observed grain size is app. 100 μm . With backscattered electrons it was possible to observe the secondary phases in the sample



Figure 4.8: Image of an optical microscope with magnification 160 of the LaM50 sample; grains with diameter of around $100\mu\text{m}$ are visible

as regions of brighter color (see fig.4.10). That the darker color corresponds to the hexaferrite phase, was confirmed by an element analysis with the energy dispersive X-ray method. Compared with conventional hexaferrites the grainsize of the La ferrite is very big indicating that the grains grow very fast during the heat treatment at very high temperatures, which are necessary for formation of the hexaferrite phase. To check this a Ba ferrite was prepared by coprecipitation and heat treated at 1000°C for 2 h (sample BaM1), as is the common method, and at 1380°C for 24 h (sample BaM2), as used for preparing the La ferrite. BaM1 showed the typical platelet structure with grains in the size of a few μm , while BaM2 exhibited very big grains of more than $50\mu\text{m}$ (see fig.4.11). The hysteresis loop of sample BaM2 exhibited also a very small coercivity (see fig.4.12), while BaM1 showed a typical coercivity of 0.3 T.



Figure 4.9: Another image of the optical microscope with magnification 160 of the LaM50 sample

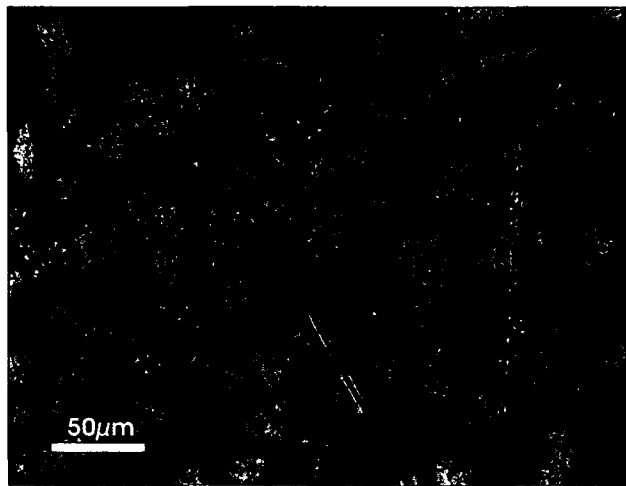


Figure 4.10: SEM image with backscattered electrons and magnification 350 of the LaM50 sample; the secondary phases Fe_2O_3 and LaFeO_3 are visible as regions of brighter color

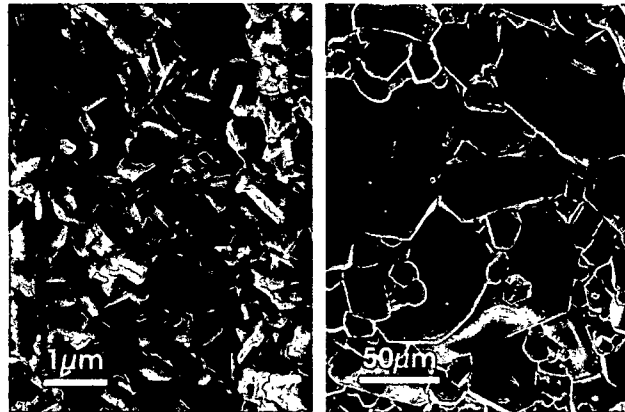


Figure 4.11: SEM image of a Ba ferrite sample prepared by coprecipitation with different heat treatment temperature (BaM1 1000° for 2 hours and BaM2 1380°C for 24 hours); sample BaM1 on the left shows grains with diameter of a few μm , while sample BaM2 on the right shows grains with diameter of more than 50 μm

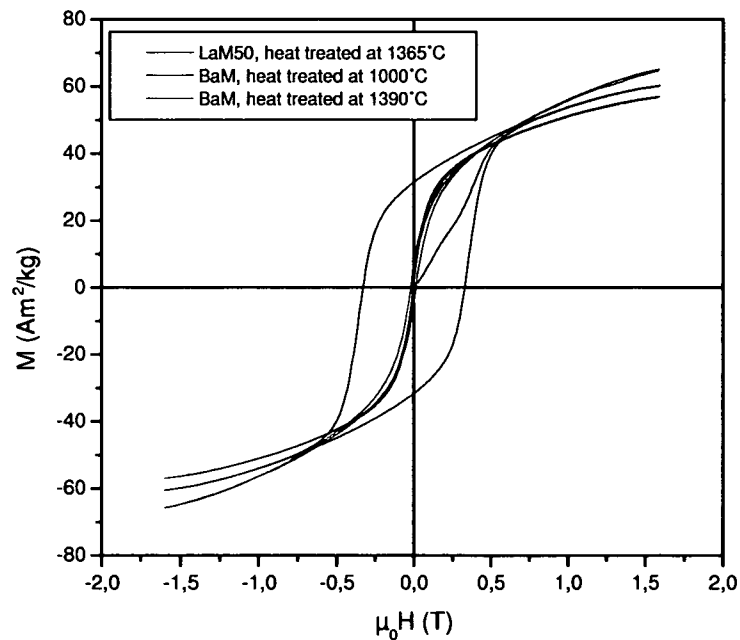


Figure 4.12: Hysteresis loop of BaM1 and BaM2 measured at room temperature in a VSM up to 1.5 T in comparison with the LaM50 sample; in BaM2 the coercivity is strongly decreased

Density

The density of LaM50 was measured with a helium pycnometer and delivered a reasonable value of 5.19 g/cm^3 . Usually the density of ferrites is around 5 g/cm^3 [73] and the same measurement delivered for a commercial Ba ferrite 4.65 g/cm^3 . The density does not depend obviously on the preparation method, since all samples were pressed before heat treatment with the same pressure ($3 \cdot 10^7 \text{ Pa}$). The measurement yielded a value of 4.22 g/cm^3 for another coprecipitated Ba ferrite and 4.29 g/cm^3 for a mechanical alloyed Sr ferrite.

X-ray densities were calculated for the mechanical alloyed samples, see chapter 4.2.1.

4.1.2 Electronic properties

Electrical resistance

Fig.4.13 shows the resistance of the mechanical alloyed La hexaferrite LaM3 measured on a pressed pellet. In clear contrast to insulating Sr hexaferrite this material is a poor conductor at room temperature. The ceramic is brittle and porous so that no sufficient control of the geometry is possible to measure conductivity. An estimate of the conductivity at room temperature is only of the order of $0.01/(\Omega\text{cm})$. With decreasing temperature the resistivity follows a semiconducting characteristic down to app. 100 K over more than two orders of magnitudes in R, as indicated by the full line in the figure. The energy gap parameter is small, only 0.07 eV, or 800 K. Below 100 K the resistance continues to increase but much less steeply, approaching the stretched exponential behavior with exponent $\nu=0.5$ shown by the dotted line. This might be associated with variable range hopping [70]. The crossover could be induced by the current flowing mainly through grain boundaries at low T, where the carriers in the semiconducting grains are frozen out. Again the change occurs around the temperature of phase transition.

Specific heat

To figure out at which temperature the phase transition appears, a measurement of specific heat C_p was performed. As shown in fig.4.14 the curve exhibits a small hump at around 110 K. This hump appears as a symmetric anomaly, which is shown in the differentiated signal, where a curve, similar to the derivative of a Gauss function occurs. This is close to a jump in $\frac{dC_p/T}{dT}$ which indicates a first order transition, but to classify this the hump is not distinctive enough. The maximum at low temperatures is the inflection point of the Debye function.

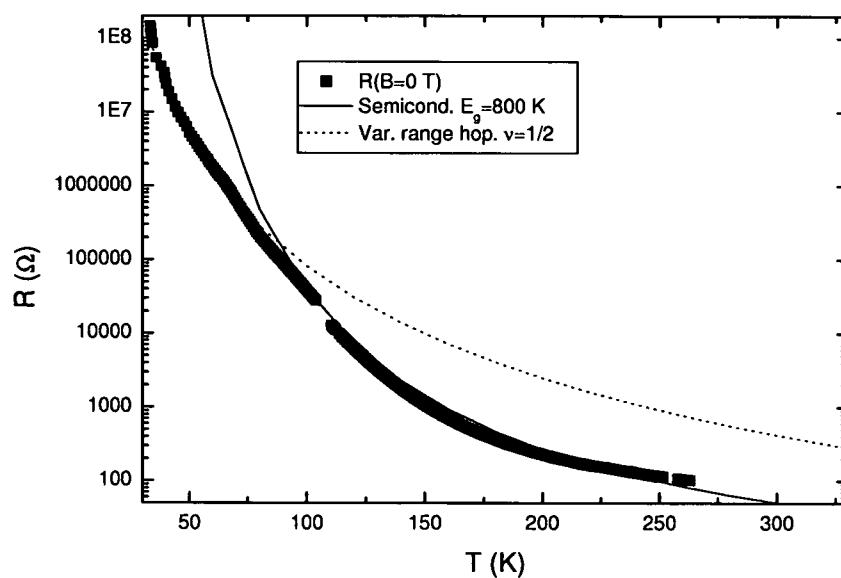


Figure 4.13: Electrical resistance of LaM3 versus temperature in logarithmic scale; above 100 K the material exhibits a semiconductor like behavior, while below a variable range hopping seems to dominate the conductivity

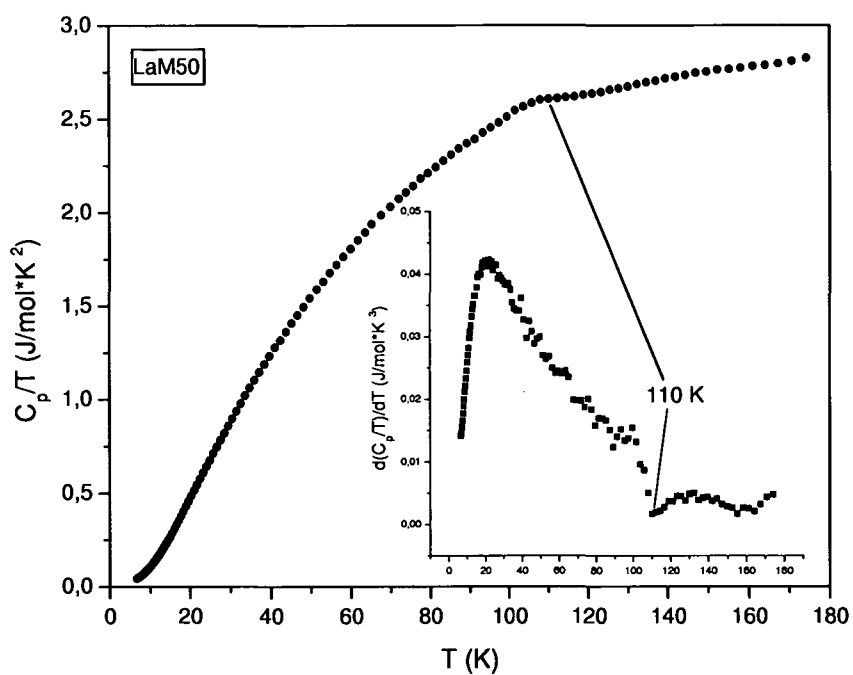


Figure 4.14: C_p/T versus T of the LaM50 sample; a hump at app. 110 K is visible indicating the phase transition from hexagonal structure at room temperature to orthorhombic structure at low temperatures

4.1.3 Magnetic properties

Susceptibility

In the susceptibility signal of the sample LaM50 again a hump at around 110 K is visible in the real part as well as in the imaginary part (see fig.4.15). Above this transition the imaginary part is very small, reversible processes seem to dominate and hysteresis losses are small. Interesting is a second hump in χ'' at around 35 K, that does neither appear in χ' nor in the specific heat (see chapter 4.1.2). This could indicate a magnetic transition without structural transition, although they usually go together in ferrites, since the Fe spins are strongly coupled to the lattice. For future experiments temperature dependent hysteresis loop measurements of magnetically aligned samples are recommended. A confirmation for this idea was also found in the anisotropy (see chapter 4.1.3) and the NMR spectrum (see chapter 4.1.4) at this temperature.

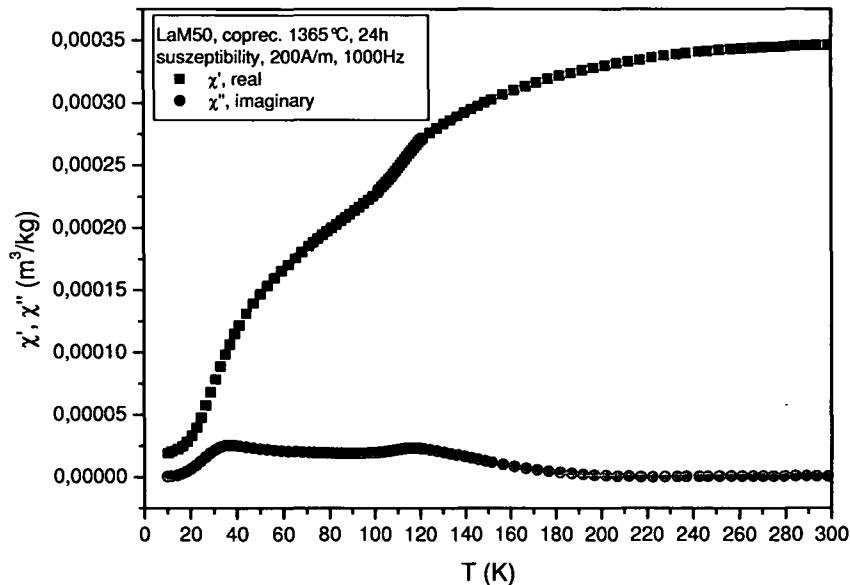


Figure 4.15: Real and imaginary part of χ versus T of the LaM50 sample; a hump at app. 110 K is visible indicating the phase transition from hexagonal structure at room temperature to orthorhombic structure at low temperatures

Magnetization

Measurements of hysteresis loop were performed at room temperature in a pulsed field magnetometer using fields up to 4.9 T and at 4.2 K in a vibrating sample magnetometer, with fields up to 15 T. At room temperature the magnetization at 4.9T was measured to $M_{LaM3}=74 \text{ Am}^2/\text{kg}$, $M_{LaM50}=65 \text{ Am}^2/\text{kg}$ and, for comparison, $M_{SrM}=72.4 \text{ Am}^2/\text{kg}$ (see fig.4.16). The value of the sample prepared by coprecipitation is significantly smaller due to an amount of 10% secondary phases, with negligible contribution to the magnetization. To estimate the saturation magnetization a plot M versus $1/H^2$ [23] was employed, yielding a value of $66.8 \text{ Am}^2/\text{kg}$ for LaM50 (see fig.4.17) and $74.7 \text{ Am}^2/\text{kg}$ for LaM3. The value of Sr hexaferrite found in literature is $74.3 \text{ Am}^2/\text{kg}$ [5].

According to the publication of Lotgering [12] the saturation magnetization of La hexaferrite is slightly decreased compared with Sr hexaferrite. This can be explained by using the Gorter model [41] (see chapter 2.2.2). In the La hexaferrite one Fe ion per formula unit has to change from a 3+ valence to a 2+ valence for charge compensation of the valence difference between La and Sr. It was pointed out in [12] that, assuming a preference of the Fe^{2+} for an octahedral site, the Fe^{2+} will enter the 2a site, giving a smaller contribution to the total magnetization of $4\mu_B$. Therefore the total magnetization of La hexaferrite at 0 K is calculated to $(12+2)*5\mu_B + 2*4\mu_B - (4+4)*5\mu_B = 38\mu_B$ per unit cell. This model is based on the assumption of localized electrons, i.e. insulators, which should be mentioned here, since the La hexaferrite, as seen in chapter 4.1.2, is a bad insulator at room temperature. Nevertheless, the value holds also for halfmetals, as shown in chapter 5.3.

To confirm this value the magnetization was measured at 4.2 K (see fig.4.18). To saturate the La hexaferrite sample it was necessary to use a high field, in this case a superconducting magnet with a maximum field of 15 T was available. The value of the saturation magnetization was again extrapolated from a M versus $1/H^2$ plot of this measurement and yielded $M_s=85.3 \text{ Am}^2/\text{kg}$ for LamM50. From X-ray analysis and Mössbauer spectroscopy it is known that the sample contains 90% of hexaferrite phase. The secondary phases give a negligible contribution to the magnetization, since

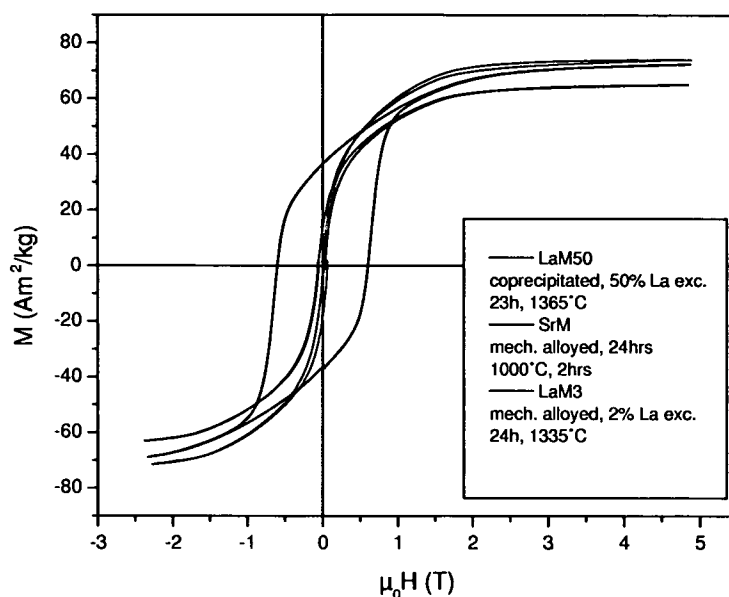


Figure 4.16: Comparison of hysteresis loop at room temperature of LaM50 and LaM3 with a Sr hexaferrite sample; the measurement was performed in a pulsed field magnetometer with a maximum field of 4.9 T and a pulse duration of 10.6 ms

LaFeO₃ and Fe₂O₃ are antiferromagnetic or exhibit a weak ferromagnetism. This leads to a value of 94.8 Am²/kg for the pure La hexaferrite, which is equal to 18.9 μ_B/formula unit, calculated with $(M[emu/g] * \text{weight per mol}) / (N_A \mu_B) = \mu_B / \text{formula unit}$ (N_A is the Avogadro constant). This is in good agreement with the value of 19.2 μ_B/formula unit reported by Lotgering and the calculation following the Gorter model.

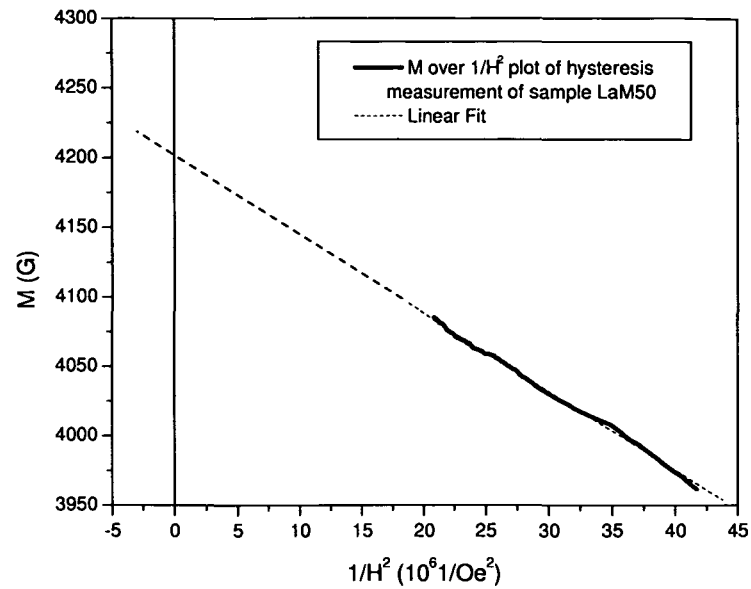


Figure 4.17: M versus $1/H^2$ plot of a magnetization measurement up to 4.9 T of sample LaM50; from this plot the value of the saturation magnetization was extrapolated

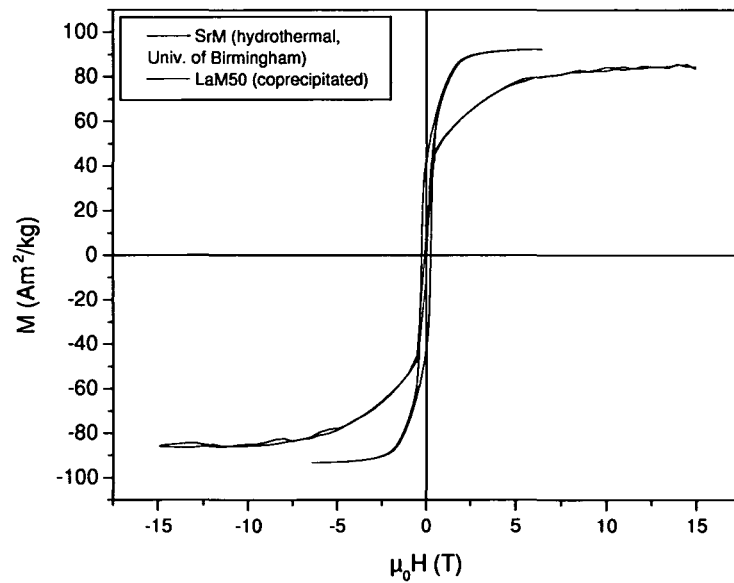


Figure 4.18: Comparison of the hysteresis loops at 4.2 K of LaM50 with a Sr hexaferrite sample; the measurement was performed in a vibrating sample magnetometer with a maximum field of 15 T and a frequency of 81 Hz

Magnetocrystalline anisotropy

The magnetocrystalline anisotropy of the samples was measured in a pulsed field magnetometer using the singular point detection method (SPD; [72]). This method uses the fact that the second derivative of the magnetization with respect to the field exhibits a singularity at the anisotropy field for materials with uniaxial anisotropy. Fig.4.19 shows the temperature dependent anisotropy field of the LaM50 sample in comparison with a Sr hexaferrite prepared by hydrothermal synthesis. The anisotropy exhibits a remarkable increase from 1.64 T at room temperature up to 4.01 T at 10 K. This is in agreement with Lotgering [12], who reported a value of around 40 kOe for the anisotropy field at 4.2 K. This increase was explained by the change from Fe^{3+} to Fe^{2+} at one of the lattice sites, which results at one hand in a change of magnetization and at the other hand in a contribution to the anisotropy constant K_1 because of the orbital momentum of Fe^{2+} . From magnetization measurements it is known, that the Fe^{2+} can enter only a lattice site with negative magnetization contribution (which means a spin up site) and positive K_1 contribution. For the mechanical alloyed sample LaM3 only the values at room temperature and 4.2 K are shown and they match with the ones of the coprecipitated La hexaferrite. A change in the slope is visible at around 110 K, which is the temperature of the phase transition. Due to the distortion it seems a change in crystal field appears, which leads to a smaller increase in anisotropy. Evident is also a hump at around 10 K. This hump may be associated with the splitting of the 16h site in the NMR spectrum (see later chapter 4.1.4) and the hump in the susceptibility although they occur at slightly different temperatures. All this indicates a magnetic transition.

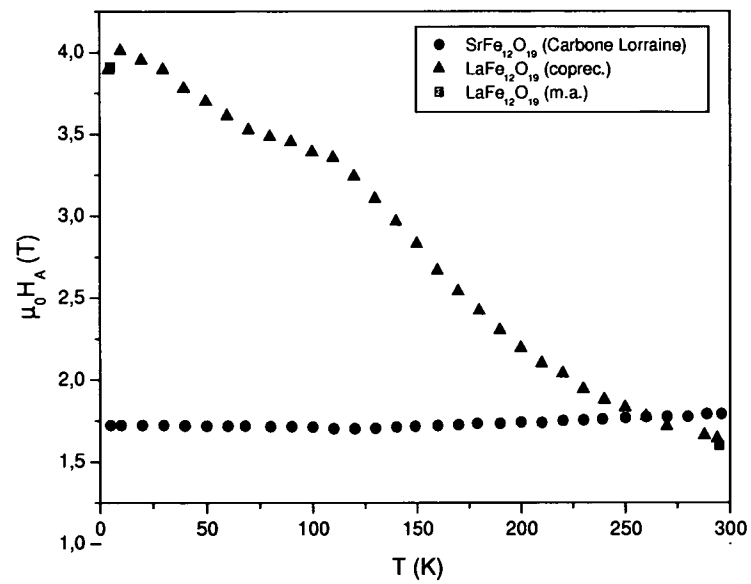


Figure 4.19: Comparison of anisotropy field from room temperature down to 4.2 K of La ferrite with a Sr hexaferrite sample; the measurement was performed in a pulsed field magnetometer with a maximum field of 8 T and a pulse duration of 2 ms (half wave), using the SPD technique

Hysteresis loop and coercivity

Evident in the hysteresis loop at room temperature is a very small coercivity compared with conventional hexaferrites. The Sr hexaferrite sample in fig.4.16, which was prepared by mechanical alloying, shows a typical coercivity of 0.6 T, while for the La ferrite it is around 0.05 T, like in a soft magnetic material. It was found that the reason is the big grain size of the sample, since the hexaferrite phase is formed only with a heat treatment at very high temperatures (see chapter 4.1.1).

Two attempts to reduce the grain size and so enhance the coercivity were made. In the first one the La hexaferrite was milled in a ball mill for a few minutes and coercivity and magnetization were checked in a VSM after every minute. This procedure should break the grains and indeed the coercivity was increased (see fig.4.20). But simultaneously the magnetization was reduced by 35% and this already after 10 min milling (see fig.4.21). The coercivity was after 10 min with 0.065 T still very small compared with conventional hexaferrites. XRD revealed that the reason for the reduced magnetization is an increased amount of secondary phase (hematite) in the sample. It seems, that the energy of a few minutes milling is sufficient to stimulate the decomposition of the metastable La hexaferrite compound.

What is usually done in ferrite production to prevent grain growth is to mix the ferrite with some additives like SiO_2 or CaO , mill it again and sinter it afterwards [74]. These additions work as pinning centers for the grain boundaries, since the strain energy of such impurities is lower at the surface, which is also the reason why most of the impurities are found in the grain boundaries. According to the experience with milling the La ferrite, this procedure may not be possible. Therefore a simple approach was tried, adding SiO_2 to the starting materials, mill all together, followed by the heat treatment within the temperature range of stability of the La hexaferrite phase. A composition of $\text{La}_2\text{O}_3+12\text{Fe}_2\text{O}_3+0.15\text{SiO}_2$ was chosen for the sample LaM7. Fig.4.22 shows the hysteresis loop of this sample in comparison with sample LaM3, measured in a pulsed field magnetometer with pulse duration 10.6 ms. A significant reduction by 42% of the magnetization is visible, which can not be only due to not magnetically ordered secondary phases formed by Si. It

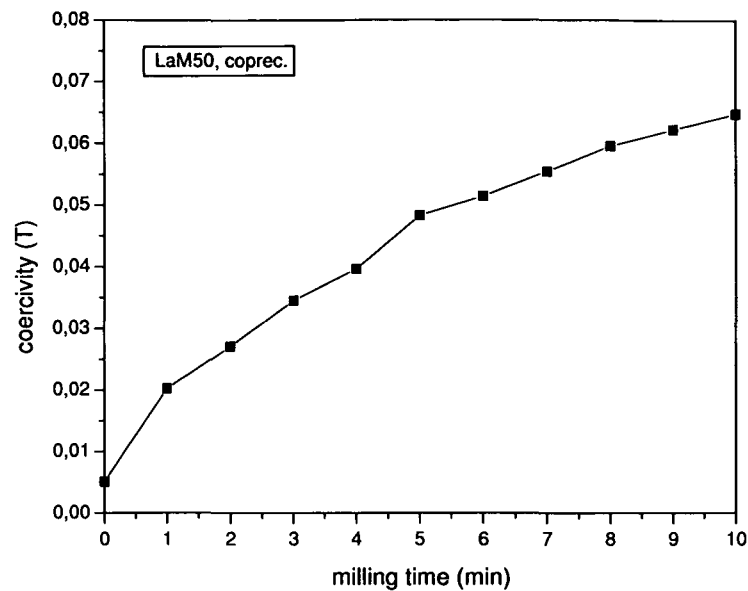


Figure 4.20: Coercivity of the sample LaM50 after a few minutes of milling in a ball mill

seems that the addition of SiO_2 stimulated the formation of other phases and hindered the formation of the hexaferrite phase. XRD revealed as secondary phase 12% of Fe_2O_3 , which cannot explain the reduction of magnetization. Probably an amount of X-ray amorphous phase containing Si is responsible for this reduction. The lattice parameters of the hexaferrite phase are with $a=5.888 \text{ \AA}$ and $c=22.895 \text{ \AA}$ almost the same as for the LaM3 sample, which leads to the assumption that no Si entered the lattice. A substitution of Fe by Si is also not likely, because of the different valence. On the other hand Si entering the grain boundaries would be not visible in the XRD pattern. A series of samples prepared only with SiO_2 and Fe_2O_3 would be useful to observe the possible phases formed.

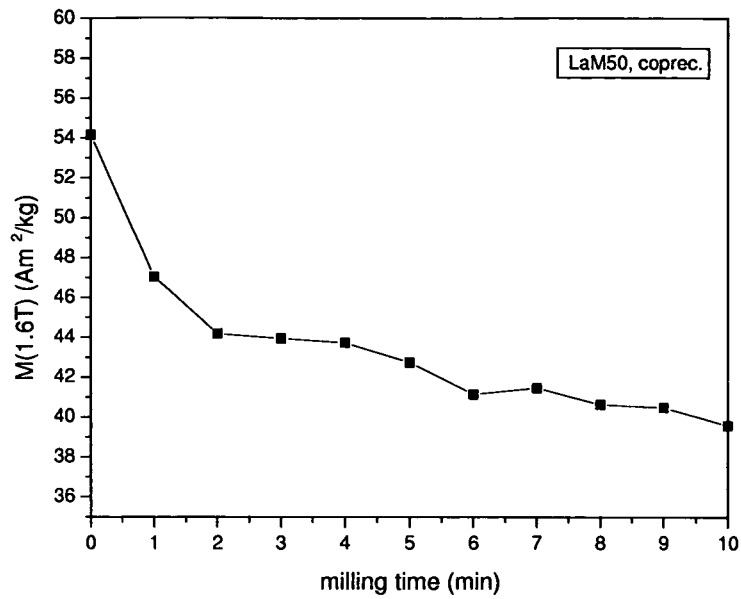


Figure 4.21: Magnetization of the sample LaM50 after a few minutes of milling in a ball mill

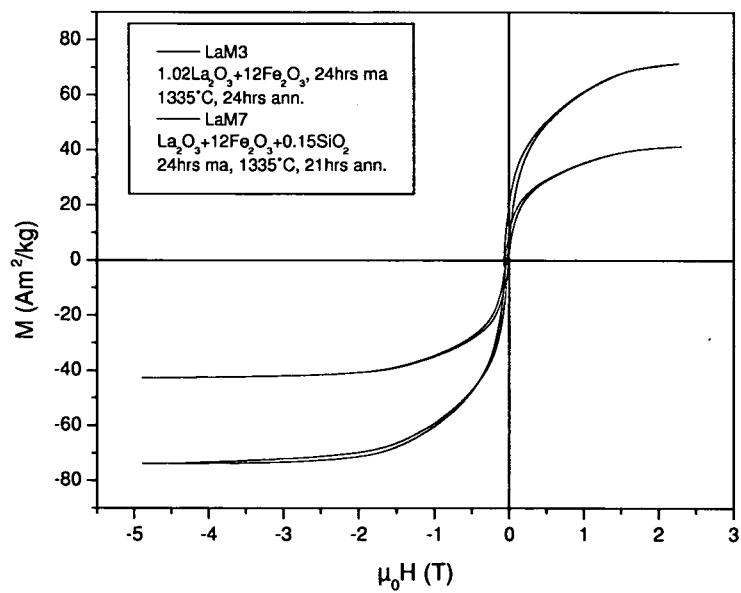


Figure 4.22: Hysteresis of the sample LaM7, milled with a small amount of SiO_2 , compared with LaM3

4.1.4 Local probes

Mössbauer spectroscopy

In order to check the presence of the Fe^{2+} ion and find a preference for one of the lattice sites, Mössbauer spectroscopy was performed. Fig.4.23 shows the room temperature spectrum of the coprecipitated LaM50 sample with app. 4% Fe_2O_3 and app. 6% LaFeO_3 of secondary phases. Since the secondary phases contain iron the fit was difficult to perform, due to some line overlap. The best result was obtained, assuming that Fe^{2+} enters the 2a site. Since

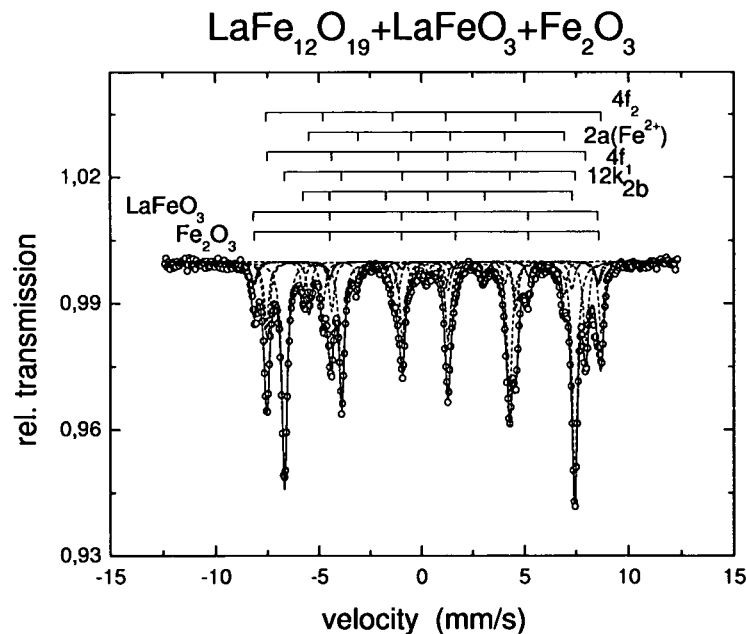


Figure 4.23: Mössbauer spectrum of the LaM50 sample at room temperature; a satisfying fit is obtained with Fe^{2+} at the 2a site

this method is sensitive to changes in the local surrounding of the Fe ions, it was interesting to perform temperature dependent measurements in order to monitor the phase transition. From these spectra the hyperfine fields of all Fe sites were derived and plotted versus temperature (see fig.4.24). All iron sites except 2a exhibit a typical increase in hyperfine field with decreasing

temperature according to

$$B_{HF}(T) \propto \bar{S}_z(T) \propto M(T) \quad (4.1)$$

[75], which was also observed in conventional Sr ferrite (see fig.4.25). At the 2a site the hyperfine field, which is already at room temperature significantly reduced compared to Sr hexaferrite (35%), decreases even 25% more down to around 120 K and stays constant at lower temperatures or increases slightly, respectively. This can be explained by the unquenched orbital momentum of the Fe^{2+} ion at the 2a site, because then a factor of opposite sign proportional to the orbital momentum is added to the hyperfine field in 4.1 (see chapter 2.1.2). It means that the orbital momentum is established from room temperature down to 120 K leading to an increasing anisotropy field until it reaches its equilibrium. At lower temperatures the orbital momentum stays constant and in the hyperfine field only the temperature dependence of the spin term can be observed, which leads to a slight increase.

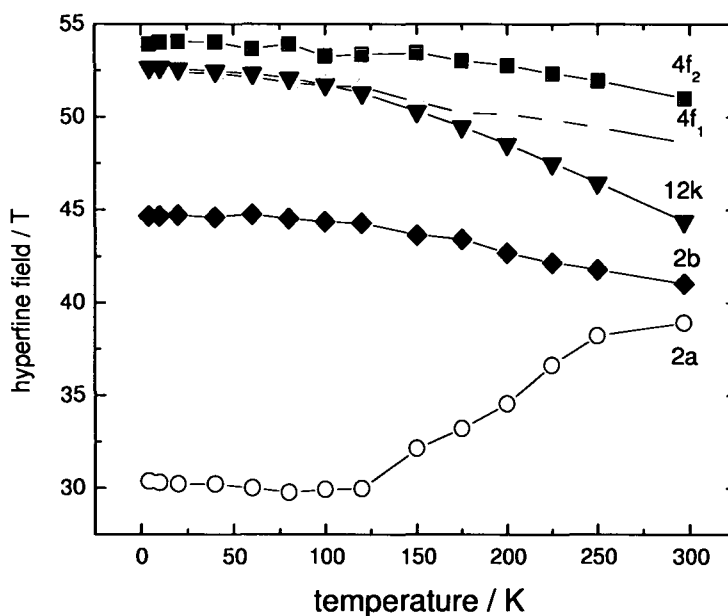


Figure 4.24: Hyperfine field versus temperature of the 5 Fe sublattices in LaM50 calculated from Mössbauer spectra

The quadrupole shift, which is a measure for the electrical field gradient

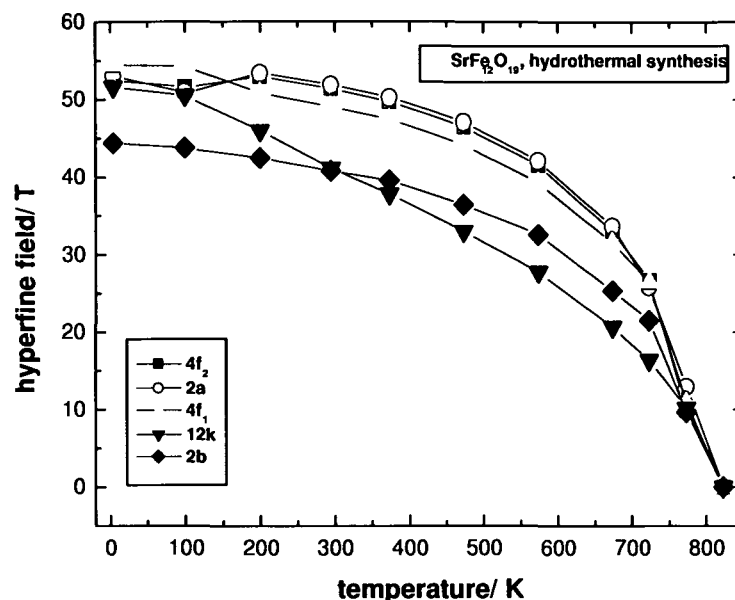


Figure 4.25: Hyperfine field versus temperature of the 5 Fe sublattices in Sr ferrite (prepared by hydrothermal synthesis at University of Birmingham) calculated from Mössbauer spectra

at the nucleus, shows the opposite behavior as the hyperfine field. At room temperature the quadrupole shift is small at all sites except 2b, which is a bipyramidal site, since all other have a symmetry close to cubic symmetry exhibiting either octahedral or tetrahedral coordination. Therefore it is also small at the 2a site (octahedral coordination) and almost constant down to 120 K. At this temperature the orbital momentum is fully established, but with the bigger Fe^{2+} ion and the unquenched momentum the structure seems not yet to be in equilibrium and so a lattice distortion starts. This leads to a distortion of the O octahedra surrounding the Fe^{2+} , visible in the decreasing quadrupole shift with decreasing temperature. At 4.2 K a negative quadrupole shift was observed in contrast to the value at room temperature (see. fig.4.26).

The isomer shift of the 2a site is at room temperature more positive than on all other sites. This is a clear indication for the Fe^{2+} , since an additional electron in the 3d orbital due to a screening effect reduces the attraction of the nucleus for s electrons. Fe^{2+} has one electron more in the

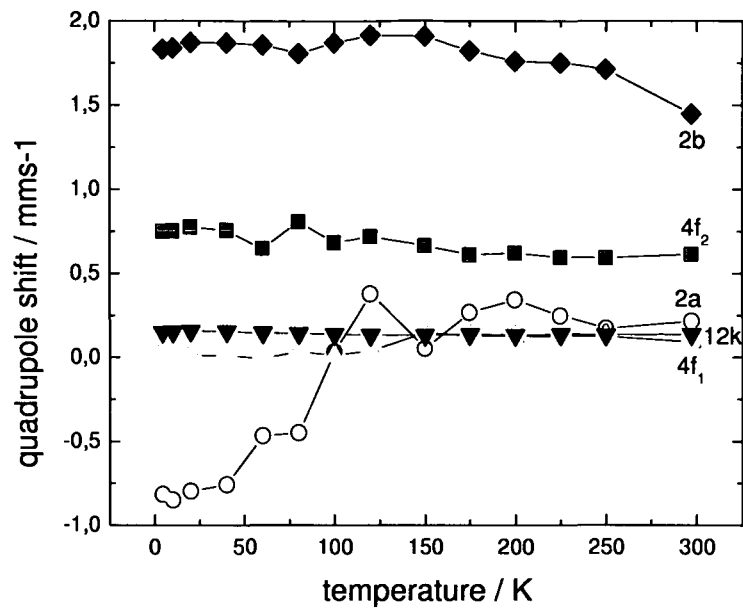


Figure 4.26: Quadrupole shift versus temperature of the 5 Fe sublattices in LaM50 calculated from Mössbauer spectra

3d orbital than Fe^{3+} , so that its electron density at the nucleus is lower than for the Fe^{3+} . Surprisingly, with decreasing temperature the isomer shift gets smaller down to the temperature of the phase transition and increases again at lower temperatures. The decrease may be explained by establishing the orbital momentum of the Fe^{2+} ion, which leads to an expansion of the 3d orbital, that reduces the screening of the s electrons and increases the electron density at the nucleus site. The increase at lower temperatures, when the orbital momentum is fully established, may be due to a distortion of the 2a oxygen octahedra, since the 3d orbital of the Fe ion is coupled through superexchange with the 2p orbital of the O ions. Imagine a distortion in form of a compression along the c-axis of the octahedra (see fig.4.28). The 2p orbital of the O ions in the base move closer to the 3d orbital of Fe leading to a reduction of the 3d orbital. This leads to an increased screening and an increased isomer shift.

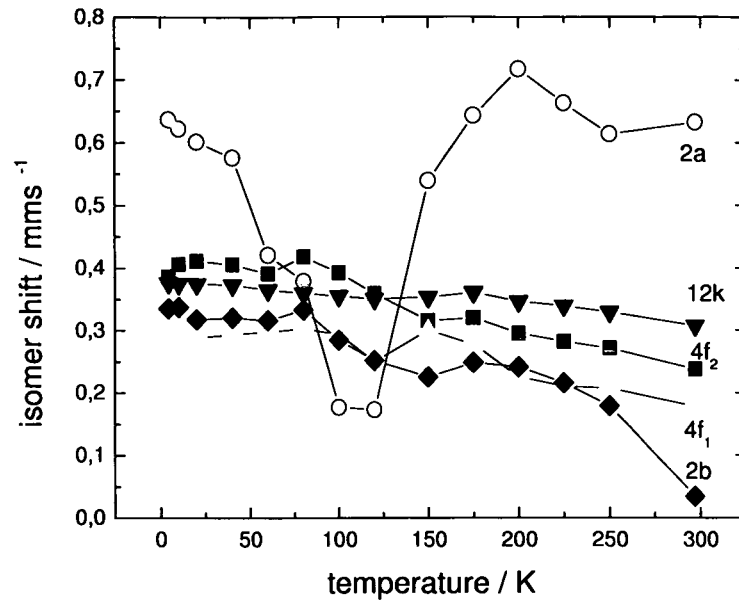


Figure 4.27: Isomer shift versus temperature of the 5 Fe sublattices in LaM50 calculated from Mössbauer spectra

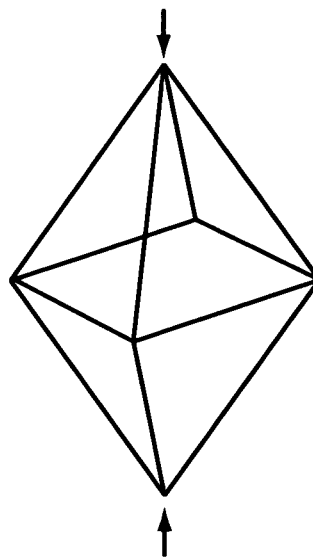


Figure 4.28: Possible distortion of 2a oxygen octahedra leading to an increase in the isomer shift

Nuclear magnetic resonance

The samples were also investigated by nuclear magnetic resonance using the spin-echo method of the ^{57}Fe isotope. The spectrum at 4.2 K (see fig.4.29) shows a significant deviation from the one of conventional Sr hexaferrite, which was expected due to the phase transition occurring at low temperatures. All lines of the five Fe sublattices are shifted. Both 4f sites are shifted to lower frequencies and correspond in the distorted lattice to 8f1 and 8f2. 12k is shifted to higher frequencies corresponding to 16h, which represents two third of the 12k site. One third of the 12k intensity is missing and may be the broad hump starting at 70.5 MHz and reaching up to the 16h peak, corresponding to the orthorhombic 8f3 site. This is difficult to assign, since at that frequency also the wall signal of the 8f1 line is observed. This splitting of the 12k site cannot be observed in the Mössbauer spectrum, due to the lower resolution. Unfortunately 2a and 2b could not be observed, probably due to too short relaxation times. According to the Mössbauer results of the hyperfine fields (see tab.4.4) the 2a line should be at 41.8 MHz due to $B_{hf} = \frac{1}{\gamma}f$ with the gyromagnetic ratio $\gamma = 1.3757\text{MHz/T}$ for ^{57}Fe , even lower than the 2b site in the undistorted lattice of Sr ferrite (59.5 MHz). The 2b site should shift to the higher frequency of 61.5 MHz. Already in Sr hexaferrite it is difficult to obtain a signal of the 2b site, since the Fe ion is jumping between two 4e positions in the bipyramidal coordination [35]. In the La hexaferrite it was not possible to find the signal of the 2b site, due to some strongly fluctuating fields, which are reducing the relaxation time. The same seems to happen for the 2a site.

Fig.4.30 shows the shift of the Fe lines in an external field. The sample was a powder sample that aligns with the easy axis parallel to the external field. This field gives a positive or negative contribution to the hyperfine field, depending on the orientation of the external field with respect to the Fe spin, following again $\Delta B_{hf} = \frac{1}{\gamma}\Delta f$. For a site with spins parallel to the external field (spin up site) the hyperfine field is orientated antiparallel due to the core polarisation and therefore the external field gives a negative contribution, and vice versa for a spin down site. This leads to a positive slope of γ for the spin down sites 8f1 and 8f2 and a negative slope for the spin up site 16h.

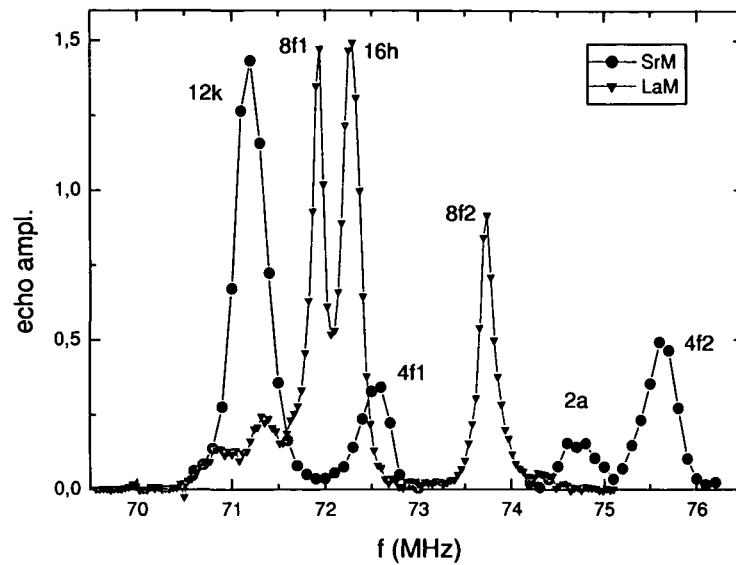


Figure 4.29: Pointwise Fourier transformed NMR spectrum of LaM3 in comparison with Sr ferrite (sintered)

For small fields the frequency stays constant due to the shielding effect of the demagnetizing field $H_D = -NM$, where $N = N_{ij}$ is a tensor of second order, and can be analytically determined only for ellipsoid particles. Only for special geometries it can be a factor, called the demagnetizing factor, like eg for spherical particles. Here $\mu_0 H_D \approx 0.15$ T. For the 16h site two values are shown 16ha and 16hb because this site exhibits a splitting at higher temperatures (see fig.4.31). It is not yet clear, what causes the splitting, but it is likely, that it is associated with a magnetic transition, which was also observed in the susceptibility at around 35 K (see chapter 4.1.3).

In addition the ^{139}La resonance was measured (see fig.4.32), keeping the frequency at 35 MHz and using a field sweep. The La peak in a diamagnetic reference would appear at this frequency at $B_{dia}=5.82$ T. The gyromagnetic ratio of La is $\gamma=6.0146$ MHz/T and its nuclear spin $I=7/2$. Therefore $2I=7$ lines corresponding to the transitions $\Delta m=1$ between the quadrupole split energy levels are visible. According to the formula $I(I+1)-m(m-1)$ [76] the relative intensity should be highest in the middle, where m is smallest. This is not observed in the NMR spectrum due to relaxation effects. It is well known from various ferromagnets that relaxation via virtual spin-wave

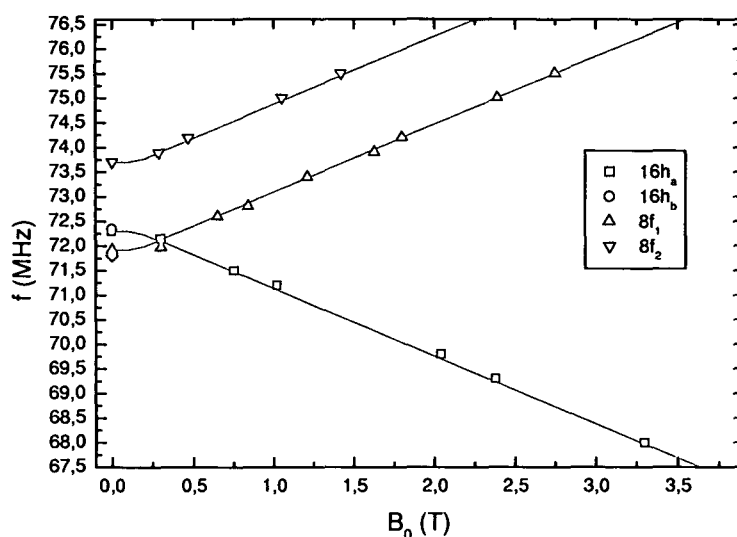


Figure 4.30: Shift of Fe resonance with field

excitations can lead to this effect [77, 78]. In addition a reduction of the intensities is visible due to a reduced amplification factor, which is reciprocally proportional to the field. The transferred hyperfine field was calculated from the difference between the field of the central line and B_{dia} to $B_{hf}=1.35$ T. The line shift with increasing external field are shown in fig.4.33. The values fit well on a line with the slope γ , which is only the case since the powder aligns parallel to the external field. The quadrupole splitting can be read easily from this figure and is 3.85 MHz or $\pm 10.13 \cdot 10^{21}$ V/m² electrical field gradient at the nucleus site.

Fig.4.34 shows a comparison between hyperfine fields measured with NMR and Mössbauer technique. In tab.4.4 the good agreement at 4.2 K is obvious. Unfortunately it is not possible to compare the values of the interesting 2a site and the 2b site. The values of the 8f2 site are slightly higher with Mössbauer and to distinguish the 16ha and 16hb sites the resolution of Mössbauer is too low.

Fig.4.35 shows the temperature dependence of the spin-lattice (T_1) and the spin-spin (T_2) relaxation time of the 8f1 peak in LaM. The relaxation times decrease rapidly with temperature and no signal was observed above 35 K. T_1 and T_2 are proportional with a factor of 200. This indicates, that both

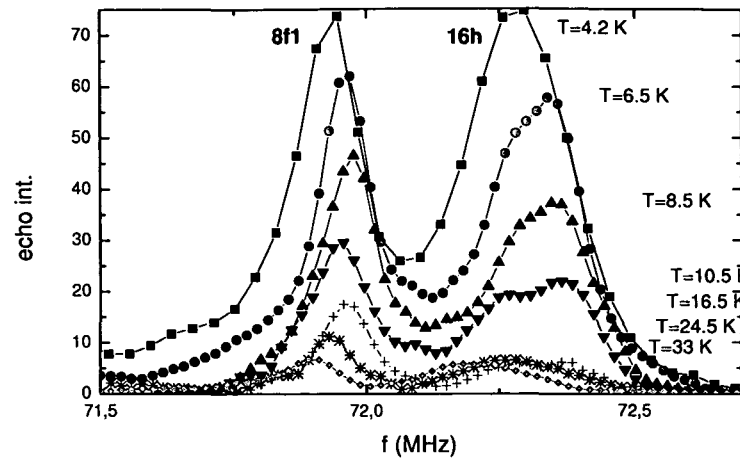


Figure 4.31: Temperature dependence of the 16h site in the spectrum of LaM3; the site shows a splitting at higher temperatures

Table 4.4: Hyperfine fields at 4.2 K calculated from NMR and Mössbauer measurements

	Bhf4f2 (T)	Bhf2a (T)	Bhf4f1 (T)	Bhf12k (T)	Bhf2b (T)
Mössbauer	53.91	30.38	52.32	52.67	44.67
NMR	53.59	-	52.29	52.55	-

times couple to the same relaxation process, due to fluctuating fields [79]. For this case the relation between T_1 and T_2 can be written as $\frac{1}{T_2} = \frac{\alpha}{T_1} + \beta$.

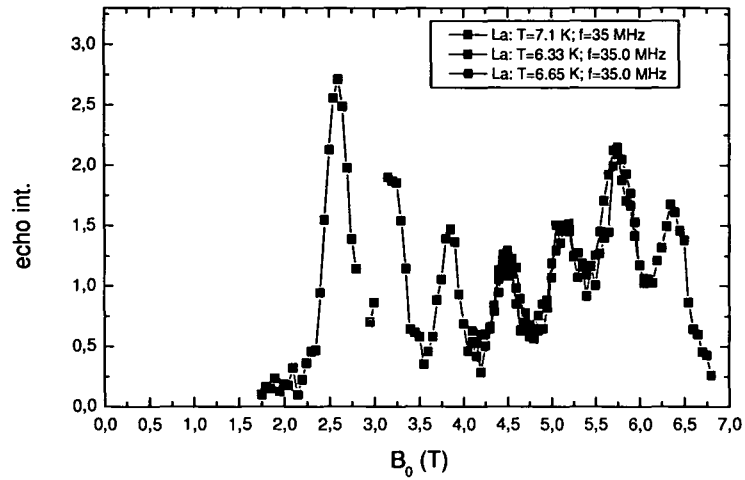


Figure 4.32: La resonance of LaM3

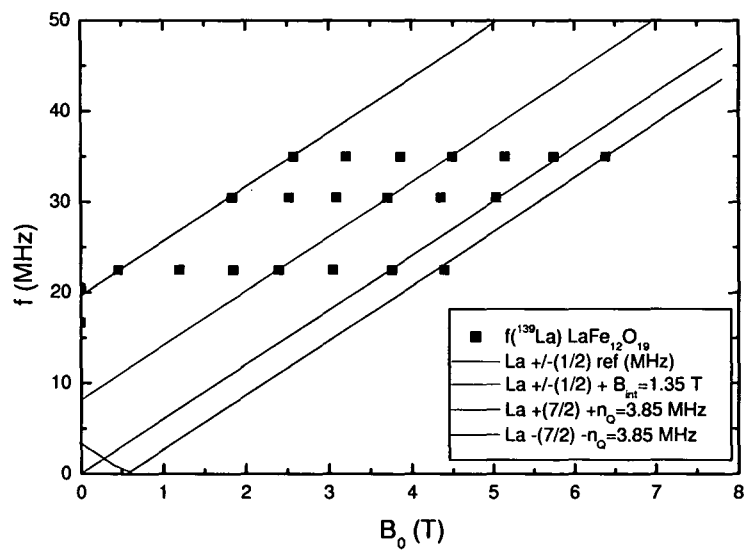


Figure 4.33: Shift of La resonance septett with field

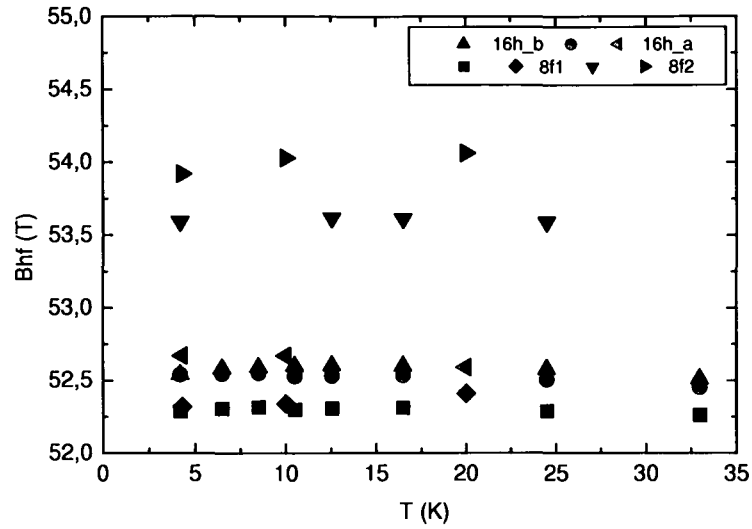


Figure 4.34: Comparison between hyperfine fields measured with NMR and Mössbauer spectroscopy, the first symbol corresponds to the NMR values

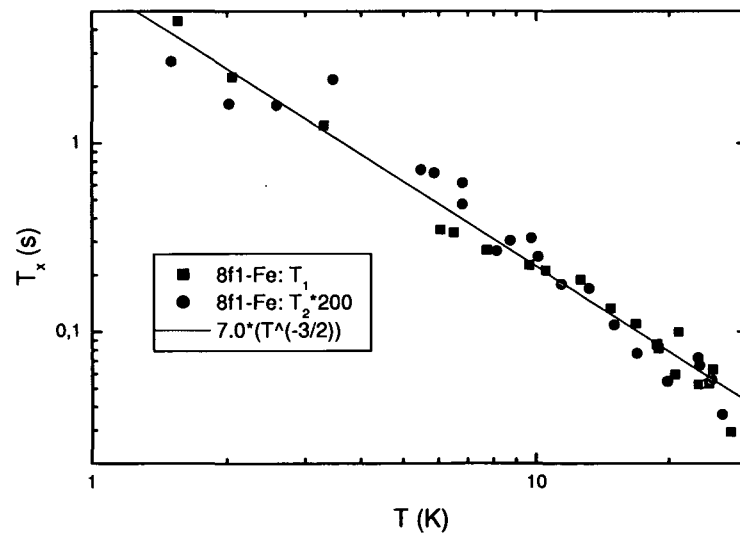


Figure 4.35: Temperature dependence of the relaxation times of the 8f1 Fe site in LaM3

Neutron diffraction

The magnetic moments at the different Fe sites in the hexagonal crystal structure of the La ferrite were determined by neutron diffraction. This gives a hint for the Fe^{2+} preference, since the spin magnetic moment of Fe^{2+} is reduced by $1\mu_B$ in comparison with Fe^{3+} , that has a spin moment of $5\mu_B$. The observed magnetic moments at room temperature are shown in tab.4.5. Four different experiments were performed: a) high resolution experiment at the D2B spectrometer using a wavelength of 1.4 \AA ; b) experiment at the D20 spectrometer with wavelength 1.6 \AA and a $10'$ collimator; c) experiment at the D20 spectrometer with wavelength 1.6 \AA using full flux and only the central part of the detector; d) experiment at the D20 spectrometer with wavelength 1.6 \AA using full flux and the full height of the detector. A reduction of the magnetic moment is visible at the 2a site, which is in agreement with the Mössbauer measurements. The magnetic moment is for all sites much lower than $5\mu_B$, because a significant part is transferred to the oxygen ions, and a part of electrons is in the interstitial region, which is in agreement with the conductivity of the sample at room temperature (see also chapter 4.1.2). Another reason is that the measurement was performed at room temperature, where the magnetization is app. 10% lower than at 0 K.

Table 4.5: Magnetic moments at room temperature at the different Fe sites determined by neutron diffraction; a)D20, 1.4\AA ; b)D2B, 1.6\AA , $10'$ Coll; c)D2B, 1.6\AA , Fullflux1; d)D2B, 1.6\AA , Fullflux2

Fe site	μ_B a)	μ_B b)	μ_B c)	μ_B d)
12k	3.6	3.8	3.8	3.7
4f2	3.8	3.7	4.0	4.1
4f1	3.8	3.9	3.9	3.7
2b	3.5	3.9	4.0	3.9
2a	3.4	3.4	3.5	3.1

4.2 La substituted Sr hexaferrite

For an overview of samples investigated within this group see the table in chapter 3.1.1.

4.2.1 Structural properties

X-ray diffraction

With X-ray diffraction the change in lattice parameters with respect to the La concentration was analyzed. Fig.4.36 shows the change in the lattice parameter a of mechanical alloyed samples with different La concentration, calculated by Topas from room temperature X-ray diffraction. An increase of only 0.2% from $x=0$ to $x=1$ (x...La concentration) occurs, but it is not linear in the concentration and exhibits a bigger slope at higher concentrations. The values are plotted for different concentrations. One is the nominal concentration, which means the concentration used for the starting materials. In most cases this is not the concentration in the compound, e.g. in the coprecipitated samples it was necessary to add a certain La excess in order to keep the amount of secondary phases as low as possible. Nevertheless in mechanical alloyed samples the error between nominal concentration and effective concentration can be assumed as small, since for the pure La ferrite only an excess of 2% La was necessary. This assumption is only valid if the sample exhibits no secondary phases containing La or Sr, which is the case for all samples. As discussed already in chapter 3.1.1 it is not clear, what happened in the samples with $x=0.33$, $x=0.5$ and $x=0.75$, where hematite was found to be the only secondary phase. But since these samples also fit in the line of values (see fig.4.37 and fig.4.38), the concentration may not deviate too much from the nominal one. Nevertheless the occupation, which is proportional to the concentration, was calculated by Topas and these are the circles in the plots. These values are only approximations, since they depend strongly on the starting parameters of the iteration. For all concentrations, except $x=1$ and $x=0$, where the occupation was not refined, they are higher than the nominal ones. Another interesting result is, that a good fit was only obtained for a total occupation of Sr plus La smaller than 1, in worst cases

up to 10% smaller, and the same happened for the Fe sites. This could mean a high amount of defects in the structure. However, this result is doubtful, since no confirmation was found in the NMR measurements which should be sensitive to a high amount of defects in the local surroundings of Fe sites. Another possible explanation is, that the Co radiation is highly absorbed in the Fe containing sample, and this more at higher angles, where the path in the sample is longer. This leads to an effect in the pattern, that the program tries to fit with low occupation values. In any case the value $x=1$ is an outlier and one of the possible explanations could be the difference in preparation, since the starting materials were here only oxides, while for the partly substituted samples La and Sr carbonate were used. Another explanation may be an essential difference in the crystal structure, because in contrast to the partly substituted samples the pure La ferrite exhibits a lattice distortion at low temperatures (see chapter 4.1.1).

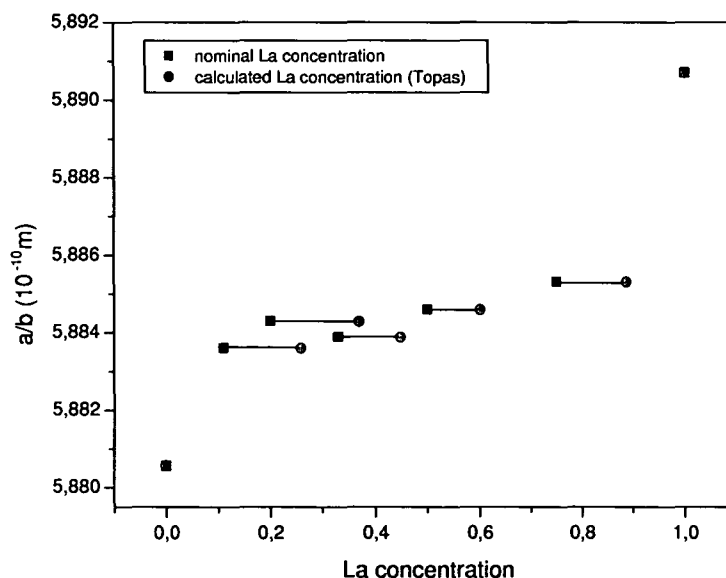


Figure 4.36: Change in lattice parameter $a=b$ with the La substitution, all samples were prepared by mechanical alloying and XRD was performed at room temperature

While parameter a increases with the La concentration, the lattice parameter c decreases (see fig.4.37). This decrease is stronger than the increase

in a so that the unit cell volume decreases, too (see fig.4.38). For the volume a linear fit is more suitable, according to the Vegard law [80, 81]. For the calculated concentrations the fit is good for all values. For the nominal concentrations the value $x=1$ appears again as an outlier, all other concentrations fit nicely on the line. Table 4.6 gives an overview of the measured

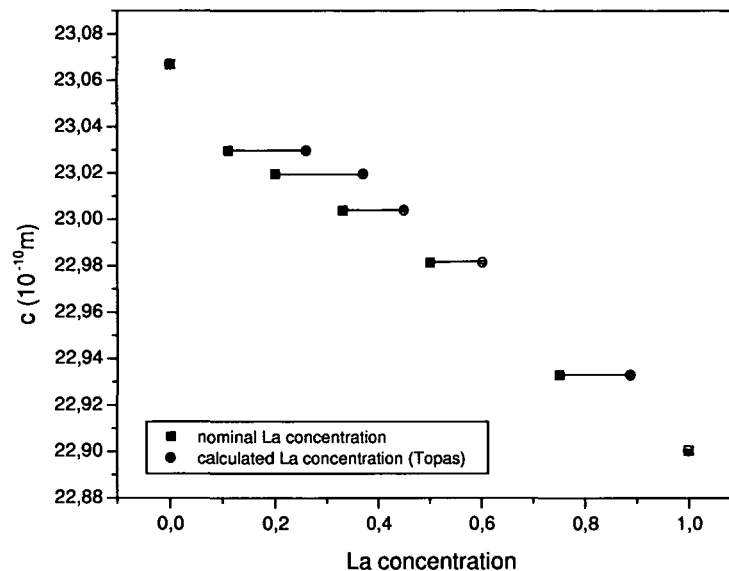


Figure 4.37: Change in lattice parameter c with the La substitution, all samples were prepared by mechanical alloying and XRD was performed at room temperature

and calculated values.

In addition x-ray density and crystallite size were calculated (see tab.4.7). In this case the x-ray crystallite size, which is in the order of 100 nm, does not coincide with the grain size, which was determined to be around 100 μm . It corresponds to a coherence length for the x-rays, which can be much smaller than the grain size, due to changes of texture or defects within the grains. The x-ray density is with $\approx 5 \text{ g/cm}^3$ comparable with literature values for SrM (e.g. 5.14 g/cm^3 [30]), but smaller for the mixed ferrites, than for the pure ones, LaM3 and SrM.

For the best Rietveld fits with Topas a slight texture in the direction of the c-axis (001) was assumed, except for SrM, which showed no texture. The R values for all fits were smaller than 5, except for the sample SrLa2.1, where

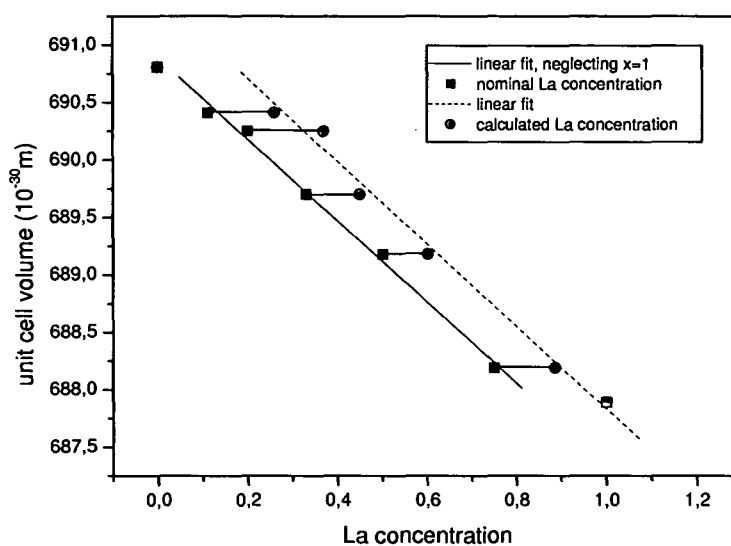


Figure 4.38: Change in unit cell volume with the La substitution, all samples were prepared by mechanical alloying and XRD was performed at room temperature

a texture in two directions, that may arise from a magnetic ordering of the grains, made the fit problematic. Nevertheless with a value around 10, the result is still acceptable. For future investigations it is recommended to perform a very accurate XRD with the sample mixed with Bi oxide, to separate the crystallites. From this the distances between Fe and the neighboring O ions could be calculated, to find an indication for Fe^{2+} , which has a bigger ion size than Fe^{3+} .

Table 4.6: Comparison of lattice parameters a and c of mechanical alloyed samples; x_{nom} is the nominal La concentration according to the starting materials, x_{calc} is the with Topas calculated La concentration; vol_{uc} is the volume per unit cell; sec.ph. is the amount of secondary phase in the sample, in this case Fe_2O_3

name	x_{nom}	x_{calc}	$a=b$ [$10^{-10}m$]	c [$10^{-10}m$]	vol_{uc} [10^{-30}]	sec.ph. [%]
SrM	0	0	5.8806	23.0669	690.81	0
SrLa8_1	0.11	0.26	5.8836	23.0296	690.41	0
SrLa4_1	0.2	0.37	5.8843	23.0196	690.25	0
SrLa2_1	0.33	0.45	5.8839	23.0039	689.70	8
SrLa1_1	0.5	0.602	5.8846	22.9814	689.18	6
SrLa1_3	0.75	0.887	5.8853	22.9329	688.19	12
LaM3	1	1	5.8907	22.9003	687.89	0

Table 4.7: X-ray density (x-ray dens.) and crystallite size (crys. size) of mechanical alloyed samples; x_{nom} is the nominal La concentration

name	x_{nom}	x-ray dens. [g/cm^3]	crys. size [nm]
SrM	0	5.105	106
SrLa8_1	0.11	5.027	200
SrLa4_1	0.2	5.017	239
SrLa2_1	0.33	4.902	184
SrLa1_1	0.5	4.988	182
SrLa1_3	0.75	4.949	186
LaM3	1	5.133	226

Neutron diffraction

In order to check if a phase transition like in LaM occurs also for the partly substituted SrM samples, neutron diffraction was performed. Fig.4.39 shows a part of the temperature dependent diffractograms of La hexaferrite, Sr hexaferrite and two different La substituted Sr ferrites with La/Sr ratios of 1/2 and 3/1. Only the angles, where due to the phase transition changes in the peaks occur, are shown. Both partly substituted samples exhibit a very similar pattern, although their magnetic behaviour is very different, having a increased anisotropy at low temperatures for La/Sr=3/1 and a reduced for La/Sr=1/2. Their diffractograms differ from the La ferrite as well as from the Sr ferrite. The shift of the 4 visible peaks indicates the change in the lattice parameters with the La concentration. The two peaks in the middle move, starting from SrM, where they are separated, closer, ending up in LaM as almost one peak. The left one from this both corresponds to (2 2 14), and shifting to higher angles means a decrease of the c-axis, while the a-axis increases according to the shift of the other peaks. The main observation is, that no phase transitions are visible except for the La ferrite.

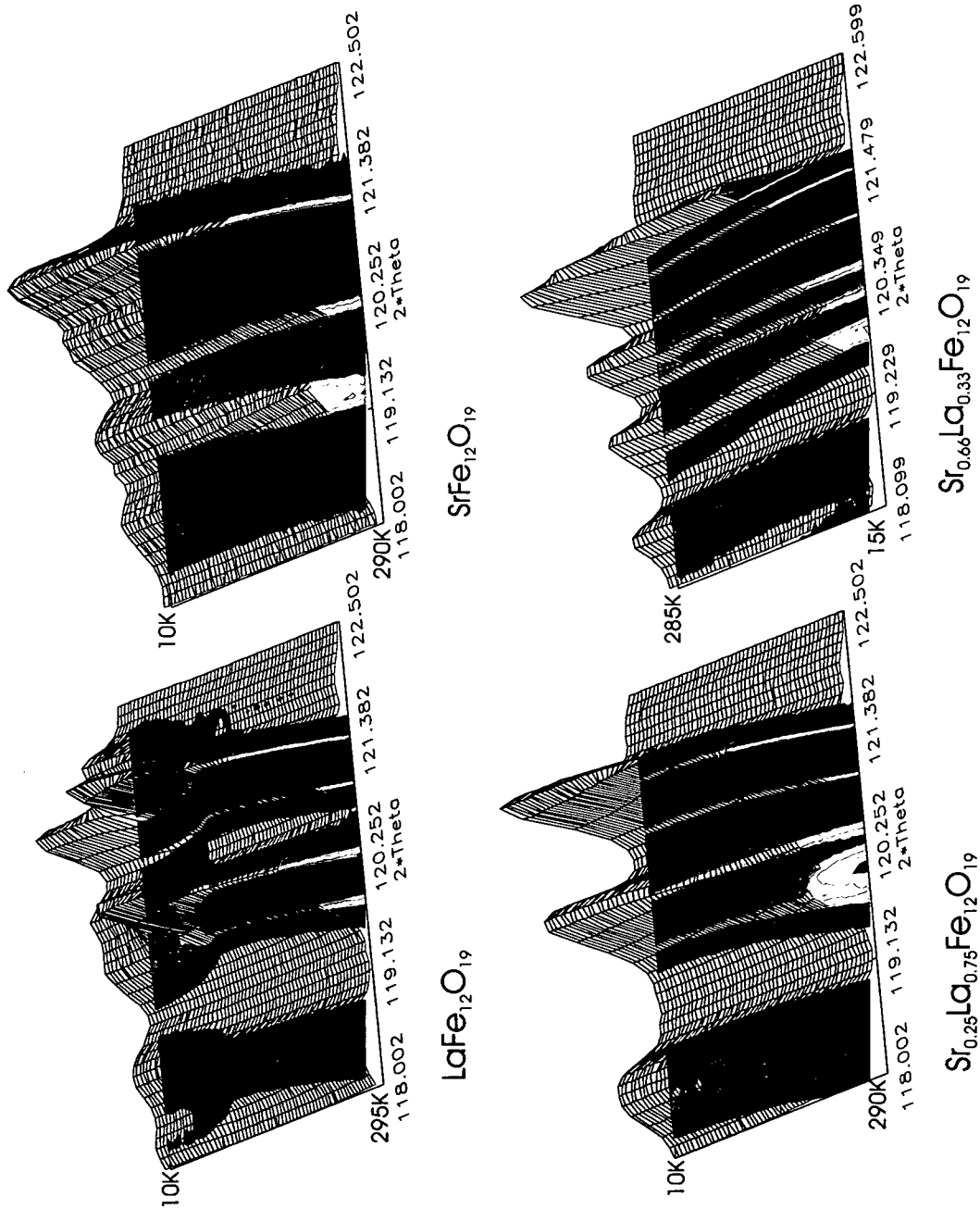


Figure 4.39: Comparison of the peaks showing the phase transition in LaM with partly substituted Sr ferrite and with pure SrM

4.2.2 Electronic properties

Electrical resistance

The electrical resistivity was measured of all La substituted Sr ferrite samples prepared by mechanical alloying. The samples were pressed to cylindrical pellets with a cross section of 1 cm^2 and a height of $2.9 \pm 0.05 \text{ mm}$. Since all samples have almost the same dimensions a comparison of the resistivity is possible. A specific resistivity or a conductivity is not given, since the porosity of the samples, grain boundary influence, impurities and defects in the structure are undetermined. Fig.4.40 shows a measurement in zero magnetic field from room temperature down to app. 30 K. The room temperature resistivity is changing with increasing La concentration from a value of $\text{k}\Omega$ for pure Sr hexaferrite to a few Ω for pure La hexaferrite (see tab.4.8). This corresponds most likely to a gradual change in the energy gap at the Fermi level, since the La ferrite exhibits a much smaller energy gap than the Sr ferrite (see chapter 4.1.2). The Sr ferrite can be fitted with an exponential function, corresponding to a semiconductor like behavior. For all other samples the slope at lower temperatures is lower so that variable range hopping is assumed, like for the pure La ferrite. The measurement exhibits for all La doped samples a hysteresis between cooling down and heating up. It is not yet clear if this is a material property or due to a too fast cooling or heating, which may result in a effective sample temperature higher and lower, respectively, than the one measured. More astonishing is that the values of resistivity at room temperature before and after the measurement do not match. This result has still to be reproduced.

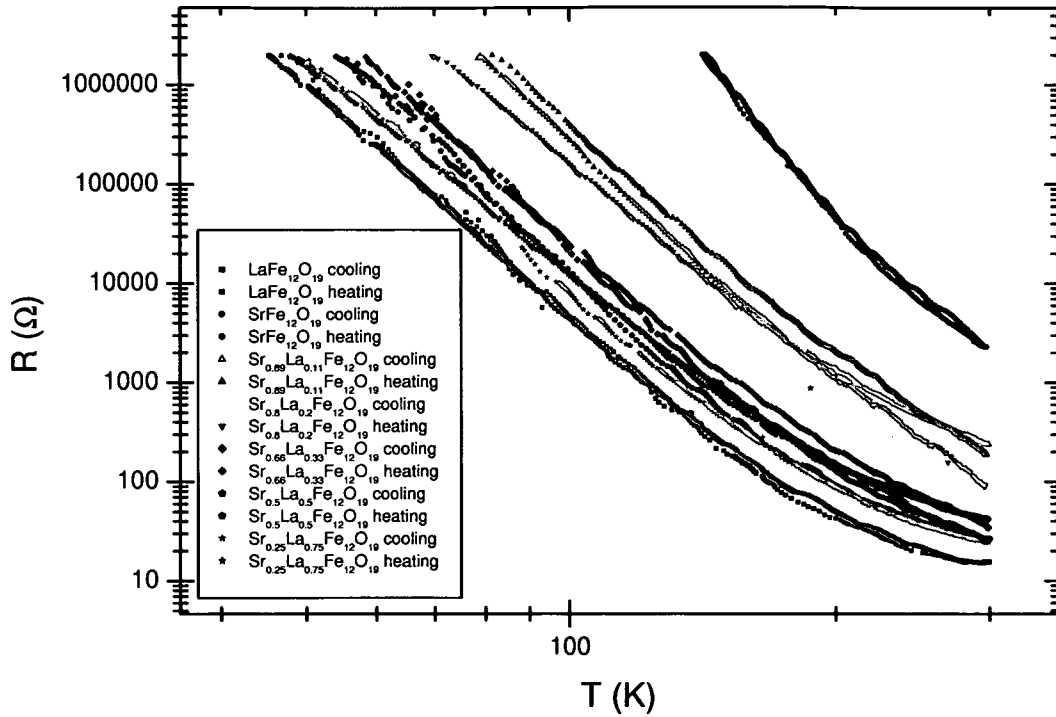


Figure 4.40: Resistivity from room temperature down to 30 K of Sr ferrites substituted with different La concentrations, measured on pressed powder pellets, in logarithmic scale

Table 4.8: Room temperature resistivity pellets of La substituted Sr ferrite with different La concentration

name	R [Ω]
SrM	2306
SrLa8.1	240
SrLa4.1	118
SrLa2.1	42
SrLa1.1	27
SrLa1.3	25
LaM3	16

4.2.3 Magnetic properties

Magnetization

The magnetization of samples prepared with different La concentration by mechanical alloying was measured at room temperature in a pulsed field magnetometer with fields up to 4.9 T (see fig.4.41) and from this the saturation magnetization was calculated. A clear dependence of the magnetization on the concentration could not be observed, but the magnetization decreases with increasing amount of secondary phase (hematite). In fig.4.42 the saturation magnetization from the measured values (squares) are corrected by the amount of secondary phase (circles). The values are scattered with a maximum deviation from the Sr ferrite magnetization of around 5%, which maybe due to errors in the measurement as well as the amount of secondary phases. The temperature dependence of the magnetization was measured

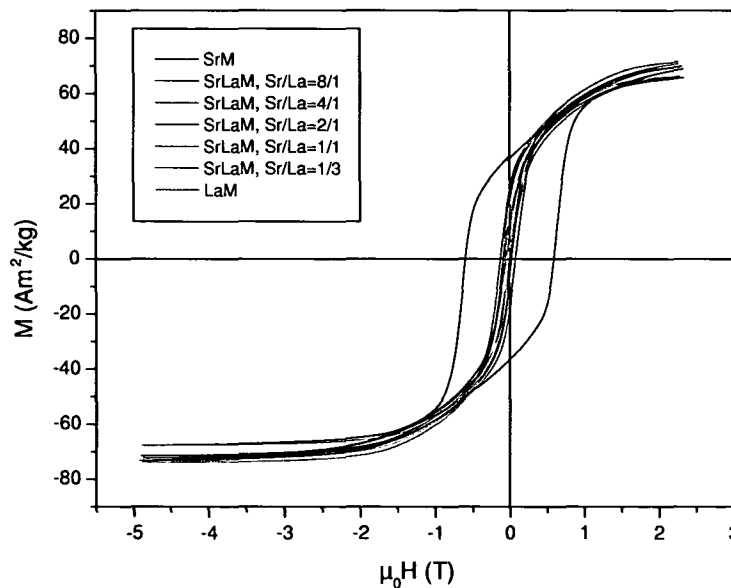


Figure 4.41: Room temperature hysteresis at 4.9 T of La substituted Sr hexaferrite with different La concentrations

in a VSM and in fig.4.43 a comparison between the coprecipitated samples and a Sr ferrite prepared by hydrothermal synthesis is shown. From 4.2 K to room temperature the Sr ferrite exhibits the steepest curve while the La

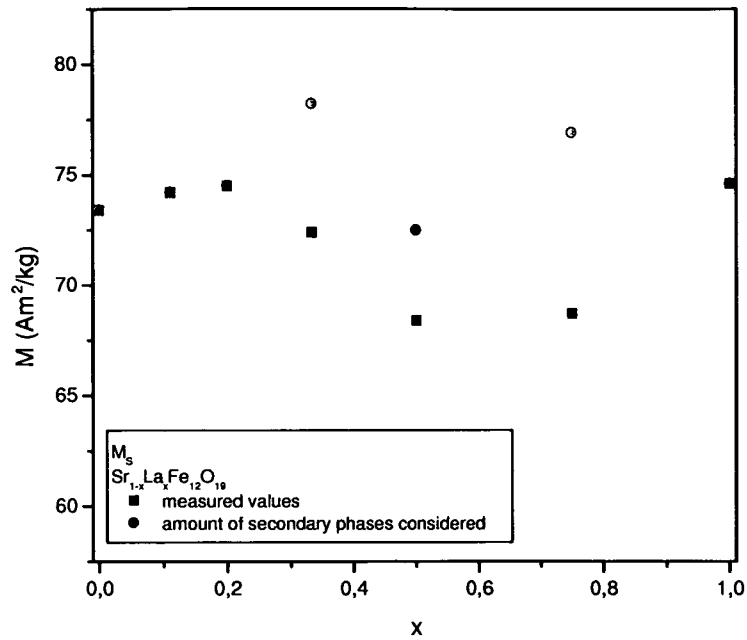


Figure 4.42: Room temperature magnetization at 4.9 T of La substituted Sr hexaferrite with different La concentrations; an amount of secondary phase Fe_2O_3 reduces the magnetization

ferrite decreases slower. Since $M(T)$ is proportional to a superposition of Brioullin functions of the sublattices, this indicates a change in the sublattices, most likely due to the Fe^{2+} , which is different for the pure La ferrite and the partly substituted Sr ferrite. From a low temperature measurement of the hysteresis loop (see chapter 4.2.3) the saturation magnetization of the pure $\text{Sr}_{0.67}\text{La}_{0.33}\text{Fe}_{12}\text{O}_{19}$, corrected for 17% of secondary phases, was estimated to $96.8 \text{ Am}^2/\text{kg}$. Due to Fe^{2+} there should be a change in magnetic moment of $\pm 0.33\mu_B$ per formula unit. Unfortunately the resolution of the measurement is not high enough and the error in the secondary phase amount is too big to allow the determination of this value.

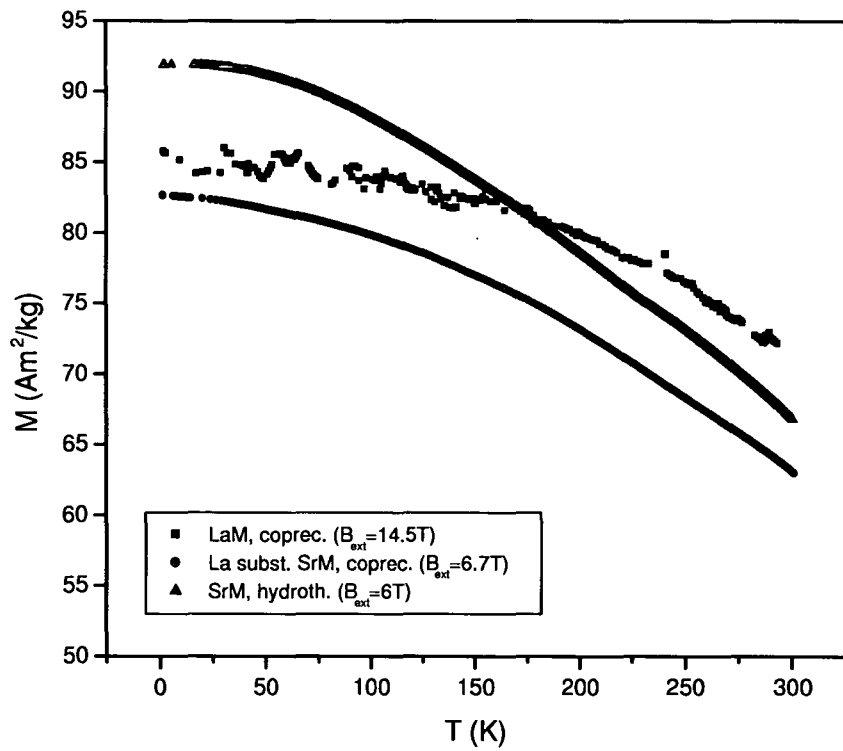


Figure 4.43: Saturation magnetization versus temperature of La substituted Sr hexaferrite (Sr/La=2/1) in comparison with SrM and LaM

Magnetocrystalline anisotropy

In the magnetocrystalline anisotropy a clear dependence on the La concentration is visible. Fig.4.44 shows the anisotropy field versus La concentration as measured by SPD technique at room temperature and at 4.2 K. At room temperature the anisotropy is decreasing almost linearly by 21% at $x=0.5$ and then increasing slightly up to a value of 1.6 T for the La ferrite (Sr ferrite: 1.83 T). There is some uncertainty in comparing the values, due to the demagnetizing field. It was not possible to cut the brittle samples in exactly the same way, so that the demagnetizing field of the slightly different geometries may differ a few percent. At 4.2 K again the anisotropy decreases, but only up to $x=0.33$, and increases then rapidly to reach a value of 3.9 T for the pure La ferrite. From this one can already see that the anisotropy decreases with decreasing temperature for $x=0$ to $x=0.5$ and increases at La concentrations higher than $x \approx 0.6$, where both curves cross.

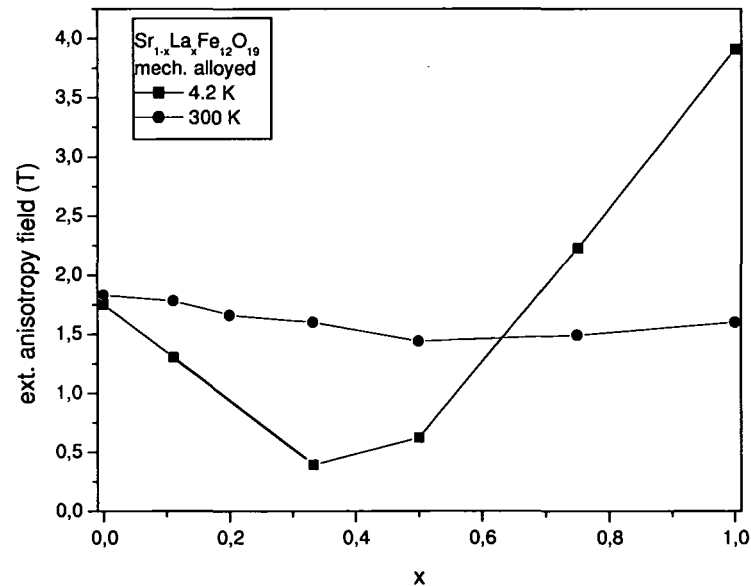


Figure 4.44: Anisotropy field versus La concentration x at 4.2 K and at room temperature

This is better visible in the temperature dependent SPD measurement (see fig.4.45). For all concentrations except $x=0.75$ and $x=1$ the anisotropy

decreases with decreasing temperature. This is rather astonishing, since Lotgering argued for a preference of the Fe^{2+} for the 2a site in La ferrite, where the anisotropy is enhanced. Also in the partly substituted samples some kind of charge compensation has to take place. This can be in form of a localized Fe^{2+} ion and if the reasoning of Lotgering was true, it will only enter the 2a site, where it always enhances the anisotropy. But since the anisotropy is decreased, Fe^{2+} has to enter a site with negative K_1 contribution. Charge compensation is also possible in the form of a delocalized electron. Such an electron could enter the conduction band and increase conductivity of the sample, but it will not change anisotropy much. It may happen that the electron is localized at low temperatures, influencing the anisotropy, and delocalized at room temperature. This picture fits with the electrical resistance of the samples, but is not valid for the pure La ferrite, where the presence of Fe^{2+} at the 2a site at room temperature was confirmed.

The sample with $x=0.75$ shows the same behavior as the pure La ferrite, but a less strong increase in anisotropy. Again a change in slope is visible, for this sample at around 90 K. For the sample with $x=0.2$ only values down to 40 K are shown, below this temperature the SPD peak disappeared. The samples $x=0.33$, coprecipitated, and $x=0.5$, mechanical alloyed, are almost indistinguishable.

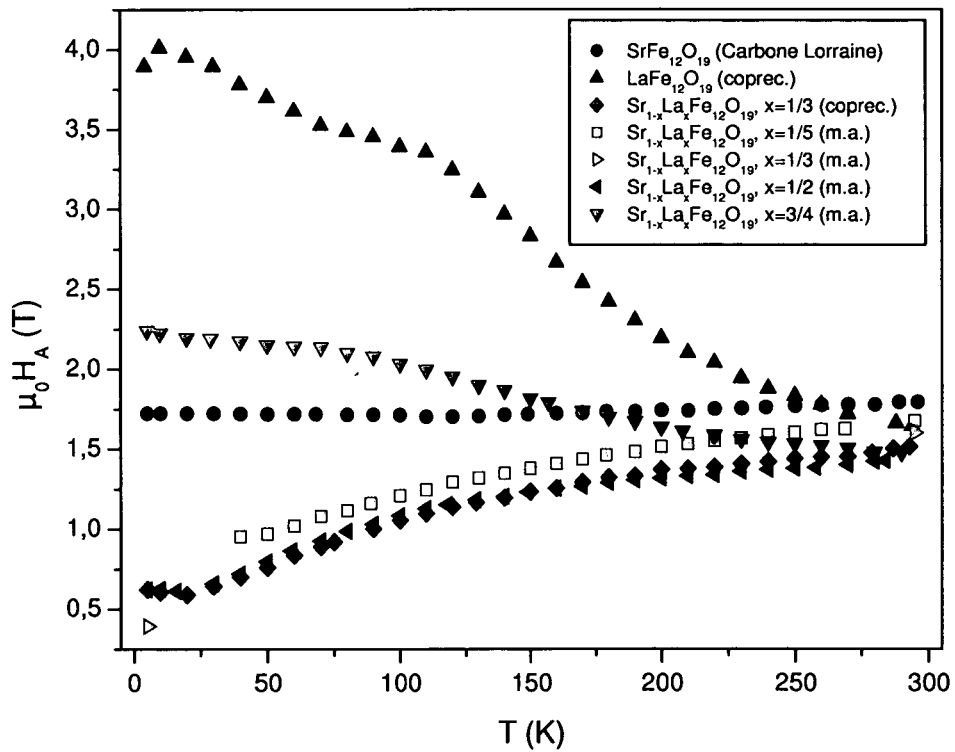


Figure 4.45: Anisotropy field versus temperature of La substituted Sr hexaferrite with different concentrations, prepared by different methods

Hysteresis loop and coercivity

Coercivity measured in a pulsed field magnetometer versus La concentration is shown in fig.4.46. The coercivity decreases with increasing La concentration. The coercivity is determined by two main factors, one is the magnetocrystalline anisotropy, which is an upper limit for the coercivity, the other is the microstructure. In this case the microstructure is dominating the coercivity. As explained in chapter 3.1.1 it is necessary to heat treat the La ferrite at very high temperatures. This supports grain growth and leads to a big difference in coercivity between La hexaferrite and conventional hexaferrites. A heat treatment of the partly substituted samples at lower temperatures results in a higher coercivity, but at the same time it is not sure if the La really enters the hexaferrite structure or forms secondary phases, or defects in the grain boundaries (see chapter 3.1.1). Therefore it is safe to perform a heat treatment also for these samples at high temperatures (1335°C). The result is a strongly reduced coercivity compared with the Sr ferrite, which was heat treated at 1000°C, as shown in fig.4.46. The samples heat treated at the same temperature exhibit a smaller change in coercivity, ranging from 0.1 T at $x=0.11$ to 0.03 T at $x=1$. Although this behavior, decrease down to $x=0.5$ and above slight increase follows the anisotropy, it is expected that this is a microstructural effect as observed in Sm substituted Sr ferrite [82].

The hysteresis loop of the coprecipitated partly with La substituted sample (Sr/La=2/1) was measured at 4.2 K in a VSM, see fig.4.47. The hysteresis loop is much steeper at low fields than in the La hexaferrite and magnetization reaches saturation at much lower fields. This was expected from the measurements of anisotropy field, which is very low for the partly substituted sample. Overall the hysteresis loop resembles the one of Sr hexaferrite. Taking into account the secondary phases of the La samples the measurement delivers similar results for the maximum magnetization of all three samples ($M_S=93.8 \text{ Am}^2/\text{kg}$ for SrM, $M_S=96.9 \text{ Am}^2/\text{kg}$ for $\text{Sr}_{0.67}\text{La}_{0.33}\text{Fe}_{12}\text{O}_{19}$, $M_S=94.8 \text{ Am}^2/\text{kg}$ for LaM).

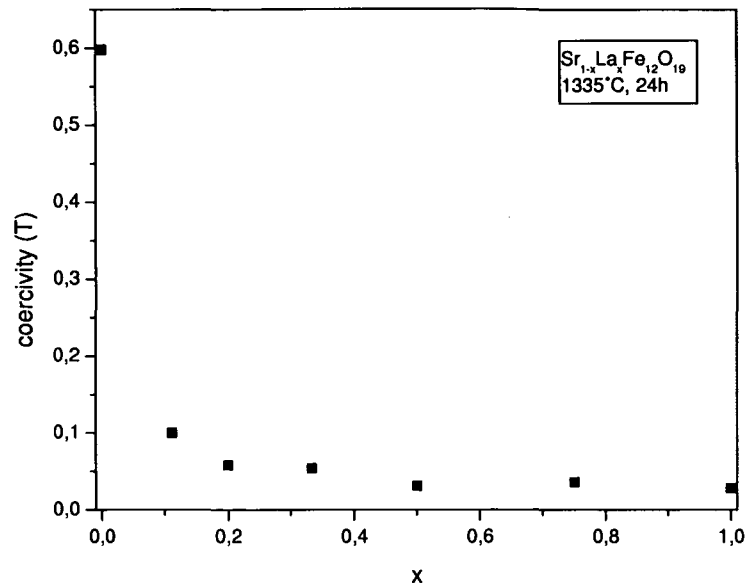


Figure 4.46: Room temperature coercivity at 4.9 T of La substituted Sr hexaferrite with different La concentrations, prepared by mechanical alloying; for the samples heat treated at high temperatures (all except SrM) the coercivity is significantly decreased

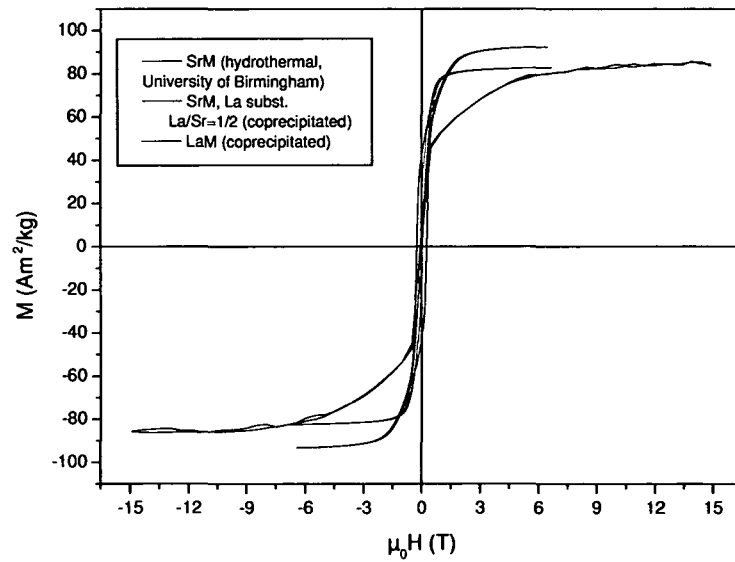


Figure 4.47: Hysteresis loop at 4.2 K of La substituted Sr hexaferrite (Sr/La=2/1) in comparison with SrM and LaM

4.2.4 Local probes

Mössbauer spectroscopy

In order to determine a localization of the Fe^{2+} ion and so to explain the distinct behavior of the anisotropy, the Mössbauer spectrum of the sample $\text{SrLa}_{2.1}\text{Co}$ (coprecipitated sample with $\text{Sr}/\text{La}=2/1$) was measured (see fig.4.48). The spectrum resembles one of pure Sr hexaferrite and no indication for Fe^{2+} was found. Also the hyperfine fields show the typical temperature dependence for all 5 Fe sites, except in temperature range between 160°C and 230°C , where B_{hf} at the 2a site is increased. This may be a sign for problems with the fit. The quadrupol shift shows a positive value for the 2b site, as in Sr hexaferrite. The isomer shift values of all sites are strongly scattered, except for the 12k site.

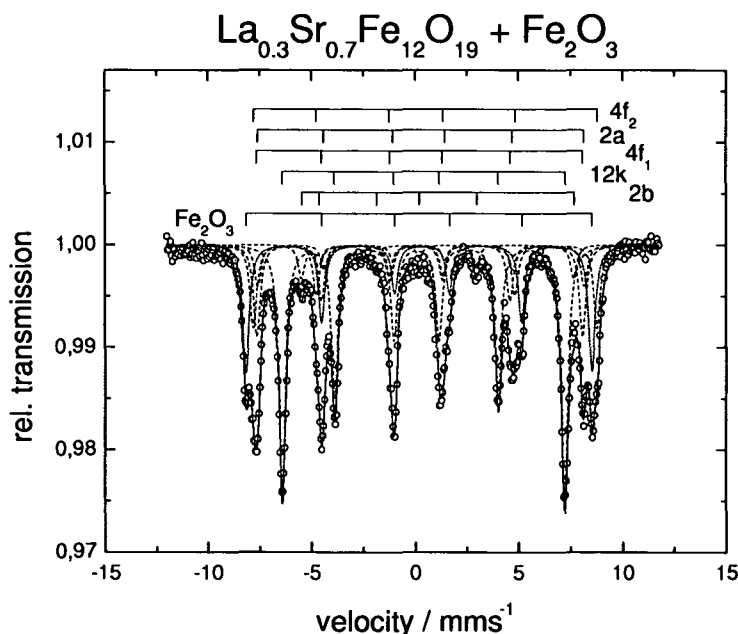


Figure 4.48: Mössbauer spectrum at room temperature of La substituted Sr hexaferrite ($\text{Sr}/\text{La}=2/1$)

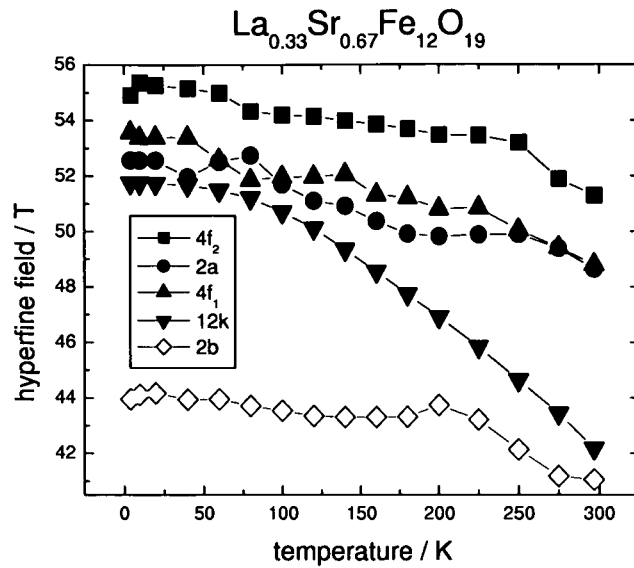


Figure 4.49: Hyperfine field versus temperature of the 5 Fe sublattices in La substituted Sr hexaferrite (Sr/La=2/1) calculated from Mössbauer spectra

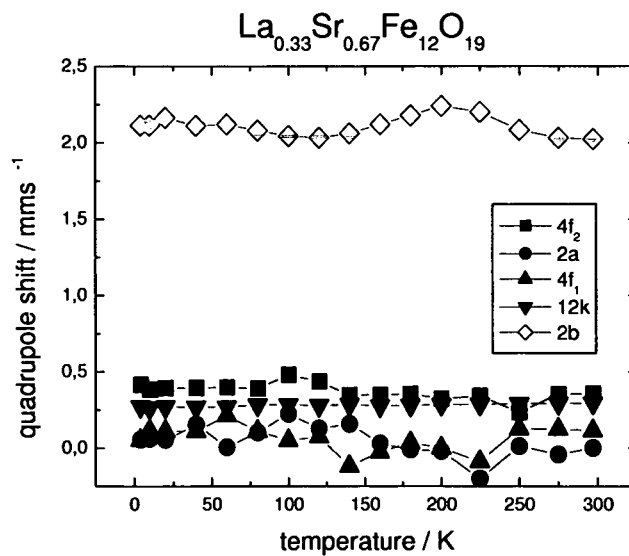


Figure 4.50: Quadrupole shift versus temperature of the 5 Fe sublattices in La substituted Sr hexaferrite (Sr/La=2/1) calculated from Mössbauer spectra

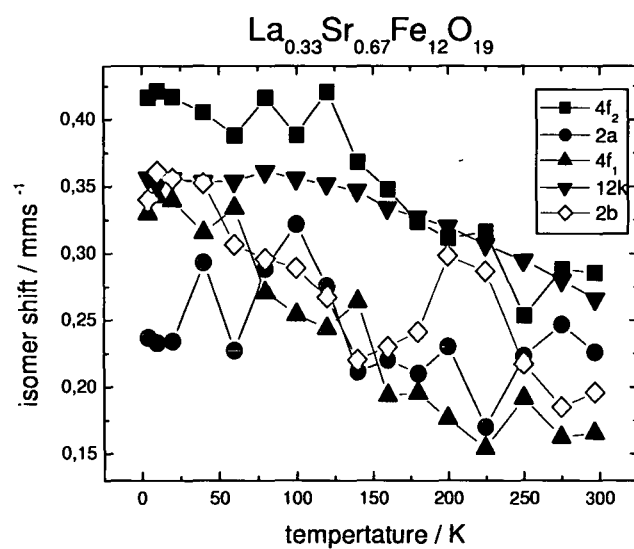


Figure 4.51: Isomer shift versus temperature of the 5 Fe sublattices in La substituted Sr hexaferrite (Sr/La=2/1) calculated from Mössbauer spectra

Nuclear magnetic resonance

Fig.4.52 shows the NMR spectrum of the La substituted Sr hexaferrite with $\text{La/Sr}=1/2$ in comparison with pure Sr and pure La hexaferrite. Between 70 MHz and 76 MHz 7 peaks are visible in this structure. 12k, 4f1 and 4f2 show satellite peaks, while 2a is shifted to lower frequencies. By measuring in an external field (see fig.4.53) the satellites were assigned to the main peaks, showing a positive slope, like for 4f1 and 4f2, or a negative slope, like for 12k. These satellites are due to different local environments of the Fe ions, caused by the partly substitution. While the main part of the 12k peak is unchanged, the 4f2 shows a strong splitting in two almost equivalent peaks and a slight shoulder at the right. This can be explained having a look at the crystal structure (see chapter 2.2.1). The 4f2 site is very close to the Sr site and has 3 Sr ions as neighbors. Some of these Fe ions will find no La ion as neighbor, some one and some two. The intensity of the peaks is proportional to the probability to find a certain number of La ions in the neighborhood. The 12k site is in between the layer that contains the Sr ion and the 2a site, which is strongly influenced by the La substitution. Therefore the 12k peak shows only slight changes. The 2a peak, which is shifted significantly to lower frequencies in the La hexaferrite, occurs in the partly substituted sample at only slightly lower frequency and vanishes above $x=0.5$.

Fig.4.54 shows zero field spectra of samples prepared by mechanical alloying with different La concentrations. At the small concentration $\text{La/Sr}=1/8$ the spectrum resembles the one of pure SrM. All 4 peaks of the sites 12k, 4f1, 2a and 4f2 are present, but already the satellites of 4f1 and 4f2 occur. The 2a peak is shifted to lower frequencies. With increasing concentration the satellites grow and the peaks 4f1, 4f2 and 2a are shifted to lower frequencies, at $\text{La/Sr}=1/1$ 2a vanished and 4f2 appears as a broad hump. In the pure LaM the 2a peak is shifted out of the frequency range shown and 4f2 occurs again as a sharp peak. At higher concentrations also the 4f1 and its satellite move closer to a broad hump, with an intensity higher than the remainder of the unperturbed 12k site. The strongest change occurs at least at small concentrations at the 4f1 site, which leads to the assumption that this may be the preferred site for the Fe^{2+} ion. The 4f1 site has tetrahedral

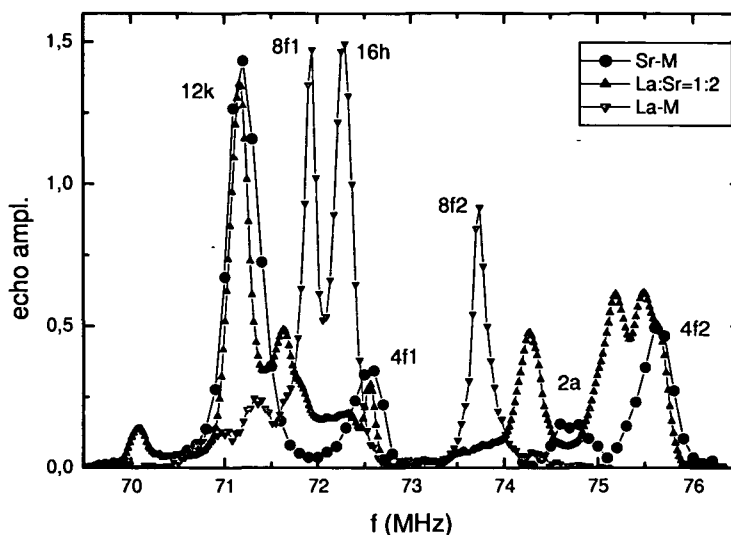


Figure 4.52: Pointwise Fourier transformed NMR spectrum of La substituted Sr hexaferrite (Sr/La=2/1) in comparison with Sr ferrite (sintered) and La ferrite

coordination, therefore the affect on the anisotropy of the orbital momentum of Fe^{2+} will be very different than at octahedral site (see chapter 2.1.3), and could explain the decrease in anisotropy with decreasing temperature. At a certain concentration the additional electron changes from the 4f1 site to the 2a site, which is nearby in the crystal lattice, and increases the anisotropy with decreasing temperature, like in the pure LaM. This configuration seems not to be stable so that a distortion of the lattice occurs.

The La resonance is very different compared to the one in pure La hexaferrite. A broad hump appears due to a distribution of electrical field gradients and internal magnetic fields. The curve should be symmetric, but because of the amplification factor, which is reciprocally proportional to the field, the intensities are smaller at higher fields. This can be corrected by multiplying with the field and then a maximum can be determined. From this the transferred hyperfine field can be estimated to 2.75 T.

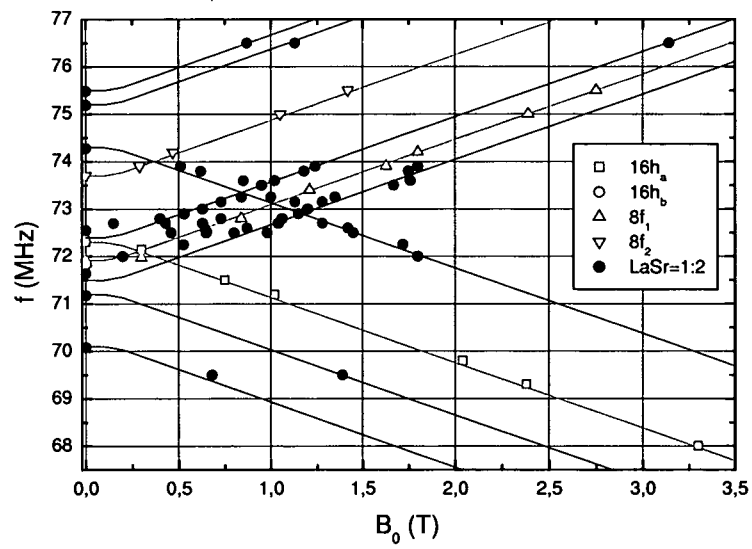


Figure 4.53: Shift of Fe resonance with an external field

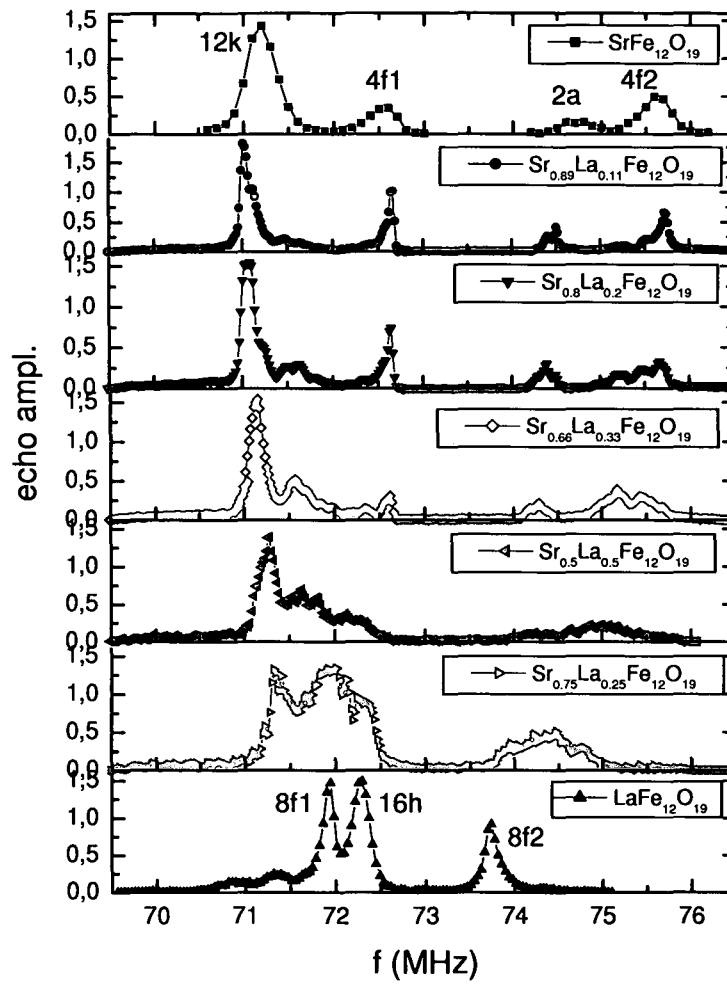


Figure 4.54: NMR spectra of La substituted Sr hexaferrite with various La concentrations, prepared by mechanical alloying, in comparison with Sr ferrite (sintered)

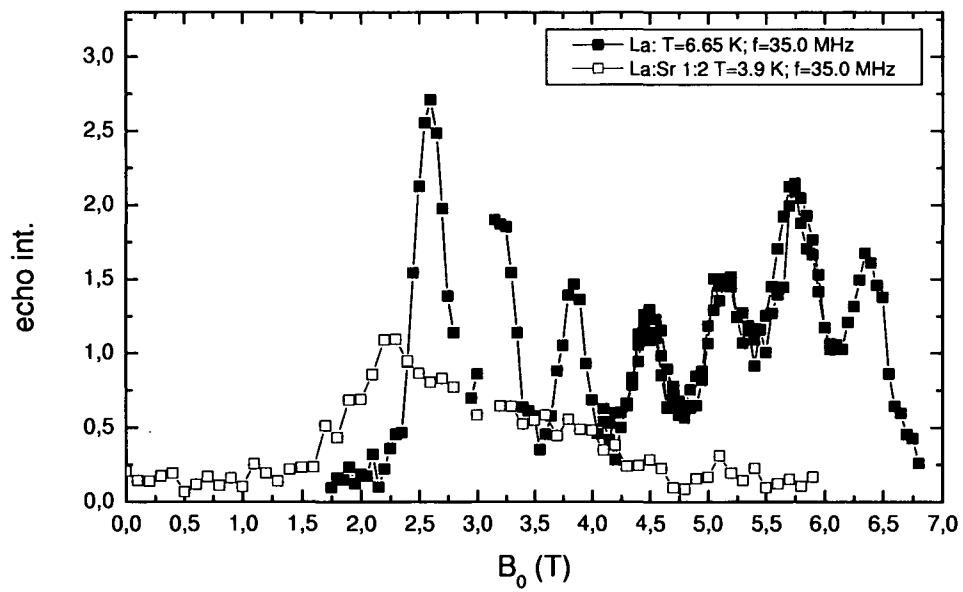


Figure 4.55: La resonance of La substituted Sr hexaferrite (Sr/La=2/1) in comparison with La ferrite

4.3 Rare earth substituted Sr hexaferrite

This chapter includes investigation of Sr hexaferrite samples of the type $\text{Sr}_{1-x}\text{RE}_x\text{Fe}_{12}\text{O}_{19}$, substituted with 4 different rare earth elements, RE=La, Sm, Nd, Pr in different nominal concentrations, $x=0.04, 0.048, 0.059, 0.111, 0.2, 0.333$, equal to ratios RE/Sr=1/24, 1/20, 1/16, 1/8, 1/4, 1/2. All samples were prepared by hydrothermal synthesis at the University of Birmingham, including a structural characterization by XRD and SEM. Magnetic properties were mainly investigated in Vienna, including Mössbauer studies and NMR. These samples are interesting because, besides the effect of the different valence of the rare earth compared with Sr which leads to changes in magnetic behavior due to the Fe^{2+} ion, the rare earth element itself, except La, may develop an orbital momentum, giving a contribution to magnetocrystalline anisotropy.

4.3.1 Structural properties

X-ray diffraction

XRD was performed at the University of Birmingham using Cu $K\alpha$ radiation with 40kV and 50mA[9]. For all samples an increasing amount of secondary phases with increasing RE concentration was observed. The secondary phases were mainly Fe_2O_3 , present in all 4 sample series, Nd_2O_3 in the Nd series [9], $(\text{Sr,Sm})\text{FeO}_{3-\delta}$ in the Sm series [8, 82], LaFeO_3 in La series [10]. It was possible to reduce the amount of secondary phases by increasing the temperature for calcination. For concentration RE/Sr<1/4 above 1100°C a negligible amount was found. For higher concentrations it was necessary to increase the calcination temperature more, 1250°C were necessary to obtain single phase samples. The RE concentration had in all cases almost no influence on the lattice parameters, which is shown on the example of Sm (see tab.4.9).

Microstructure

SEM studies indicated that platelet structure was obtained for all samples. The grain size was independent of the RE earth concentration but, strongly

Table 4.9: Lattice parameters of Sm substituted Sr hexaferrites

Sm concentration	c [10^{-10}]	a [10^{-10}]
Sm/Sr=0	23.027	5.882
Sm/Sr=1/16	23.016	5.878
Sm/Sr=1/8	23.017	5.877
Sm/Sr=1/4	23.031	5.882
Sm/Sr=1/2	23.013	5.879

correlated with the secondary phases. For example in the Nd series a mixture of small and large particles was found for higher RE concentrations, with increasing proportion of small particles with increasing Nd/Sr ratio [9]. For Sm substituted Sr hexaferrite the particle size was determined to be about 1.5-1.6 μm and the size showed no increase with the calcination temperature. For small Sm/Sr ratios the grain size even decreased with increasing temperature, probably due to an grain growth inhibiting effect of the secondary phase SrFeO_{3-x} . Also for the Sm series a decreased grain size with increasing Sm concentration was observed [8].

4.3.2 Magnetic properties

Magnetization

Fig.4.56 shows magnetization measured at 1100kA/m at room temperature versus RE concentration for the series Sm, La and Nd and remanence for the Sm series [13]. These first measurements of magnetic properties were performed at the University of Birmingham and show a slight decrease of magnetization with increasing RE concentration. This decrease may be attributed to a small amount of non magnetic secondary phases in the samples. The remanence shows a broad maximum, but decreases at higher concentrations, too.

The hysteresis loop at 4.2 K was then measured at a VSM at the Vienna University of Technology. Fig.4.57 shows measurements of all samples with highest RE concentration, RE/Sr=1/4 (and La/Sr=1/2). For all samples

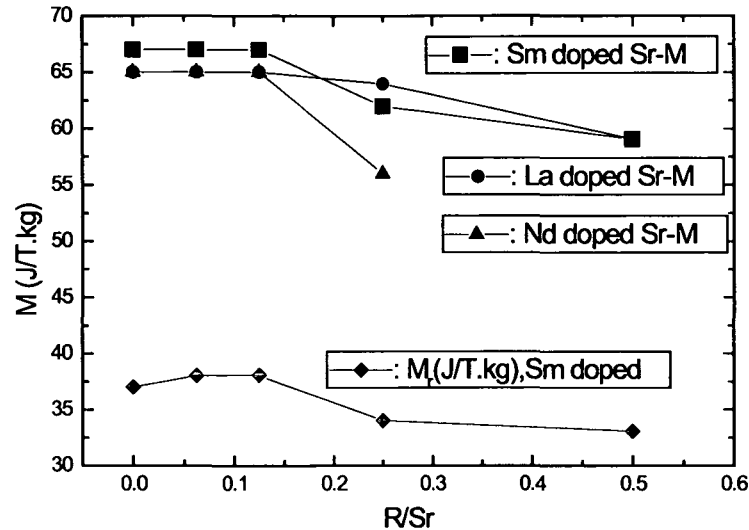


Figure 4.56: Magnetization and remanence at room temperature of RE substituted Sr hexaferrite samples, with RE=Sm, La, Nd [13]

the magnetization decreases compared with the pure Sr ferrite, in the worst case the decrease is 10% for La/Sr=1/2. As explained in the chapter 4.1 a slight decrease is expected due to the Fe^{2+} ion, which has a smaller magnetic moment. But for this reason we expect only an decrease of $0.3\mu_B$ per formula unit, equal to 1.5%. Whereas in the case of the formation of secondary phases the decrease can be much higher. Assuming that no La enters the hexaferrite structure, but forms a non magnetic secondary phase, with a formula weight of 1/3 of the Sr ferrite, the magnetization will be reduced by 10%. A secondary phase with a formula weight of 1/4 of SrM (moleweight 1061.8 g) is e.g. LaFeO_3 (moleweight 242.45 g), which is one of the possible secondary phases. Another indication that the rare earth element did not enter the hexaferrite structure is a measurement of magnetization versus temperature, shown in fig.4.58. While the coprecipitated samples (see chapter 4.2.3) show a deviation from the pure Sr hexaferrite, all samples prepared by hydrothermal synthesis follow exactly the Sr hexaferrite behavior. In the inset of fig.4.58 the difference between the magnetization signal of the RE substituted Sr ferrite and the pure Sr ferrite is shown. For all samples the curve is almost constant and shows a deviation of up to 10% for the sample

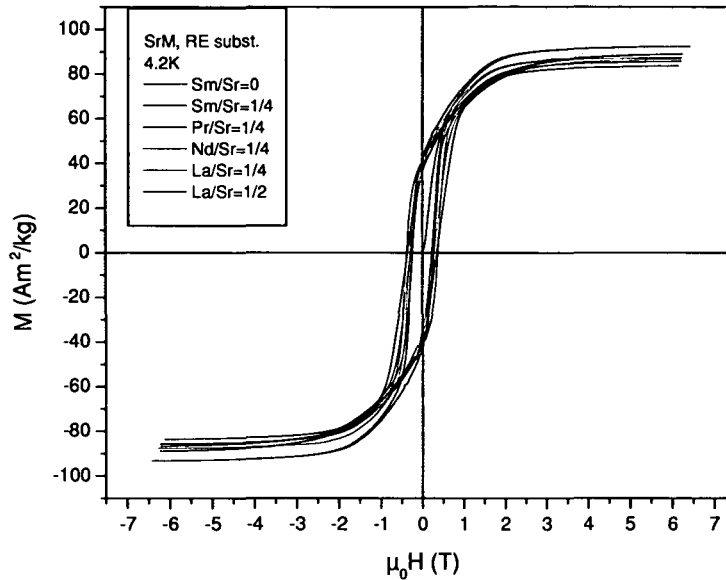


Figure 4.57: Comparison of hysteresis loop at 4.2 K of RE substituted Sr hexaferrite samples, with RE=Sm, La, Nd, Pr; the measurement was performed in a vibrating sample magnetometer with a maximum field of 7 T and a frequency of 81 Hz

with the highest RE concentration. In order to clarify, if secondary phases are present in the sample, a second XRD was performed for the sample with La/Sr=1/2. The results of the analysis are shown in tab.4.10. A total amount of 13% of secondary phases was found, which explains the decrease in magnetization. Also the lattice parameters indicate clearly that only SrM is present in this sample, without La entering the lattice. It is not clear, why first measurements showed single phase samples, since it is not likely that the sample decomposes with time, since hexaferrites are chemically very stable. On the other hand, since the rare earth substituted phase is metastable at room temperature, it cannot be completely excluded. Most probable is the explanation that the first XRD measurements were performed for a different charge of samples, and maybe slight differences in preparation lead to the amount of secondary phases.

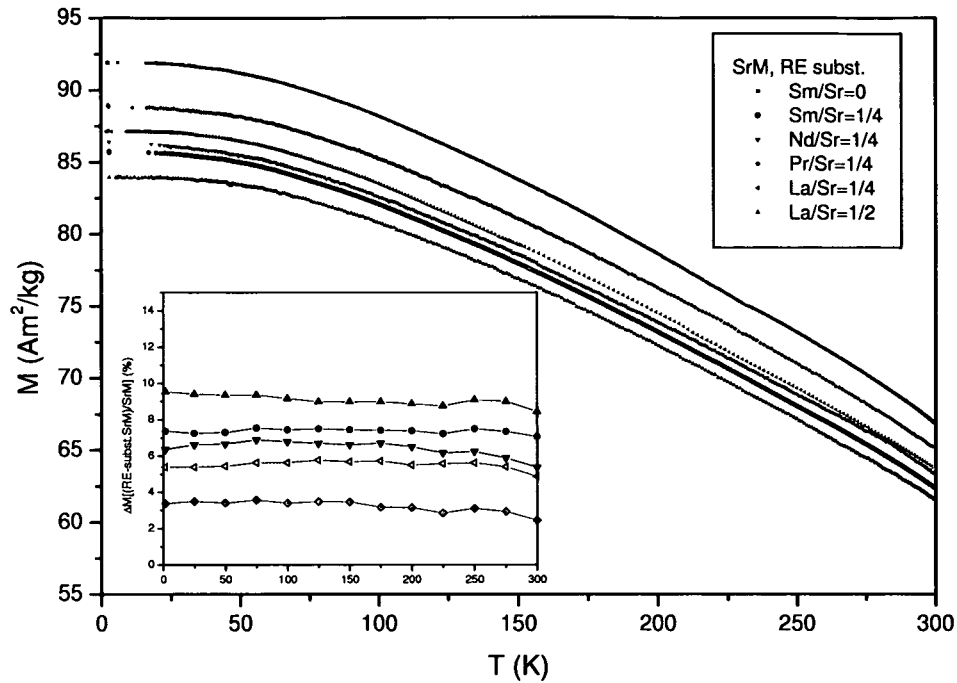


Figure 4.58: Magnetization versus temperature at 6.9 T of RE substituted Sr hexaferrite samples, with RE=Sm, La, Nd, Pr

Table 4.10: XRD analysis performed with Topas of a La substituted Sr hexaferrite with La/Sr=1/2; lattice parameters and secondary phases are shown

u.c. volume [10^{-30}]	c [10^{-10}]	a [10^{-10}]	Fe ₂ O ₃ [%]	LaFeO ₃ [%]
690.45	23.028	5.884	3.4	10

Magnetocrystalline anisotropy

In contrast to the samples with La-Co substitutions (see chapter 2.2.3) the RE substituted samples also did not exhibit a strong increase in anisotropy with the RE concentration (see fig.4.59). The most promising result was found for Pr, with a by 10% increased anisotropy field, still half of the value that can be reached with La-Co substitutions. Also no significant deviation

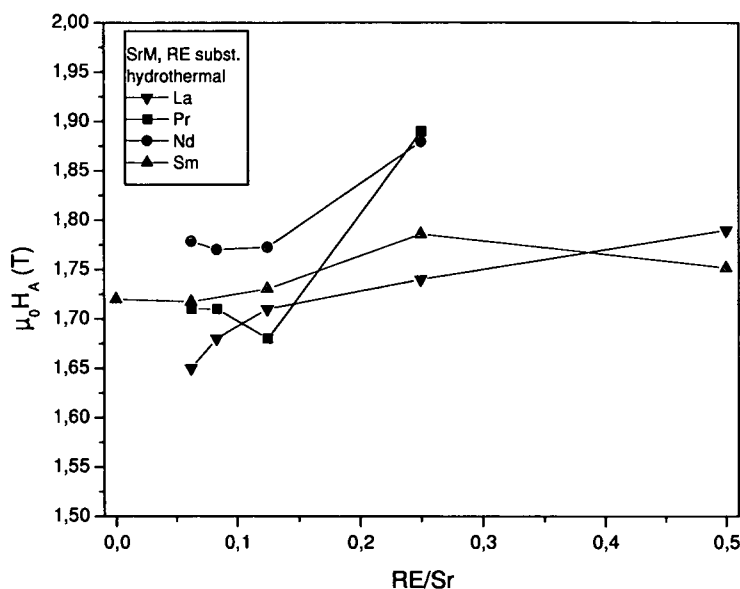


Figure 4.59: Comparison of anisotropy field at room temperature of RE substituted Sr hexaferrite samples, with RE=Sm, La, Nd, Pr and concentrations up to RE/Sr=1/2; the measurement was performed in a pulsed field magnetometer with a maximum field of 8 T and a pulse duration of 2 ms (half wave), using the SPD technique

from the conventional Sr ferrite was found in the anisotropy field versus temperature (see fig.4.60). At low temperatures a potential orbital momentum or a contribution of the momentum of the rare earth element should be apparent. Only the Nd substituted sample showed a hump in magnetocrystalline anisotropy at around 25 K, but overall the increase is still small. This result is especially astonishing for the La substituted sample, since the sample with the same concentration prepared by coprecipitation and mechanical alloying showed completely different behavior. In comparison with the coprecipitated

sample the hydrothermally prepared resembles the pure Sr ferrite, as shown in fig.4.61. This is again an indication that with hydrothermal synthesis the rare earth element does not enter the hexaferrite structure, and therefore only the Sr ferrite signal is measured.

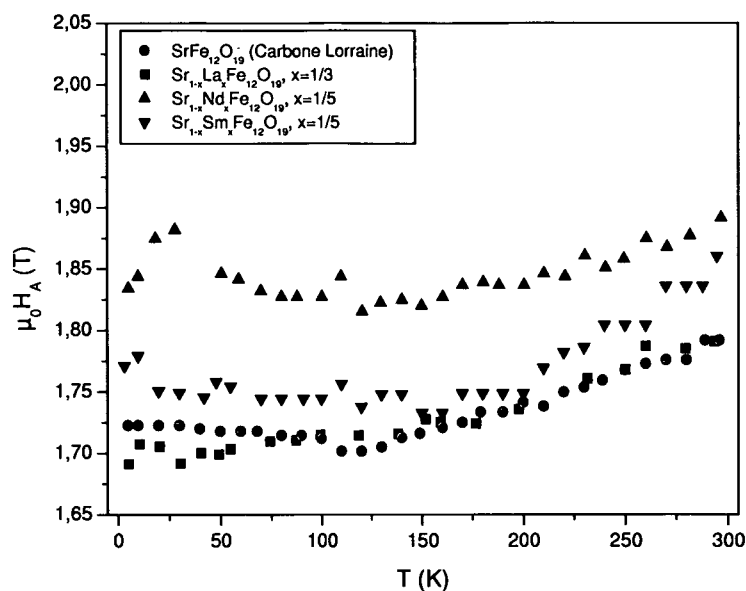


Figure 4.60: Comparison of anisotropy field from room temperature down to 4.2 K of RE substituted Sr hexaferrite samples, with RE=Sm, La, Nd and concentrations of max. anisotropy at room temperature; the measurement was performed in a pulsed field magnetometer with a maximum field of 8 T and a pulse duration of 2 ms (half wave), using the SPD technique

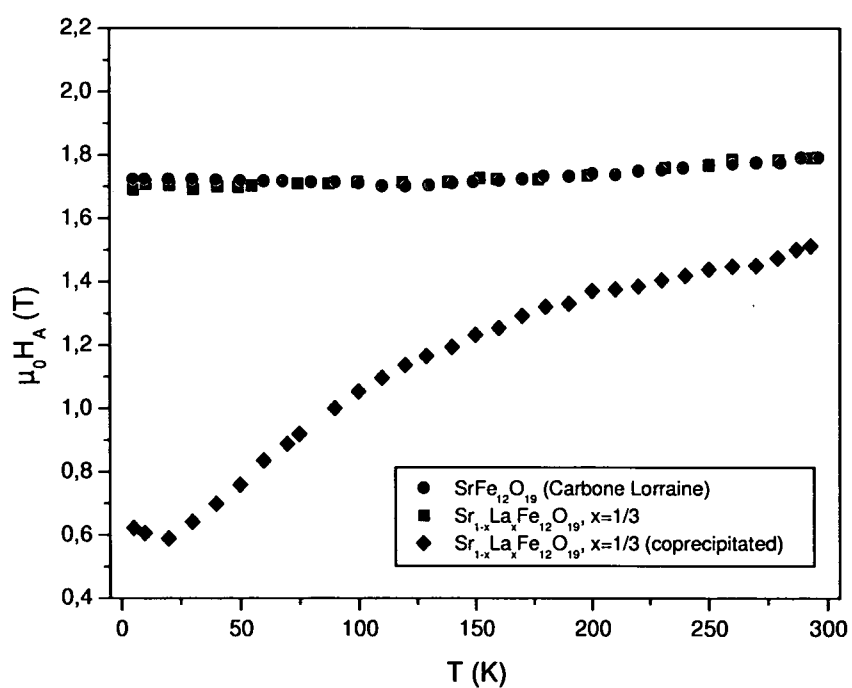


Figure 4.61: Comparison of anisotropy field from room temperature down to 4.2 K of La substituted Sr hexaferrite samples, with Sr/La=2/1, prepared by hydrothermal synthesis and coprecipitation

Hysteresis loop and coercivity

Although the magnetocrystalline anisotropy does not change drastically the coercivity always shows a maximum with respect to the RE concentration [13]. As example the measurement of the Nd series is shown in fig.4.62. It was found that the main factor for this behavior is the microstructure, exhibiting smaller grains at a certain RE concentration depending on the RE element (see chapter 4.3.1).

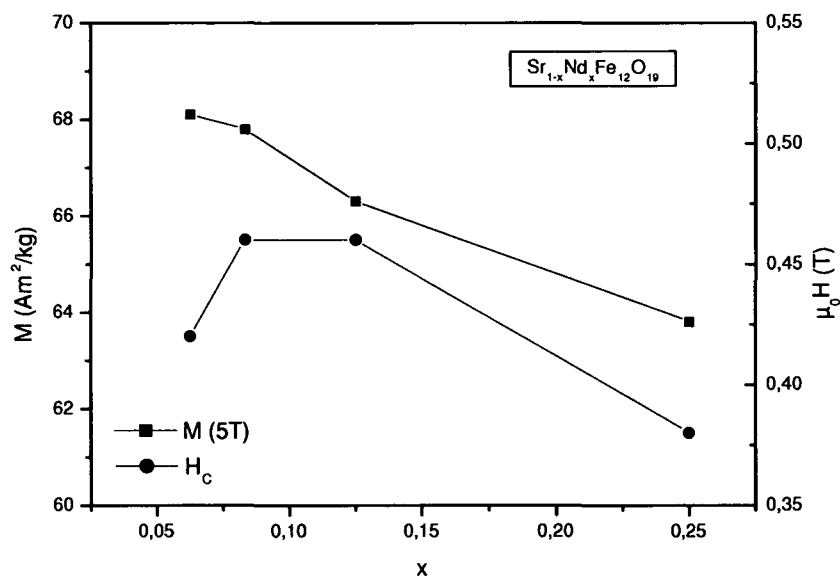


Figure 4.62: Coercivity and magnetization at 5 T of Nd substituted Sr ferrite with different concentration

4.3.3 Local probes

Mössbauer spectroscopy

Mössbauer measurements were performed for the Sm series [83]. The effect of the Sm substitution on the hyperfine parameters is close to the resolution of the experiment, showing again almost no deviation from the parent compound (see fig.4.63). A slight increase of Curie temperature was found

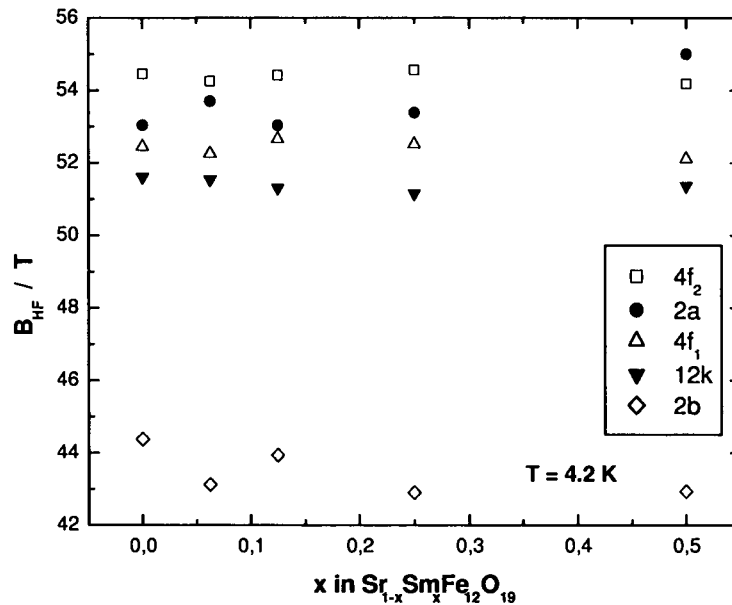


Figure 4.63: Hyperfine field versus Sm concentration at 4.2 T calculated from Mössbauer spectra [83]

with temperature dependent Mössbauer measurements, which can be taken as indication, that the Sm substitution gives a contribution to the magnetic exchange. At room temperature, where the resolution is best, a slightly broadened doublet was observed, with a negative isomer shift. This usually indicates a phase with metallic character, which could be $\text{SmFeO}_{3-\delta}$, found in these samples [8]. Overall the spectra of pure and with Sm substituted Sr ferrite are almost equivalent (see fig.4.64 and 4.65). No indication for Fe^{2+} was found. This can be taken as a hint that the Sm does not enter the hexaferrite. On the other hand it is also possible that the Sm/Sr ion has no influence on the Fe sites, which have predominantly oxygen and iron ions in

their local environment. A similar result was found for the coprecipitated sample (see chapter 4.2.4).

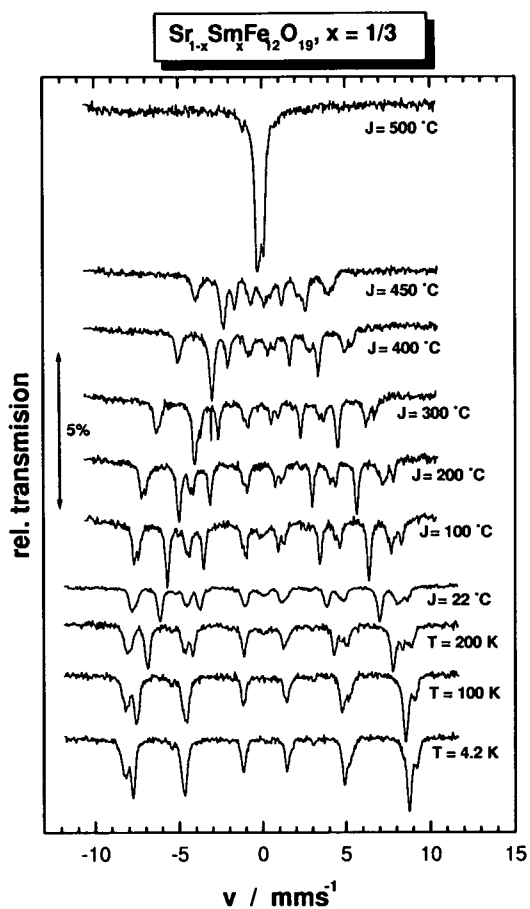


Figure 4.64: Change of Mössbauer spectra with temperature of Sm substituted Sr ferrite, with Sm/Sr=1/2 [83]

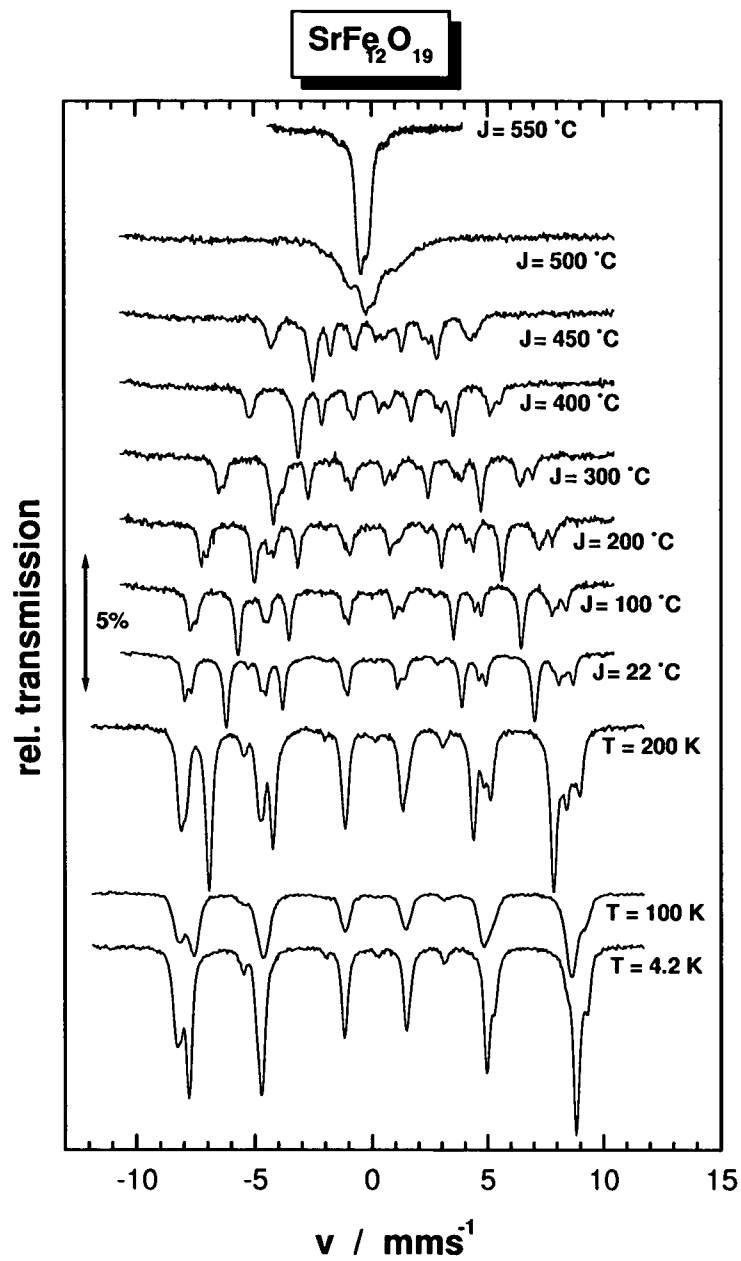


Figure 4.65: Change of Mössbauer spectra with temperature of Sr ferrite [83]

Nuclear magnetic resonance

In contrast to the Mössbauer measurements a clear deviation from the parent compound was found with NMR for small RE concentrations. Fig.4.66 shows the change of the NMR spectra with concentration using as example the La series. A shift of all Fe lines is visible at small concentrations while at higher La concentrations the spectrum is almost indistinguishable from Sr ferrite. Lines belonging to the spin down sites 4f1 and 4f2 are shifted to lower frequencies, while lines of the spin up sites 12k and 2a, but also 2b, which is not shown in the figure, shift to higher frequencies. This was observed by measurements in an external magnetic field (see fig.4.67), which shifts the lines in the opposite directions. At 0.4 T the spectrum of the La/Sr=1/16 sample and the one of Sr ferrite are identical. This means the presence of an additional hyperfine field of 0.4 T in the sample. This value holds for all iron sites except 2b, where the measurement delivered 0.25 T. The shift appeared for all rare earth elements used for substitution (see fig.4.68).

This shift was explained by the formation of a large polaron due to the additional electron present in the sample, because of the 3+ valence of the rare earth element [84]. This additional electron, in the sample with RE/Sr=1/16 only one in every eight unit cell, influences all Fe sites and causes an additional hyperfine field. This can be interpreted in a rigid band model, where the in SrM empty minority bands are filled with the additional electron. The minority states of 4f1 and 4f2 are parallel to the magnetization, while the minority states of 12k, 2b and 2a are antiparallel. Therefore, assuming negative hyperfine coupling, the additional hyperfine field would be derived from the 4f sites. For higher concentrations the overlap of bands and the filling of the majority band may compensate the polarization of the polaron. In view of the results discussed above it is, however, more probable that it is not possible to prepare samples with higher concentrations with this preparation method. Instead, the changes in the preparation procedure for larger concentrations may lead to the formation of pure SrM, so that the spectrum of the pure hexaferrite was observed.

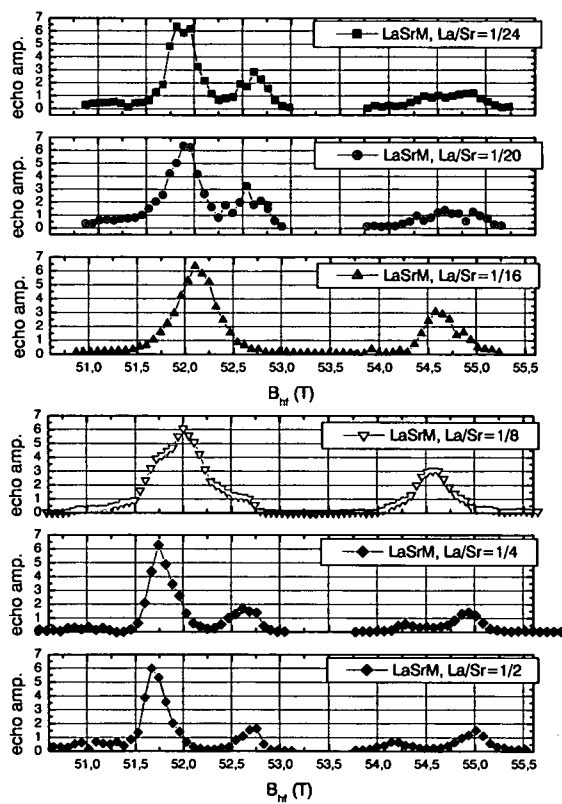


Figure 4.66: Shift of lines in NMR spectrum of La substituted Sr ferrite

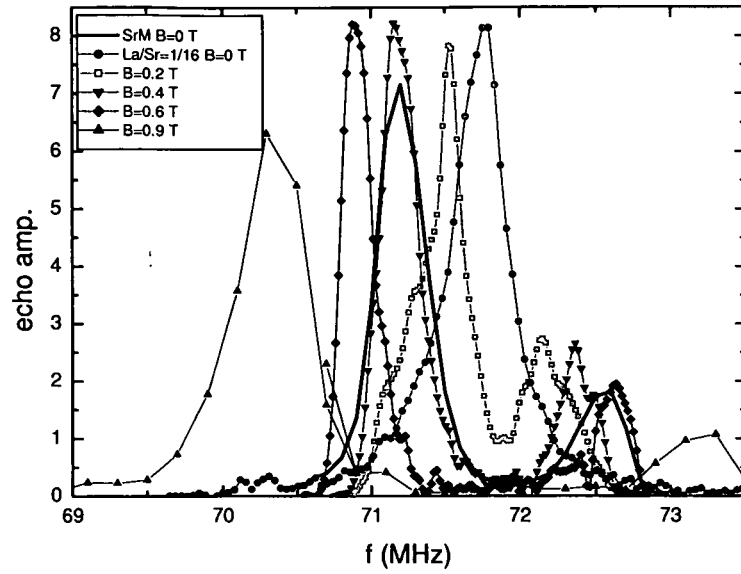


Figure 4.67: Shift of lines in NMR spectrum of La substituted Sr ferrite with an external field

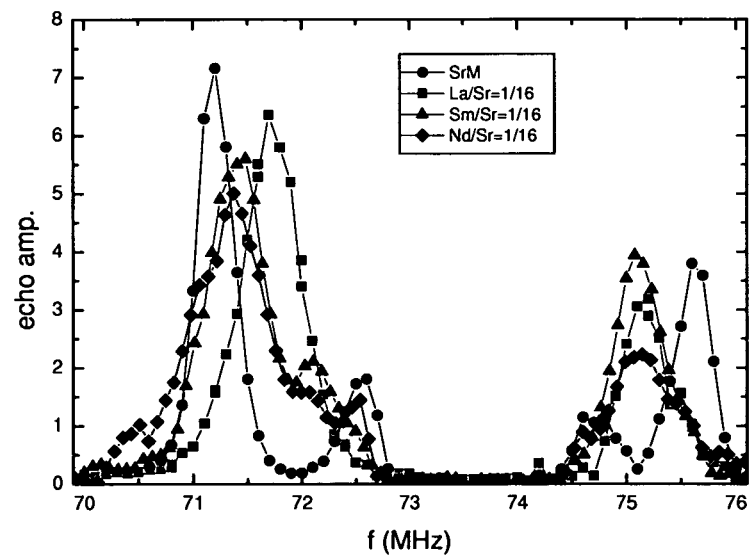


Figure 4.68: Shift of lines in NMR spectrum of different RE substituted Sr ferrite

Chapter 5

Electron structure calculations

5.1 Introduction

Electron structure calculations were performed in collaboration with the Institute of Physics of ASCR in Prague, Czech Republic. This was started with the aim to calculate the anisotropy contributions of the five Fe sites. As pointed out in chapter 2.2, the origin of the anisotropy in the M-type hexaferrite is not yet clarified. Therefore electron structure calculations could provide important information, but until recently these calculations were not possible for unit cells as large as the magnetoplumbite one, since they were restricted by the computational facilities. With the use of workstations and reliable software based on the density functional theory the situation improved, and few papers on this topic were published [46, 85], showing also the viability of calculating anisotropy in this compound.

First calculations were performed for $\text{Sr}_{1-x}\text{La}_x\text{Fe}_{12}\text{O}_{19}$ with La concentrations of $x=0, 0.25, 0.5, 0.75, 1$ and had the aim to investigate how electronic structure and magnetism develop with the La concentration. For all concentrations, including $x=1$, the unit cell $\text{P6}_3/\text{mmc}$ with Gorter spin structure was assumed. This is only a rough approximation for the pure La ferrite, since the calculations are performed at 0 K, and the La ferrite exhibits a lattice distortion below 110 K, as was found out later. In subsequent calculations LS coupling was added in order to achieve results about magnetocrystalline anisotropy, and a similar procedure was done for the distorted crystal lattice

with the CmCm spacegroup. These calculations are still in progress and did not yet yield results in good agreement with the experiment.

5.2 Calculation method

For the calculations of the electronic structure of M-type hexaferrite the WIEN2k program [86] was employed, which was developed at Vienna University of Technology. This program is based on the density functional theory and it uses the full-potential linearized augmented plane wave (FPLAPW) method with the dual basis set (see chapter 2.1.6). In the APW-like methods the space is divided into non overlapping atomic spheres and the interstitial region. The electron states are classified into core states which are fully contained in the atomic spheres, and valence states. The valence states are expanded using atomic-like basis functions in the spheres augmented by plane waves in the interstitial region. So called local orbitals are added to these basis functions to treat two valence functions with the same orbital number (like $3p$ and $4p$ functions of Fe) [87]. The $3p, 3d, 4s, 4p$ states of Fe, $2s, 2p, 3s$ of O, $4s, 4p, 4d, 5s, 5p$ of Sr, and $5s, 5p, 5d, 6s, 6p, 6d$ states of La were treated as valence states. The radii of the atomic spheres were 2.00 for La and Sr, 1.9 for all five inequivalent Fe and 1.6 a.u. for the oxygen. The leakage of the core states can be safely neglected so the outer ten (eleven) electrons of Sr (La) are placed on valence states which differ only in their main quantum number. They are responsible for the change of the density as the La concentration is increased. Charge or spin counts on individual atoms depend to some extent on the size of the atomic spheres.

The maximum orbital number for the basis functions in the atomic spheres is equal to ten. The number n_k of the k points in the irreducible part of the Brillouin zone was 4. The calculations were converged with a rather small number of basis functions per atom in the unit cell ($Rk_{max} = 4.2$, $n_b \approx 37$), n_b was then increased to ≈ 66 ($Rk_{max} = 5.8$) and the calculation run to full convergence. The results obtained with these two n_b differed only slightly. Increasing n_k from 4 to 7 had a very small effect - the effect of La-doping on the local magnetic moment of iron discussed below was found to be more than order of magnitude larger.

All calculations were spin-polarized, assuming the Gorter ferrimagnetic ordering of the Fe spins. For the exchange correlation potential we adopted the GGA form [88] as for the 3d compounds it is superior to the LSDA, as a rule. A calculation with the LSDA exchange-correlation potential [89] was performed for the stoichiometric strontium ferrite in order to compare the results with those reported before [85].

Despite the fact that in many cases GGA gives better results than LSDA when applied to systems with 3d electrons, in the 3d transition metal oxides the energy gap and the magnetic moment are still underestimated [90]. To improve the description of Fe 3d electrons the rotationally invariant version of the LDA+U method was used as described by Liechtenstein *et al.* [27], but with the GGA instead of LSDA exchange-correlation potential. The method should be therefore more correctly denoted as GGA+U. The method is no longer truly *ab-initio* as the values of the Hubbard parameter U and the exchange parameter J must be inserted. These can either be taken from the experiment or estimated using the restricted LSDA (GGA) calculation. The restricted LSDA calculation [91] of LaFeO_3 yielded the values $U=7.7$ and 9.3 eV for ferrous and ferric ion, respectively. A smaller value $U(\text{Fe}^{3+})=5.5$ eV was deduced from the photoemission and inverse photoemission experiments on $\alpha\text{-Fe}_2\text{O}_3$ [92]. The exchange parameter J is believed to be close to its atomic value $J \sim 1$ eV [91]. In any case one can rely on reasonable limits for these parameters rather than on their specific values (this concerns especially U).

In the LDA+U methods an orbitally dependent potential is introduced for the chosen set of electron states, which in the case of hexaferrites are 3d states of Fe. The additional potential has an atomic Hartree-Fock form, but with screened Coulomb and exchange interaction parameters. The problem is that the exchange and correlation already contained in the LSDA or GGA should be subtracted. The form of this 'double counting correction' is spherically symmetrical and it is not clear to which extent its application in the full potential methods is justified, as there is no 'double counting correction' for the non spherical terms in the orbital potential. This problem was avoided by using an effective $U_{eff} = U - J$ instead of the parameter U , and putting the non spherical terms in the orbital potential equal to zero. In what follows

the notation $U \equiv U_{eff}$ is used, but it should be kept in mind that we are dealing with the effective U which is somewhat smaller than the Hubbard parameter as $J/U \approx 0.1-0.2$. To see how the results depend on U , two values $U = 3.4$ and 6.9 eV were employed in addition to the GGA calculation which corresponds to $U = 0$.

5.2.1 Mixed valence region - La substituted Sr ferrite

In the mixed valence region the distribution of the La^{3+} ions is presumably random. In this situation, in order to treat the substitution, the supercell method is usually used. In this method the unit cell is increased, containing the substituted element. For example for a 50% La substituted Sr ferrite the supercell is double of the normal unit cell. However, in the present spin-polarized calculations the unit cell of the parent compound comprises two formula units, or 64 atoms, eleven of which are inequivalent. To perform the supercell calculation with the FPLAPW method would then be costly and for x close to zero or one near to impossible. To overcome this difficulty, we used the fact that the valence electron functions for La and Sr are very similar (the chemical bonding is very similar). The substitution can then be treated by a 'virtual crystal' method, successfully applied to 3d mixed valence oxides earlier [93, 94]. In the 'virtual crystal' method the electrons, the number of which is equal to the number of La atoms, are introduced by increasing the number of valence electrons per unit cell by $N_u x$, where $N_u = 2$ is the number of formula units in the unit cell. To keep the system electrically neutral the Sr atoms with atomic number $Z=38$ are replaced by 'virtual' atoms with fractional atomic number $Z=38+x$. The system retains original periodicity, so that any effect of the disorder is suppressed.

To check the applicability of the method we performed for $\text{La}_{0.5}\text{Sr}_{0.5}\text{Fe}_{12}\text{O}_{19}$ three calculations - in the first one virtual atoms with $Z=38.5$ were introduced instead of all Sr atoms, in the second virtual atoms with $Z=56.5$ replaced all La atoms ($Z=57$), and in the third calculation one of the two Sr in the unit cell was replaced by La (GGA exchange correlation potential was employed). As seen in tab.5.2.1 the calculations yielded very similar results - e.g. the Fe spins change by less than 1% and there is negligible

site	VA Sr	VA La	Sr, La
2a	3.656	3.658	3.657
2b(1)	3.468	3.459	3.440
2b(2)	3.468	3.459	3.464
4f ₁ (1)	-3.378	-3.379	-3.378
4f ₁ (2)	-3.378	-3.379	-3.376
4f ₂ (1)	-3.319	-3.313	-3.337
4f ₂ (2)	-3.319	-3.313	-3.274
12k(1)	3.649	3.648	3.668
12k(2)	3.649	3.648	3.624
total	39.008	39.009	39.006

Table 5.1: $\text{La}_{0.5}\text{Sr}_{0.5}\text{Fe}_{12}\text{O}_{19}$, GGA calculation. Magnetic moments of iron atoms calculated by virtual crystal method with virtual Sr atom (denoted VA Sr), La atom (denoted VA La) and in a standard way with one Sr and one La atom in the unit cell (denoted Sr,La). In the last method the symmetry is reduced and number of inequivalent sites increases from five to nine (all sublattices except 2a are split in two). The total magnetic moment of the unit cell that includes moments on all atoms and in the interstitial is also given. All moments are in μ_B .

change in the density of states near the Fermi energy. We conclude therefore that if the effect of disorder can be neglected, the substitution of strontium by lanthanum is well accounted for by the 'virtual crystal' method and we employed this method to obtain the results described below.

5.3 Results and discussion

5.3.1 Sr hexaferrite

The calculated electronic structure of $\text{SrFe}_{12}\text{O}_{19}$ corresponds to a metal when LSDA is used with the FPLAPW approach (see fig. 5.1), there is a finite density of states (DOS) at the Fermi energy E_F in the majority as well as in the minority spin channel. A Gaussian broadening 0.003 Ry was used to smooth the DOS in this case, as well as in all cases described below. The material is on the border between metal and semiconductor if GGA is used for the exchange potential which enlarges the gap in both spin channels almost

to the size that it overlaps. An insulator results only with a non-vanishing on-site repulsion parameter U . The band structure for GGA+U has a gap of ≈ 1.2 eV for $U = 3.4$ eV that increases to ≈ 2.1 eV as U is increased to 6.9 eV. This is much higher than the experimental value of 0.8 eV (see chapter 3.2.5), and indicates therefore that a lower U value is sufficient. However, for relative comparison of the results any value of U is applicable.

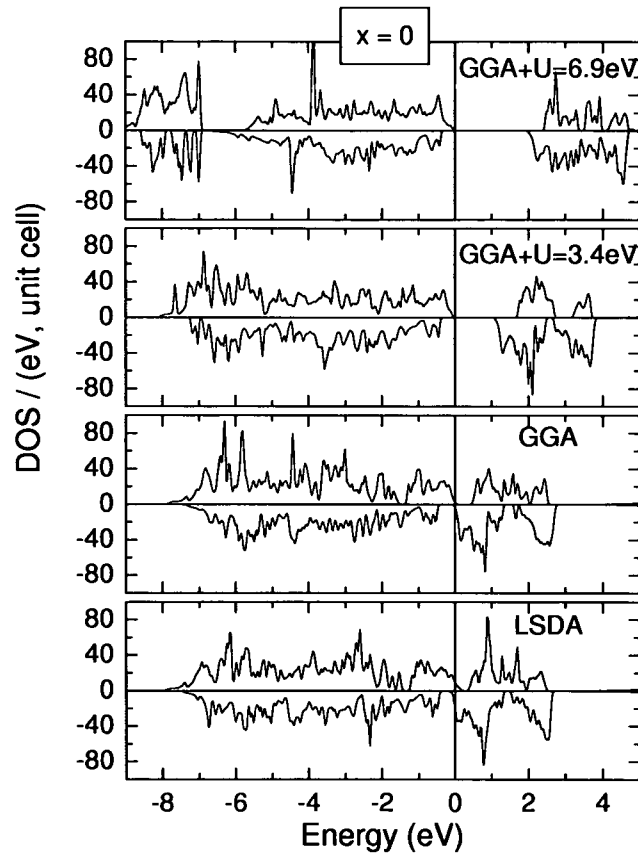


Figure 5.1: Total DOS for majority and minority states in Sr ferrite calculated by LSDA, GGA and GGA+U methods with two different U values; $E_F=0$

The states close to the Fermi energy E_F have predominantly 3d Fe character with some oxygen 2p mixing in the LSDA and GGA calculations. The oxygen character prevails when the GGA+U is applied. The DOS projected on the 3d states of the five inequivalent iron ions are shown in fig.5.2 to-

gether with the sum of the oxygen DOS. Note that the empty states of the projected DOS in this ferrimagnetic structure appear in the (global) minority spin channel only for 2a-, 2b-, and 12k-Fe sites, while they are in the majority spin channel for 4f₁- and 4f₂-Fe sites.

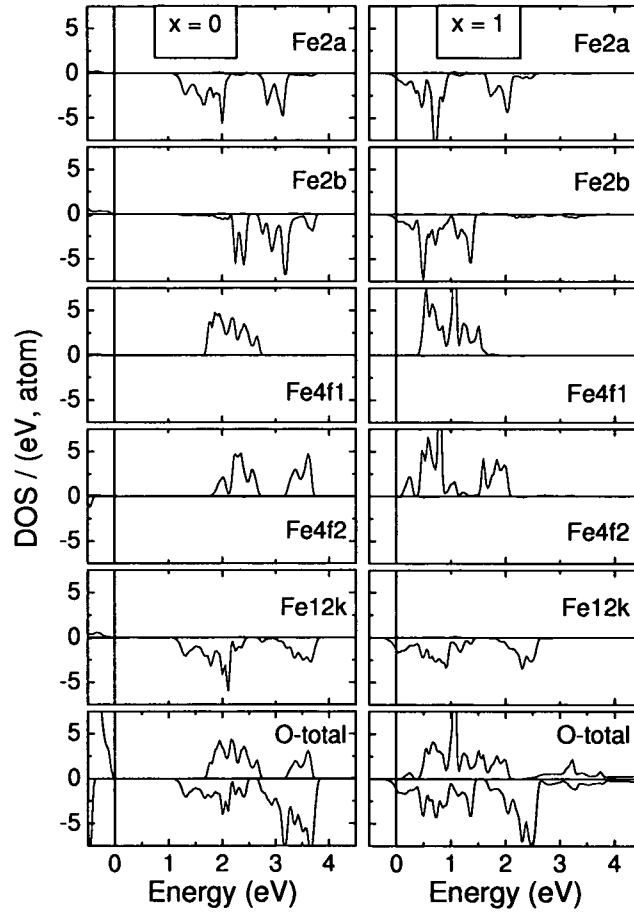


Figure 5.2: Projected DOS on the 3d states of the five Fe sublattices and total O DOS, calculated by GGA+U with $U=3.4$ eV. Left: $\text{SrFe}_{12}\text{O}_{19}$, right: $\text{LaFe}_{12}\text{O}_{19}$

The crystal field splitting of the t_{2g} - and e_g -states on the octahedral Fe-sites (2a, 12k, and 4f₂) is clearly observed in the empty states. At $U=3.4$ eV we find for the splitting, determined as the energy difference of the center of gravity of the partial t_{2g} - and e_g -DOS, 1.61, 1.31, and 1.18 eV for the 12k-, 2a-, and 4f₂-sites, respectively. For the tetrahedral co-ordination the

t_{2g} - e_g splitting is expected to be smaller compared to the splitting on the octahedral sites. This is indeed reflected in the Fe(f_1) DOS - there is no gap dividing these states.

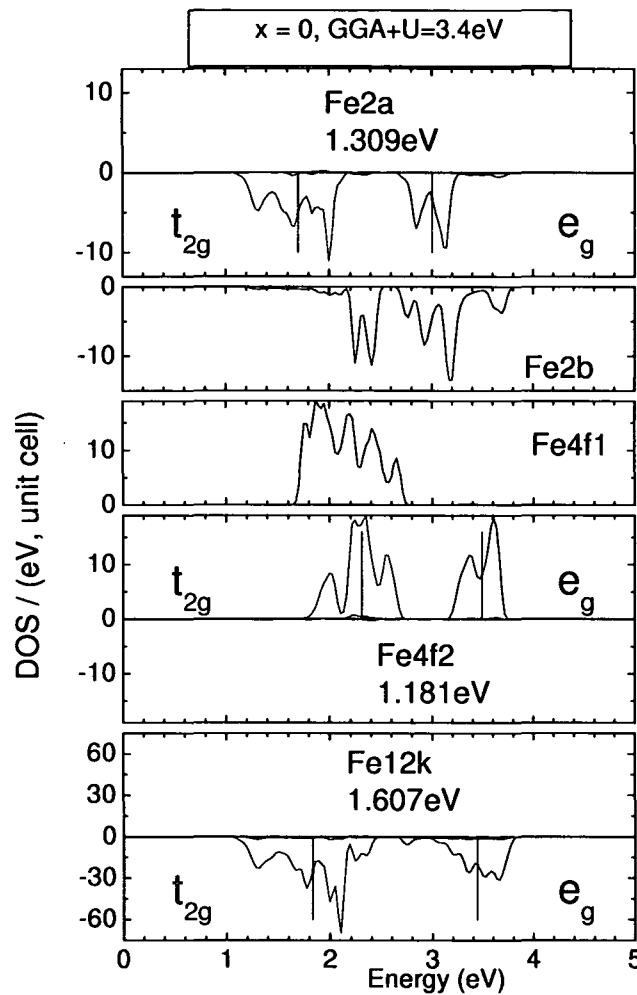


Figure 5.3: Crystal field splitting in t_{2g} - and e_g -states on octahedral Fe sites in Sr hexaferrite observed in the projected DOS

Magnetic moments of all eleven inequivalent atoms and of the interstitial region of the stoichiometric strontium hexaferrite and La hexaferrite calculated by the GGA+U method ($U=3.4$ eV) in comparison with the magnetic moments measured with neutron diffraction are given in tab.5.3.1. A theoretical value of $5 \mu_B/\text{Fe}$ in the ferrimagnetic SrM structure is expected (see

atom	SrM calc.	LaM calc.	LaM exp.
Sr/La	0	-0.01	-
Fe(2a)	4.01	4.00	3.5
Fe(2b)	3.88	3.86	4.0
Fe(4f ₁)	-3.85	-3.86	-3.9
Fe(4f ₂)	-3.95	-3.95	-4.0
Fe(12k)	4.02	3.96	3.8
O(4e)	0.33	0.34	-
O(4f)	0.08	0.08	-
O(6h)	0.03	0.03	-
O(12k ₁)	0.08	0.08	-
O(12k ₂)	0.16	0.12	-
interst.	2.49	1.80	-
total	40.01	38.01	-

Table 5.2: Magnetic moments of the interstitial region and inequivalent atoms in SrFe₁₂O₁₉ and LaFe₁₂O₁₉ calculated by the GGA+U method ($U=3.4$ eV). The total magnetic moment of the unit cell is also given. All moments are in μ_B . In comparison the measured magnetic moments of La hexaferrite by neutron diffraction are shown (see chapter 4.1.4).

chapter 2.2.2), while for the La hexaferrite one Fe site should exhibit a decreased value due to Fe²⁺ present in this compound. Clearly the Gorter spin structure proved energetically favorable for both compounds, but no decreased magnetic moment was obtained, like in the experiment at the 2a site.

5.3.2 La substituted Sr hexaferrite

The electronic structure of Sr_{1-x}La_xFe₁₂O₁₉ in the mixed valence regime ($x=0.25, 0.5, 0.75$ and 1) was calculated using GGA and GGA+U methods. The virtual crystal concept with Sr as the virtual atom was used for $x=0.25$ and 0.5, while for $x=0.75$ La virtual atom was introduced. Fig.5.4 shows resulting total DOS for $U=3.4$ eV.

The nonintegral number of electrons n in the virtual crystal approach ($x=0.25$ and 0.75) implies nonzero density of states at the Fermi energy while for integral n a gap may appear. In all cases the density of the majority

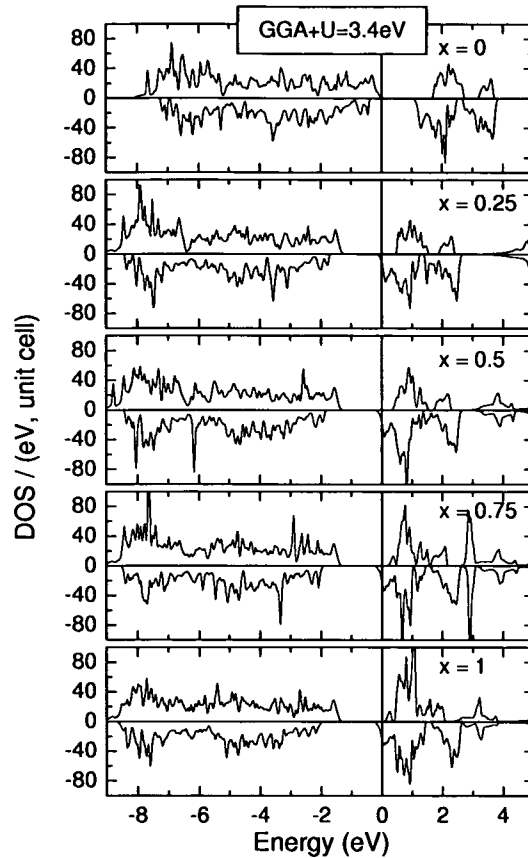


Figure 5.4: Total DOS of $\text{Sr}_{1-x}\text{La}_x\text{Fe}_{12}\text{O}_{19}$ with different La concentrations $x=0, 0.25, 0.5, 0.75, 1$ calculated with GGA+U ($U=3.4$ eV)

spin (spin up) states exhibited a gap, while the DOS of the minority, spin down, states is nonzero at E_F . The electronic structure thus corresponds to a halfmetal with the conduction in the spin down channel only. This is not in agreement with the experiment, where a clear semiconductor like behavior was found for all La concentrations, and is simply a consequence of the virtual crystal approach. However, the halfmetallic character leads to the following dependence of total magnetic moment on the La concentration x : Due to the virtual crystal approach the number of valence electrons per unit cell is $n(x) = n(0) + 2x$. At the same time n is the sum of numbers of majority and minority spin electrons: $n = n_{\uparrow} + n_{\downarrow}$. Because of the gap, n_{\uparrow} is an integer that does not depend on x (in principle it may change by

an integer, but that was not found in the results of calculation). The total magnetic moment m_{tot} is then (see fig.5.5):

$$m_{tot}(x) = n_{\uparrow}(x) - n_{\downarrow}(x) = \quad (5.1)$$

$$n_{\uparrow}(0) - [n(0) - n_{\uparrow}(0) + 2x] = m_{tot}(0) - 2x$$

For the pure La hexaferrite this was confirmed by the magnetization mea-

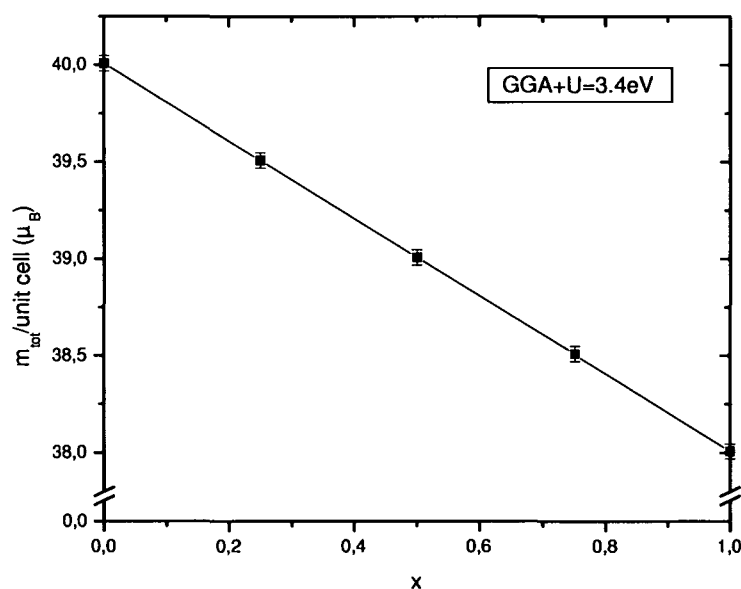


Figure 5.5: Total magnetic moment per unit cell versus La concentration

surements (see chapter 4.1.3), while the resolution of the experiment was too low to observe the changes also for the partly La substituted samples.

When La is substituted for Sr extra valence electrons appear in the system. The explanation of the large magnetic anisotropy of the pure La hexaferrite given by Lotgering [12] hinges on a preference of the additional electron for the 2a Fe sublattice. A direct information on site preferences in real space is provided by the number N_i of electrons in the atomic sphere i . This must be taken with a caution, however, as any such division reflects the real situation only approximately, in particular N_i depend on the chosen atomic radii. Nevertheless, taking the same reasonable value 1.9 a.u. for the radius of all five inequivalent irons, we believe that a good estimation for the preference

is obtained. The difference $\Delta N_i = N_i(x) - N_i(0)$ for the five inequivalent Fe sites is plotted in fig.5.6 for $U=0, 3.4$ and 6.9 eV.

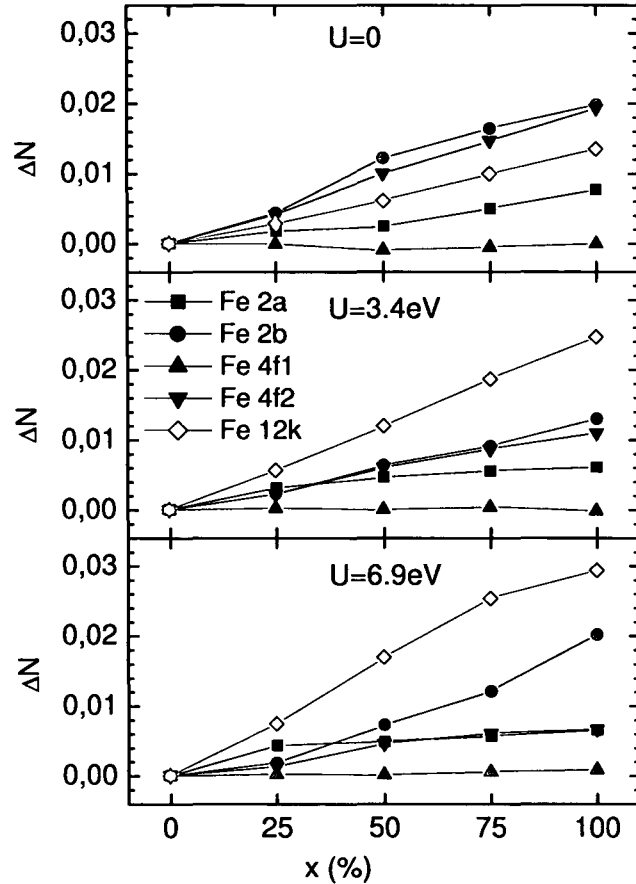


Figure 5.6: Difference of the number of electrons per atom $\Delta N = N(x) - N(0)$ for the five Fe sites as function of the La concentration for the GGA (upper panel), GGA+U, $U=3.4$ eV (middle panel) and $U=6.9$ eV (lower panel) calculations

First of all it is seen that most of the additional electrons are, in fact, not contained in atomic spheres of Fe, the total count at $x = 1$ accounts for only 0.38 electrons per unit cell. The fact that most of the additional electrons end up in the interstitial regime indicates already that no significant site preferences are predicted. In addition, a small but finite DOS at E_F is predicted for $x = 1$. This corresponds well to the measurement showing that the resistivity of $\text{LaFe}_{12}\text{O}_{19}$ at room temperature is several orders of

magnitude smaller than that of $\text{SrFe}_{12}\text{O}_{19}$ (chapter 4.1.2).

In more detail, the behavior of the 2a-, 2b-, and 4f₁-sites is predicted fairly independent of the special value of U : No additional charges enter the sphere at 4f₁-Fe, and at the 2a site the charge difference stays below 1% in all cases. The 2b Fe sublattice is predicted to take app. twice as much electrons at $x = 1$, but due to the small multiplicity this still is a small percentage of the total count. However, it is also seen that the calculated distribution of the doped electrons in the unit cell does depend significantly on the parameter U for the 12k- and 4f₂-sublattices. With increasing U ΔN_{12k} increases, while ΔN_{4f2} decreases at all x .

This may indicate an oversimplification in the calculations, since the same on-site repulsion for all Fe sites while in reality U depends on coordination and bonding. Preferably one should determine U separately for all five inequivalent sites. Due to the complexity of the structure such calculations are outside the scope of the present work. To check for the influence of such a difference in the local U the GGA+ U calculation at $x = 1$ was performed with $U=5.7$ eV for the 2a-site while it was kept at $U=6.9$ eV for all other Fe-sublattices. As expected, the smaller on-site repulsion increases the electron content of the atomic sphere at the 2a Fe, in this case by 0.04 electrons. This indicates that the absolute effect of site specific parameters U will be small, but inspection of fig.5.6 shows that the influence on the relative amount of additional charge at the five sites might be considerable.

In the LDA+ U -like methods the energy of occupied states is lowered, while the energy of unoccupied states increases. As a consequence more solutions of the selfconsistent procedure may be obtained, depending on the starting occupation matrix. To check whether in this way a solution with strong localization at 2a-sites as proposed from the experimental point of view is obtained, a calculation was performed in which the starting population matrices corresponded to this situation. After several iterations the electron was smeared over different sites, however, and the converged result was identical with the one obtained before. However, in the 'virtual crystal' approach the disorder is disregarded. As a consequence one cannot rule out that (especially for small x) the disorder may cause the localization.

Site preferences can be calculated also for the spins carried by the addi-

tional electrons. The advantage of the magnetizations is that they can, in principle, be determined from experiments. 5.2 shows that due to the half-metallic character the dependence of the total magnetization on x contains no information on such preferences. The calculated DOS shown in fig.5.4 confirm, however, that the half-metallic state is due to E_F entering the (global) minority spin DOS. From the projected DOS in fig.5.2 it is seen that indeed only 2a-, 2b-, and 12k-Fe contribute to this part of the total DOS. Again we consider the difference of the concentration dependent sublattice magnetizations $m_i(x)$ with respect to the situation in the stoichiometric Sr-hexaferrite:

$$\Delta m_i(x) = m_i(0) - m_i(x). \quad (5.2)$$

Note the different sign compared to the charge difference. Due to the gap in the total majority spin DOS only the population of the minority spin states is changed and it increases. This implies in the ferrimagnetic arrangement a decreasing absolute sublattice magnetization on 2a-, 2b-, and 12k-sites, but an increasing one on the antiparallel 4f-sublattices.

Fig. 5.7 shows that the redistribution of spins in the unit cell upon doping are, in fact, predicted to be fairly complex. In accord with the charge distributions discussed above there are no changes on the 4f₁-sublattice and the results for the 2a- and 2b-sites show no systematic dependence on U . Again, the main effect of the on-site repulsion is to increase any preference the system might have for the 12k-sites, and suppressing migration to the 4f₂-sites. There are differences in the details of the charge and spin redistribution upon doping but a direct comparison of the charge and spin count rests on the assumption that the majority spin states of all individual Fe ions are completely filled and stay so. This may well not be the case with the precision required here to allow a discussion of such details.

The overall changes of charge or spin counts in the atomic spheres are small, in contrast to the empirical model of localization at the 2a sites. The majority of the electrons introduced by the substitution of Sr by La ends up in the interstitial regime, without clear indications for localization. No change occurs on the 4f₁-sites, a relatively small increase of the charge is obtained for the 2a-sublattice and app. twice as much on 2b-Fe. The largest changes

are predicted for the 12k-sites, but they depend on the on-site Coulomb parameter U , as they do for 4f₂-Fe.

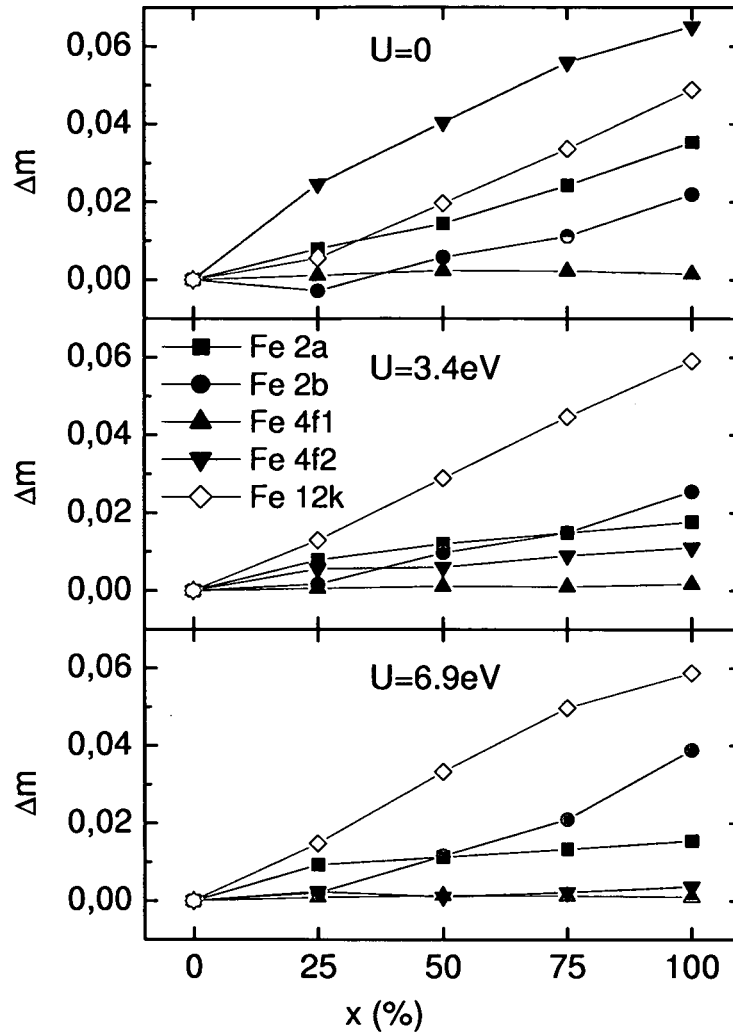


Figure 5.7: $\Delta m = m(0) - m(x)$ as a function of the La concentration for the GGA (upper panel), GGA+U, $U=3.4$ eV (middle panel) and $U=6.9$ eV (lower panel) calculations. The absolute values of sublattice magnetizations on 2a-, 2b-, and 12k decrease while they increase on 4f₁ and 4f₂.

Chapter 6

Conclusion

This work was started in order to investigate the influence of substitution of the Sr or Ba ion in the M-type hexaferrites by rare earth elements on their magnetic and structural properties.

6.1 First studies

To this end first studies were performed on Sr hexaferrite samples prepared by hydrothermal synthesis where a part of Sr ions was substituted by a rare earth element. These samples were obtained from the University of Birmingham and the elements used were La, Sm, Nd, Pr in concentrations of RE/Sr=1/24, 1/20, 1/16, 1/8, 1/4, 1/2. Measurements of magnetic properties of these samples showed that no improvement, concerning anisotropy and magnetization, is obtained by the substitution. Anisotropy measured by singular point detection (SPD) technique at room temperature showed only slight increase and no clear dependence on the RE concentration was observed. The magnetization at room temperature and 4.2 K was decreased with increasing amount of substitution. The low temperature anisotropy was almost constant with respect to temperature, like in the pure Sr hexaferrite. With X-ray diffraction the reason for this behavior was found in a high amount of secondary phases for high RE concentrations. It seems that this preparation method is not appropriate for RE substituted hexaferrites with higher RE concentrations. The RE element does not enter the hexaferrite

structure, but forms secondary phases instead and a part may enter the grain boundaries. Only for very small nominal concentrations up to RE/Sr=1/16, it is granted that the RE enters the hexaferrite lattice, since a strong influence on the NMR spectrum occurs. A shift of all five ^{57}Fe peaks was found, which can be explained by the additional electron on the Fe sites, that is necessary to compensate for the valence change on the Sr site (2+) by the RE element (3+). To influence all Fe sites the electron has to be delocalized, forming a large polaron. For higher concentrations the NMR spectrum but also Mössbauer exhibited no significant deviation from the pure Sr hexaferrite. This leads to the conclusion that the preparation of RE substituted samples cannot be performed in any case in the same way as for the usual M-type hexaferrites.

6.2 Preparation

In order to develop an appropriate preparation method for RE substituted hexaferrites a collaboration with an institute for materials research in Chihuahua, Mexico, was started. The work was focused on the pure La hexaferrite and La substituted Sr hexaferrite. La hexaferrite was reported as interesting magnetic compound due to a very strong anisotropy at low temperatures. La exhibits no magnetic moment, but it was assumed that if the preparation method works for La it may also work for other RE elements. Four different preparation methods, common in ferrite production, were tried for the pure La hexaferrite: Mechanical alloying by using a steel ball mill, coprecipitation, sol gel and sol gel autocombustion method. With all four methods the hexaferrite phase was obtained. It was found out that the essential point in the preparation is the heat treatment at high temperatures. The La hexaferrite is a high temperature phase, stable only in a narrow temperature range of 40°C around 1350°C. At room temperature it is a metastable compound, and decomposes easily. Therefore a rapid quenching, e.g. in water, has to be performed after the heat treatment. Cooling down the sample slowly, e.g. in the furnace, it decomposes in LaFeO_3 (La-orthoferrite) and Fe_2O_3 (hematite). By variation of the furnace temperature and the La excess it was possible to minimize the amount of secondary phases. The sample with

the smallest amount prepared by coprecipitation still contained 10% LaFeO_3 and Fe_2O_3 , the one prepared by mechanical alloying was pure according to XRD. Sr hexaferrite samples with different La amount were mainly prepared by mechanical alloying and ratios of $\text{La}/\text{Sr}=1/8, 1/4, 1/2, 1/1, 1/3$ were used. A heat treatment of these samples at temperatures like used for the pure Sr hexaferrite resulted in a high amount of secondary phase. Again the La did not enter the hexaferrite structure. With increasing temperature the amount of secondary phases was decreased. It was therefore decided to prepare all samples with the same temperature as necessary to obtain the pure La hexaferrite. However, the formation of secondary phases for higher La concentrations ($>1/4$) could not be avoided. It was then tried to obtain Dy and Er hexaferrite by the same method. The temperature range of stability of this phase is unknown, therefore several temperatures were tried, without success. We conclude that the preparation of RE substituted samples is only possible by conventional methods, if a heat treatment in the right temperature range is performed, followed by a rapid quenching.

6.3 Structural properties

By XRD it was found that the lattice parameter c decreases with increasing La concentration, while a is increasing slightly. The unit cell volume therefore decreases with increasing La concentration. The most interesting result was that the pure La hexaferrite exhibits a lattice distortion at low temperatures. This distortion takes place in the basal plane of the hexagonal lattice, increasing the parameter a but reducing b in the orthorhombic description. The structure can be described by the spacegroup CmCm . The distortion was observed in the thermodiffractogram obtained by neutrons, the temperature of the phase transitions was found in the specific heat. This distortion seems to have a strong influence on the magnetocrystalline anisotropy of the La hexaferrite. In non of the partly with La substituted Sr ferrite samples a change of structure was observed.

6.4 Magnetic properties

6.4.1 Anisotropy

The anisotropy of all samples was measured by SPD technique and showed a strong increase with decreasing temperature for the pure La hexaferrite. This increase can be explained by a combined effect of the lattice distortion and Fe^{2+} exhibiting an orbital momentum. Fe^{2+} appears in the pure La hexaferrite for reasons of charge compensation, due to the different valence of La and Sr. The presence of the Fe^{2+} ion was verified by an increased value of the isomer shift at the 2a site, calculated from the room temperature Mössbauer spectrum of the sample. The Fe^{2+} ion establishes an orbital momentum with decreasing temperature down to the temperature of the phase transition. Then the momentum is fully established, but the structure is not stable and so the lattice distortion starts. This was observed in the hyperfine field versus temperature, that shows a strong decrease at the 2a site down to 110 K and then stays almost constant. The opposite behavior was found for the quadrupole shift, which is clearly connected to the lattice distortion. The increase in anisotropy may be explained in the one ion model by a Jahn-Teller like effect. The 2a site in the $P6_3/mmc$ structure is of octahedral coordination and Fe^{2+} is in the $3d^6$ state. Therefore the 3d energy levels are split in a 3-fold degenerate t_{2g} energy ground state and a 2-fold degenerate e_g energy level. The ground state degeneracy is further lifted by the distortion. It was shown for example for the Co^{2+} in the spinel structure that a trigonal distortion leads to a 2-fold degenerate ground state. In that case the LS coupling has to be treated in second order perturbation theory and could successfully explain the increased anisotropy in Co substituted magnetite. This theory was also applied to the La-Co substituted hexaferrites. For the Fe^{2+} a trigonal distortion would lead to a non degenerate ground state, which cannot explain the increased anisotropy. The distortion that occurs in the M-type La hexaferrite is more close to a tetragonal distortion than to a trigonal one. In that case also Fe^{2+} would exhibit a 2-fold degenerate ground state and the same reasoning as for the Co^{2+} may be applied. From current investigation of the interatomic distances at the 2a site a clearer picture of the distortion

should be obtained and crystal field calculation may turn this qualitative picture in a quantitative one. The idea was supported by the latest electron structure calculations performed on the distorted lattice, that indeed confirmed the localization of Fe^{2+} at the 2a site and showed convergence for a 2-fold degenerate ground state.

For the La substituted Sr hexaferrite with $\text{La}/\text{Sr}=3/1$, the anisotropy showed the same increase, but less strong than in the pure La hexaferrite. Although no distortion was found in the neutron diffractogram, the disappearance of the 2a line from the NMR spectrum together with the 12k-, 4f2-, and 4f1-lines as well as the La spectrum approaching broadened versions of the lines observed in LaM indicates that local distortions occur. These local distortions lead to the same effect in anisotropy as in the pure La hexaferrite. For the samples with lower La concentration the anisotropy showed completely different behavior: The anisotropy decreases with decreasing temperature. Since NMR spectra of these samples showed a strong effect on the 4f1 site, it may be an explanation if the Fe^{2+} enters in these samples the 4f1 site. This is also reasonable due to the crystal structure, since the 4f1 site is close to 2a and therefore they could easily exchange an electron. At very low La concentrations the additional electron may be delocalized, like in the samples prepared by hydrothermal method. At a higher concentration it localizes at the 4f1 site and with increasing La amount also the 2a site will be occupied. Only for the pure La ferrite we can find Fe^{2+} exclusively at the 2a site and this seems to lead to a lattice distortion at low temperatures.

6.4.2 Magnetization and coercivity

Despite the high magnetocrystalline anisotropy at low temperatures all samples exhibited very small coercive fields. This is due to the strong grain growth during the heat treatment at high temperatures. The grain size of around $100\ \mu\text{m}$ was observed in the optical microscope as well as in the scanning electron microscope.

The magnetization in the La hexaferrite was reduced compared to Sr hexaferrite and a value of $18.9\ \mu_B/\text{formula unit}$ at 4.2 K for the magnetic moment was calculated. This is due to the reduced magnetic moment of

the Fe^{2+} ion compared with Fe^{3+} . This proves that the Fe^{2+} can enter only a spin up site. The magnetic moment due to the orbital momentum was neglected in the calculation since small changes in the order of $0.1 \mu_B$ cannot be resolved in the experiment. A clear reduction or increase in magnetization was also not observed for the partly substituted samples, for the same reason.

The local magnetic moments at the five different Fe sites, determined by neutron diffraction, confirmed the reduction at the 2a site, clearly indicating the presence of Fe^{2+} .

6.5 Electron structure calculations

Electron structure calculations based on the density functional theory did not lead to any conclusion about a site preference for the Fe^{2+} . The overall changes of charge or magnetic moment in the atomic spheres are small, in contrast to the expected localization at the 2a sites. The majority of the electrons introduced by the substitution of Sr by La ends up in the interstitial regime, without a clear indication for a localization.

The total magnetic moment per unit cell showed a linear decrease with increasing La concentration. This was confirmed by the experiment for the pure La hexaferrite.

A halfmetallic character was observed for all mixed valence compounds including $\text{LaFe}_{12}\text{O}_{19}$ with conduction in the minority spin channel. Only $\text{SrFe}_{12}\text{O}_{19}$ was found to be an insulator employing the GGA+U method. This may be only a consequence of the virtual crystal method and the fact that a relaxation of the lattice was not considered.

Especially for the La hexaferrite it is therefore necessary to perform calculations in the distorted crystal lattice. The latest calculations supported the idea of a localization of the additional electron at the 2a site with a two-fold degenerate ground state. Taking this into account all experiments and calculations fit well together, creating a picture that is able to explain the strongly increased anisotropy of La hexaferrite: The additional electron at the 2a site establishes a strong orbital momentum that interacts with the crystal field of the distorted lattice in a Jahn-Teller like effect.

Bibliography

- [1] Skomski, R., and Coey, J. M. D. (1999). *Permanent Magnetism* (ISBN 0750304782). Institute of Physics Publishing, Bristol and Philadelphia.
- [2] Went, J. J., Ratheneau, G. W., Gorter, E. W., and VanDosterhout, G. W. (1951). *Philips Techn. Rev.* **13**, 194.
- [3] Adam, J. D., Davis, L. E., Dionne, G. F., Schloemann, E. F., and Stitzer, S. N. (2002). "Ferrite devices and materials". *IEEE Transactions on Microwave Theory and Techniques* **16(8)**, 1103–1118.
- [4] Kimura, T., Lawes, G., and Ramirez, A. P. (2005). Electric Polarization Rotation in a Hexaferrite with Long-Wavelength Magnetic Structure. *Physical Review Letters* **94**, 137201.
- [5] Kojima, H. (1982). *Ferromagnetic Materials Vol.3*. E.P. Wolfarth, North-Holland, Amsterdam.
- [6] Smolenski, A. G., and Andreev, A. A. (1961). *Bull. Acad. Sci.* **25**, 1405.
- [7] Iida, K., Minachi, Y., Masuzawa, K., Kawakami, M., Nishio, H., and Taguchi, H. (1999). *Journal of the Magnetism Society Japan* **23**, 1093.
- [8] Wang, J. F., Ponton, C. B., and Harris, I. R. (2001). "A study of the magnetic properties of hydrothermally synthesised Sr hexaferrite with Sm substitution". *Journal of Magnetism and Magnetic Materials* **234**, 233–240.
- [9] Wang, J. F., Ponton, C. B., and Harris, I. R. (2002). "A study of Nd substituted Sr hexaferrite prepared by Hydrothermal Synthesis". *IEEE Transactions on Magnetics* **38(5)**, 2928–2930.

- [10] Wang, J. F., Ponton, C. B., Grössinger, R., and Harris, I. R. (2004). "A study of La-substituted strontium hexaferrite by hydrothermal synthesis". *Journal of Alloys and Compounds* **369**, 170–177.
- [11] Deschamps, A., and Bertraut, F. (1957). "Sur la substitution de baryum par une terre rare dans l'hexaferrite $\text{BaO} \cdot 6\text{Fe}_2\text{O}_3$ ". *France Académie des Sciences séance du 17 Juin 1957*, 3069–3072.
- [12] Lotgering, F. K. (1974). "Magnetic anisotropy and saturation of $\text{LaFe}_{12}\text{O}_{19}$ and some related compounds". *Journal of Physics and Chemistry of Solids* **35**, 1633–1639.
- [13] Grössinger, R., Küpferling, M., Blanco, J. C. T., Wiesinger, G., Müller, M., Hilscher, G., Pieper, M. W., Wang, J. F., Ponton, C. B., and Harris, I. R. (2003). "Rare earth substitutions in M-type ferrites". *IEEE Transactions on Magnetics* **39** (5), 2911–2913.
- [14] Ataie, A., Harris, I. R., and Ponton, C. P. (1995). "Magnetic properties of hydrothermally synthesized strontium hexaferrite as a function of synthesis conditions". *Journal of Materials Science* **30**, 1429–1433.
- [15] Kramers, H. A. (1934). *Physica* **1**, 182.
- [16] Blundell, S. (2001). *Magnetism in condensed matter*. Oxford University Press, New York.
- [17] Craik, D. (1995). *Magnetism: principles and applications*. Wiley, Chichester.
- [18] http://www.uky.edu/~holler/html/orbitals_2.html .
- [19] Yosida, K., and Tachiki, M. (1957). *Prog. Theor. Phys.* **17**, 331.
- [20] Slonczewski, J. C. (1958). "Origin of magnetic anisotropy in Cobalt-substituted Magnetite". *Physical Review* **110**(6), 1341–1348.
- [21] Yosida, K. (1996). *Theory of Magnetism*. Springer-Verlag, Berlin/Heidelberg.

- [22] Stoner, E. C., and Wohlfarth, E. P. (1948). "A mechanism of magnetic hysteresis in heterogeneous alloys". *Philosophical Transactions of the Royal Society of London A* **240**, 599–642.
- [23] Grössinger, R. (1981). "A critical examination of the law of approach to saturation". *Physica Status Solidi (a)* **66**, 665–674.
- [24] Cottenier, S. (2002). Density Functional Theory and the family of (L)APW-methods: a step-by-step introduction (ISBN 90-807215-1-4). Instituut voor Kern- en Stralingsfysica, Leuven.
- [25] Hohenberg, P., and Kohn, W. (1964). *Physical Review* **136(3B)**, 864.
- [26] Kohn, W., and Sham, L. J. (1965). *Physical Review* **140(4A)**, 1133.
- [27] Liechtenstein, A. I., Anisimov, V. I., and Zaanen, J. (1995). Density-functional theory and strong interactions: Orbital ordering in Mott-Hubbard insulators. *Physical Review B* **52(8)**, 54675470.
- [28] Jackson, J. D. (1999). Classical electrodynamics. Wiley, New York.
- [29] Bertotti, G. (1998). Hysteresis in Magnetism. Academic Press, San Diego.
- [30] Adelsköld, V. (1938). "X-ray Studies on Magneto-Plumbite, $\text{PbO} \cdot 6\text{Fe}_2\text{O}_3$, and other Substances resembling Beta-Alumina, $\text{Na}_2\text{O} \cdot 11\text{Al}_2\text{O}_3$ ". *Arkiv för Kemi, Mineralogi och Geologi* **12A (29)**, 1–9.
- [31] Lisjak, D. (2003). "Microwave ferrites". *Informacije-MIDEM* **33(3)**, 195–201.
- [32] Morel, A. (2003). "Amelioration des proprietes magnetiques des aimants permanents du type Hexaferrite de Strontium par la substitution Lanthane-Cobalt", doctoral thesis. University of Rouen, Rouen.
- [33] Dahlgren, M. (1998). Study of Exchange Enhanced Magnetic Materials. Vienna University of Technology (doctoral thesis), Vienna.

- [34] Obradors, X., Solans, X., Collomb, A., Samaras, D., Rodriguez, J., Pernet, M., and Font-Alba, M. (1988). "Crystal Structure of Strontium Hexaferrite $\text{SrFe}_{12}\text{O}_{19}$ ". *Journal of Solid State Chemistry* **72**, 218–224.
- [35] Muller, J., and Collomb, A. (1991). "A new representation of the bipyramidal site in the $\text{SrFe}_{12}\text{O}_{19}$ M-type hexagonal ferrite between 4.6 and 295 K". *Journal of Magnetism and Magnetic Materials* **103**, 194–203.
- [36] Kimura, K., Ohgaki, M., Tanaka, K., Morikawa, H., and Marumo, F. (1990). "Study of the bipyramidal site in magnetoplumbite-like compounds $\text{SrM}_{12}\text{O}_{19}$ (M=Al, Fe, Ga)". *Journal of Solid State Chemistry* **87**, 186–194.
- [37] Albanese, G. (1977). "Recent advances in hexagonal ferrites by the use of nuclear spectroscopic methods". *Journal de Physique C1-4* (**38**), 85–94.
- [38] Hahn, E. T. (2002). *International Tables for Crystallography*. Institut für Kristallographie, Aachen.
- [39] Pauling, L. (1960). *The nature of chemical bond*. Cornell University Press Ithaca, New York.
- [40] Ahrens, L. H. (1952). "The use of ionization potentials Part 1. Ionic radii of the elements". *Geochimica et Cosmochimica Acta* **2**(3), 155–169.
- [41] Gorter, E. W. (1957). *Proceedings IEEE* **104B**, 255.
- [42] Grill, A., and Haberey, F. (1974). "Effect of diamagnetic substitutions in $\text{BaFe}_{12}\text{O}_{19}$ on the magnetic properties". *Applied Physics A* **3**(2), 131–134.
- [43] Smit, J., and Wijn, H. P. J. (1959). *Ferrites*. N. V. Philips Gloeilamp-enfabrieken, Eindhoven.
- [44] Lotgering, F. K., Locher, P. R., and VanStapele, R. P. (1980). "Anisotropy of hexagonal ferrites with M, W and Y structures containing Fe^{3+} and Fe^{2+} as magnetic ions". *Journal of Physics and Chemistry of Solids* **41**, 481–487.

- [45] Wanatabe, H. (1957). "On the ground level splitting of Mn^{++} and Fe^{+++} in a nearly cubic crystalline field". *Prog. Theor. Phys. Japan* **17**, 405–420.
- [46] Novak, P. (1994). "Superposition model analysis of the magnetocrystalline anisotropy of Ba-ferrite". *Czechoslovak Journal of Physics* **44(6)**, 603–611.
- [47] Asti, G., and Rinaldi, S. (1976). "On the magnetic anisotropy in hexagonal ferrites". *Proceedings of AIP Annual Conference* p. 214.
- [48] Callen, H. B., and Callen, E. (1966). "The present status of the temperature dependence of the magnetocrystalline anisotropy, and the $l(l+1)/2$ power law". *Journal of Physics and Chemistry of Solids* **27**, 1271–1285.
- [49] You, X., Daping, C., Guilin, Y., and Hongru, Z. (1989). *Proceedings ICF-5* p. 485.
- [50] Hongru, Z., You, X., Jizhe, L., Guilin, Y., Mu, L., Tongzheng, J., Zijun, W., Benxi, G., and Shiyin, H. (1989). "Magnetic anisotropy of hexaferrites". *Proceedings ICF-5* p. 473.
- [51] Kittel, C. (1946). *Physical Review* **70**, 965.
- [52] Néel, L. (1947). *Comptes rendus* **224**, 1488.
- [53] Chikazumi, S. (1997). *Physics of Ferromagnetism*. Clarendon Press, Oxford.
- [54] Kools, F. (1985). *J. Phys., Colloque C6, annex No.9* **46**, 349.
- [55] Asti, G., Carbucicchio, M., Deriu, A., Lucchini, E., and Slokar, G. (1980). "Magnetic characterization of Ca substituted Ba and Sr hexaferrites". *Journal of Magnetism and Magnetic Materials* **20**, 44–46.
- [56] Yamamoto, H., Kawaguchi, T., and Nagakura, M. (1979). "A new permanent magnet material: Modified Ca ferrite". *IEEE Transactions on Magnetism* **15(4)**, 1141 – 1146.

- [57] Drofenik, M., Hanzel, D., and Moljk, A. (1973). "Study of LaFe₁₂O₁₉ from Mössbauer spectra". *Journal of Materials Science* **8**(7), 924–927.
- [58] Sauer, C., Köbler, U., Zinn, W., and Stäblein, H. (1978). "High field Mössbauer effect study of LaFe₁₂O₁₉". *Journal of Physics and Chemistry of Solids* **39**, 1197–1201.
- [59] Aharoni, A., and Schieber, M. (1961). "Magnetic Moment of Lanthanum Magnetoplumbite Ferrite". *Physical Review* **123**(3), 807–809.
- [60] Ogata, Y., Kubota, Y., Takami, T., Tokunaga, M., and Shinokara, T. (1999). "Improvements of magnetic properties of Sr ferrite magnets by substitutions of La and Co". *IEEE Transactions on Magnetics* **35**(5), 3334–3336.
- [61] Moruzzi, V. L., and Shafer, M. W. (1960). "Phase equilibria in the system La₂O₃-Iron Oxide in air". *Journal of the American Ceramic Society* **43**, 367–372.
- [62] Ding, J., Maurice, D., Miao, W. F., McCormick, P. G., and Street, R. (1995). "Hexaferrite magnetic materials prepared by mechanical alloying". *Journal of Magnetism and Magnetic Materials* **150**, 417–420.
- [63] MartinezGarcia, R., RegueraRuiz, E., and EstevezRams, E. (2001). *Mat.Lett* **50**, 183.
- [64] Yue, Z., Zhou, J., Li, L., and Gui, Z. (2001). "Effects of MnO₂ on the electromagnetic properties of NiCuZn ferrites prepared by sol-gel auto-combustion". *Journal of Magnetism and Magnetic Materials* **233**, 224–229.
- [65] Morin, F. J. (1950). "Magnetic susceptibility of α -Fe₂O₃ and α -Fe₂O₃ with added Titanium". *Physical Review Letters to the Editor* **78**, 819–820.
- [66] Pankhurst, Q. A., Johnson, C. E., and Thomas, M. F. (1986). "A Mössbauer study of magnetic phase transitions in α -Fe₂O₃ crystals". *Journal Physica C: Solid State Physics* **19**, 7081–7098.

- [67] Ding, J., Miao, W. F., McCormick, P. G., and Street, R. (1998). "High-coercivity ferrite magnets prepared by mechanical alloying". *Journal of Alloys and Compounds* **281**, 32–36.
- [68] Rietveld, H. M. (1969). *Journal of Applied Crystallography* **2**, 65.
- [69] Euler, F., and Bruce, J. A. (1965). "Oxygen coordinates of compounds with garnet structure". *Acta Crystallographica* **19**, 971–978.
- [70] Mott, N. F., and Davis, E. A. (1979). *Electronic Processes in Noncrystalline Materials*. Clarendon, Oxford.
- [71] Overhof, H., and Thomas, P. (1989). *Electronic transport in hydrogenated amorphous semiconductors*. Springer, Berlin.
- [72] Asti, G., and Rinaldi, S. (1972). "Nonanalyticity of the magnetization curve: application to the measurement of the anisotropy in polycrystalline samples". *Physical Review Letters* **28** [24], 1584–1586.
- [73] Schramberg, M. (1995). product catalogue. Magnetfabrik Schramberg, Schramberg.
- [74] Kools, F. (2003). *Science technology of ferrite magnets - Modelling of coercivity and grain growth inhibition (doctoral thesis)*. Technische Universiteit Eindhoven, Eindhoven.
- [75] Wegener, H. (1966). *Der Mössbauer-Effekt und seine Anwendungen in Physik und Chemie*. Bibliographisches Institut Hochschultaschenbücher, Mannheim.
- [76] Cohen, M. H., and Reif, F. (1957). "Quadrupole effects in Nuclear Magnetic resonance", *Solid State Physics* **5**. Springer-Verlag, Heidelberg.
- [77] Yasuoka, H., Nishihara, H., and Nakamura, Y. (1971). Observation of ^{51}V NMR in antiferromagnetic state of V_2O_3 . *Physics Letters* **37A**(4), 299–300.
- [78] Pieper, M. W., Caspary, E. G., Adelman, P., and Roth, G. (1993). "Ferromagnetism in the insulating cuprate $\text{La}_4\text{Ba}_2\text{Cu}_2\text{O}_{10}$ ". *Journal of Magnetism and Magnetic Materials* **135**, 319–325.

- [79] Slichter, C. P. (1978). Principles of magnetic resonance. Springer-Verlag, Heidelberg.
- [80] Vegard, L. (1921). *Zeitschrift für Physik* **5**, 17–21.
- [81] Vegard, L. (1928). *Zeitschrift für Kristallographie* **67**, 148–163.
- [82] Lechevallier, L., LeBreton, J. M., Wang, J. F., and Harris, I. R. (2003). “Structural analysis of hydrothermally synthesized $\text{Sr}_{1-x}\text{Sm}_x\text{Fe}_{12}\text{O}_{19}$ hexagonal ferrites”. *Journal of Magnetism and Magnetic Materials* **269**[2], 192–196.
- [83] Müller, M. (2003). Seltenerd-Substitution in M-Typ-Hexaferriten (Projektarbeit). TU Wien, Wien.
- [84] Pieper, M. W., Küpferling, M., Harris, I. R., and Wang, J. F. (2004). “Large polarons in rare-earth doped hexaferrites observed by NMR”. *Journal of Magnetism and Magnetic Materials* **272-276**, 2219–2220.
- [85] Fang, C. M., Kools, F., Metselaar, R., de With, G., and de Groot, R. A. (2003). Magnetic and electronic properties of strontium hexaferrite $\text{SrFe}_{12}\text{O}_{19}$ from first-principles calculations. *Journal of Physics Condensed Matter* **15**, 6229–6237.
- [86] Blaha, P., Schwarz, K., Madsen, G. K. H., Kvasnicka, D., and Luitz, J. (2001). Wien2k, an augmented plane wave + local orbitals program for calculating crystal properties (ISBN 3950103112). Karlheinz Schwarz, Vienna University of Technology, Wien.
- [87] Singh, D. (2001). Plane waves, pseudopotentials and the LAPW method. Kluwer Academic.
- [88] Perdew, J. P., Burke, S., and Ernzerhof, M. (1996). Generalized Gradient Approximation Made Simple. *Physical Review Letters* **77**(18), 3865–3868.
- [89] Perdew, J. P., and Wang, Y. (1992). Accurate and simple analytic representation of the electron-gas correlation energy. *Physical Review B* **45**(23), 13244–13249.

- [90] Yang, Z., Huang, Z., Ye, L., and Xie, X. (1999). Influence of parameters U and J in the LSDA+ U method on electronic structure of the perovskites LaMO_3 ($M=\text{Cr, Mn, Fe, Co, Ni}$). *Physical Review B* **60(23)**, 15674–15682.
- [91] Solovyev, I., Hamada, N., and Terakura, K. (1996). t_{2g} versus all 3d localization in LaMO_3 perovskites ($M=\text{Ti, Cu}$): First-principles study. *Physical Review B* **53(11)**, 7158–7170.
- [92] Zimmermann, R., Steiner, P., Claessen, R., Reinert, F., Hüfner, S., Blaha, P., and Dufek, P. (1999). Electronic structure of 3d-transition-metal oxides: on-site Coulomb repulsion versus covalency. *Journal of Physics: Condensed Matter* **11(7)**, 1657–1683.
- [93] Pickett, W. E., and Singh, D. J. (1997). Chemical disorder and charge transport in ferromagnetic manganites. *Physical Review B* **55(14)**, 8642–8645.
- [94] Novák, P., Boucher, F., Gressier, P., Blaha, P., and Schwarz, K. (2001). Electronic structure of the mixed valence system $(\text{YM})_2\text{BaNiO}_5$ ($M=\text{Ca, Sr}$). *Physical Review B* **63(23)**, 235114–235122.

Curriculum vitae

name **Michaela Küpferling**
 nationality Austria
 date of Birth April 10 1973
 gender female

EDUCATION

Nov 2001-present Vienna University of Technology,
 Dept. of Solid State Physics, PhD,
 doctoral thesis "Rare Earth substituted Hexaferrites"
 1991-2001 Vienna University of Technology,
 Technical Physics and Technical Mathematics
 Dept. of Experimental Physics, diploma thesis
 "Eddy currents in pulsed magnetic fields"
 second diploma exam in Technical Physics passed
 with distinction October 17 2001
 degree "Diplom-Ingenieurin"
 (Master of Science) obtained November 5 2001
 1983-1991 Gymnasium, GRG X, Laaerbergstr.1, A-1100 Vienna
 main subject: foreign languages
 minor subjects: EDV, act
 graduation (Matura) May 1991

WORK EXPERIENCE

Jan 2002-present Vienna University of Technology,
 Dept. of Solid State Physics,
 A-1040 Vienna, scientific employee
 Nov 2001-Dec 2001 Vienna University of Technology,
 Dept. of Experimental Physics,
 A-1040 Vienna, scientific employee
 Jan 1994-present EVVA Werk GmbH&CoKG, A-1120 Vienna,
 electronics development

(keysystems and access control)
 Jul 1990, Anker Brot AG, A-1101 Vienna, sales (food)
 Jul 1991,
 Aug 1992 and
 Sep 1993
 Jul 1989 Mewa Textil-Mietservice Habsburg Wien GmbH,
 A-1140 Vienna, factory worker
 (laundry)

TEACHING

2004 Tutor for 3rd semester students in Technical Physics,
 exercises "Grundlagen der Physik III-Übungen"
 (quantumphysics)
 2003 Tutor for 3rd semester students in Technical Physics,
 laboratory exercises "Laborübungen II"
 (electromagnetic waves and harmonic oscillations)
 2002 Tutor for 2nd semester students in Technical Physics,
 laboratory exercises "Laborübungen I"
 (electronics)

RESEARCH ACTIVITIES AND TRAINING ABROAD

Apr 2004 Institute of Physics of ASCR, 162 53 Prague 6,
 Czech Republic, training in electronic structure
 calculation during PhD
 Oct 2003-Jan 2004 Centro de Investigaciones en Materiales Avancados
 (CIMAV), 31109 Chihuahua, Chih., Mexico,
 preparation of new magnetic materials during PhD
 Apr 2003 34th IFF spring school, Forschungszentrum Jülich,
 "Nanoelectronics"
 May 2001 Cargese, Corsica, summer school,
 "High Magnetic Fields"